Centre Énergie Matériaux Télécommunications

DÉVELOPPEMENT ET OPTIMISATION DE LA SPECTROSCOPIE DE PLASMA INDUIT PAR LASER (LIBS) APPLIQUÉE À L'ANALYSE DU PALLADIUM DANS LA ROCHE MINÉRALISÉE : CALIBRATION, CARACTÉRISATION DU PLASMA ET EFFETS ENVIRONNEMENTAUX

Par

Samira Selmani

Thèse présentée pour l'obtention du grade de
Philosophiae Doctor (Ph.D.)
en sciences de l'énergie et des matériaux

Jury d'évaluation

Président du jury	Andreas Ruediger INRS-EMT
Examinateur externe	Aïssa Harhira Conseil national de recherches du Canada
Examinateur externe	Diane Beauchemin Université Queen's
Directeur de recherche	François Vidal INRS-EMT
Codirecteur de recherche	Marc Constantin Université Laval

REMERCIEMENTS

"*Je souhaite avant tout exprimer ma gratitude envers Dieu, qui m'a offert la force, le courage et la détermination nécessaires pour surmonter les épreuves rencontrées tout au long de mes études et lors de la réalisation de ce projet*."

Ce travail de thèse représente bien plus qu'une étape académique: il s'agit d'une aventure scientifique et personnelle marquante pour moi. Géologue de formation, j'ai pu, à travers cette thèse, explorer de nouveaux horizons et me familiariser avec la technique d'analyse géochimique LIBS (Laser-Induced Breakdown Spectroscopy). Cette méthode innovante et fascinante m'a permis d'aborder des problématiques complexes tout en enrichissant mes compétences techniques et analytiques.

Je tiens également à remercier les membres du jury (Pr Andreas Ruediger, Dr Aïssa Harhira et Pr Diane Beauchemin) qui ont accepté de consacrer leur temps à l'évaluation de ce travail.

Je tiens à exprimer toute ma gratitude à François Vidal, mon directeur de recherche principal, pour son soutien indéfectible, ses conseils avisés et son engagement sans faille tout au long de ce projet. Son expertise, sa passion pour la recherche et sa rigueur scientifique m'ont constamment inspiré. François a su me guider avec une patience et une bienveillance remarquable, tout en m'encourageant à repousser mes limites et à explorer de nouvelles perspectives. Ses conseils éclairés et sa disponibilité ont grandement contribué à la réussite de ce travail. Je suis particulièrement reconnaissante de sa présence et de son engagement inconditionnel. François a toujours été disponible pour des discussions approfondies, des réunions régulières et des corrections rapides des articles, faisant preuve d'un suivi rigoureux et d'une implication constante dans mon encadrement. Son sens de l'organisation et sa réactivité ont été des atouts précieux pour avancer efficacement dans ce projet. Ses mots d'encouragement et sa confiance en mes capacités, surtout dans les moments les plus difficiles, ont été une source de motivation inestimable. Je lui suis infiniment reconnaissante pour son accompagnement, sa bienveillance et son engagement tout au long de ce parcours.

Merci, François, pour votre enthousiasme, votre confiance et pour avoir fait de cette expérience un véritable enrichissement, tant sur le plan professionnel que personnel.

Je tiens à remercier mon Cosuperviseur, le professeur Marc Constantin, qui m'a transmis de précieuses connaissances géologiques, m'a fourni une aide inestimable pour l'interprétation des

données géologiques et m'a accompagnée avec patience pour comprendre les enjeux scientifiques liés à ce projet.

Je tiens également à exprimer ma profonde reconnaissance au Dr. Mohamad Sabsabi qui m'a formé à la technique LIBS, ce qui m'a permis de maîtriser les outils nécessaires à l'analyse et à l'interprétation de mes résultats. Son expertise et sa pédagogie ont été essentielles pour approfondir ma compréhension des aspects techniques de ce travail.

Je tiens à remercier tout particulièrement le Dr. Paul Bouchard pour son soutien exceptionnel tout au long de ce projet. Il a généreusement partagé ses vastes connaissances théoriques et expérimentales en spectroscopie d'émission optique, ce qui a grandement enrichi mon travail. Son aide précieuse pour optimiser le montage expérimental, ainsi que sa disponibilité constante au laboratoire du CNRC, ont été des atouts indispensables à la réussite de cette recherche. Paul a toujours fait preuve d'une gentillesse et d'un accueil remarquables, créant une atmosphère chaleureuse et bienveillante au sein du laboratoire. Pour moi, je le considère comme un père de substitution, toujours prêt à m'aider, à me conseiller et à m'encourager. Je lui suis profondément reconnaissante pour son accompagnement, sa générosité et son humanité, qui ont rendu cette expérience inoubliable.

Je tiens à souligner que tout ce travail n'aurait pas été possible sans le soutien et la collaboration de plusieurs équipes et personnes. Un grand merci à l'équipe de technologies optiques (Aïssa Harhira, Paul Bouchard, Josette El Haddad, Francis Boismenu, Guy Lamouche et Francis Vanier) du Centre de recherche sur les innovations dans les énergies propres du Conseil National de Recherches Canada (CNRC Boucherville) pour son expertise technique, son appui logistique et son esprit collaboratif. Votre contribution a été essentielle à la réalisation de ce projet.

Je remercie également l'INRS à Varennes pour son accueil et les ressources mises à disposition, ainsi que toute l'équipe administrative pour son professionnalisme et son efficacité.

Et, je tiens à exprimer ma gratitude à Madame Michelle Marcotte pour son soutien administratif, sa disponibilité et son aide précieuse tout au long de ce parcours.

Je tiens à exprimer ma profonde gratitude à Lionnel Djon d'Impala Canada pour avoir fourni les carottes de forage du quartier de la mine du Lac des Îles, ainsi que pour les analyses en laboratoire et le soutien financier accordé par Impala Canada. Sa contribution a été essentielle à la réalisation de ce projet.

Je tiens à te remercier du fond du cœur, Nessrine, pour ton aide précieuse dans la préparation des matériaux de référence à l'Université Laval. Grâce à toi, j'ai pu optimiser le montage et aborder les mesures nécessaires avec une confiance accrue.

Au-delà de ton professionnalisme, tu as été une amie proche, toujours présente pour m'encourager et me soutenir dans les moments importants. Tu es bien plus qu'une collègue pour moi : tu es comme une sœur, et je suis infiniment reconnaissante.

Je tiens à adresser un sincère merci à mon collègue Ismail Elhamdoui pour son soutien précieux tout au long de cette thèse. Ses encouragements constants, son aide dans le laboratoire et sa bonne humeur ont été d'un grand réconfort, surtout dans les moments les plus exigeants. Merci pour ta collaboration, ton esprit d'équipe et ton amitié, qui ont rendu ce parcours encore plus enrichissant.

Je tiens à exprimer ma profonde gratitude à toutes les personnes qui ont contribué, de près ou de loin, à la réalisation de cette thèse. Une mention spéciale va à mes chers collègues et amis de l'INRS : Amine, Anoir, Marwa, Sabrina, Amira, Yahia, Assaad, Oumaima et Ellisa.

Amine, tu as été bien plus qu'un collègue pour moi. Tout au long de ce parcours, tu as été présent à mes côtés comme un frère, toujours prêt à me guider, à m'aider et à me conseiller avec une générosité sans faille. Nos discussions enrichissantes autour d'un repas à la cafétéria, tes conseils pertinents et ton soutien constant ont été une source d'inspiration et de motivation pour moi. Sans ton accompagnement, cette aventure n'aurait pas été la même.

Merci du fond du cœur pour ton amitié, ta patience et ton dévouement. Tu as marqué cette étape de ma vie d'une manière inoubliable, et je suis infiniment reconnaissante pour tout ce que tu as fait pour moi.

Même si je suis loin d'eux aujourd'hui, je tiens à remercier mes parents (Mohamad et Saliha), ainsi que mes deux sœurs (Marwa et Nawel), pour leur soutien inestimable.

RÉSUMÉ

Les analyses traditionnelles d'échantillons miniers fournissent des informations essentielles sur la composition et la qualité des gisements. Elles sont effectuées à l'aide de méthodes telles que la chimie humide ou la pyroanalyse, et sont associées à des délais d'attente d'au moins 24 heures. Ces délais entraînent des retards de production sur les sites miniers, ce qui se traduit par une augmentation des coûts d'exploitation et de production. Pour relever ces défis, l'industrie minière explore de nouvelles technologies visant à réduire les coûts. Parmi ces innovations, on trouve la mesure en temps réel et sur site de la concentration d'Éléments du Groupe du Platine (ÉGP) pendant les différentes phases de l'exploration. La spectroscopie laser plasma LIBS (pour l'acronyme « Laser-Induced breakdown spectroscopy ») apparaît comme une technique potentielle pour effectuer des analyses multi-élémentaires dans les conditions souhaitées en temps réel et sur site.

Cette thèse de doctorat porte sur divers aspects de l'utilisation de la technique LIBS pour déterminer la concentration de palladium (Pd) dans les carottes de forage provenant de la mine de palladium de Lac des Iles (LDI) située à 127 km au nord de Thunder Bay, en Ontario, au Canada. Nous avons utilisé trois ensembles de matériaux de référence certifiés sous forme de poudres comprimées avec une concentration quasi homogène de palladium allant d'environ une partie par million (ppm) à 500 ppm pour calibrer l'instrument LIBS. La concentration moyenne en Pd a été déterminée par LIBS et comparée à celle obtenue à partir des résultats d'analyse du laboratoire de la mine pour la moitié de la carotte originale.

Nous nous sommes aussi intéressés à la caractérisation des plasmas et la morphologie des cratères d'ablation laser dans l'air ambiant à la pression atmosphérique sur les différentes phases minérales qui composent le minerai. En particulier, la température et la densité électronique du plasma ont été déterminées pour chaque phase (le plagioclase, le feldspath et l'amphibole) à partir des raies de fer et de nickel des spectres LIBS.

Nous avons utilisé la technique LIBS pour étudier l'effet de l'humidité de la roche sur les mesures et l'impact de l'eau sur le plasma. Pour aborder ce problème, et suivre l'évolution du signal en fonction du temps, nous avons réalisé des mesures LIBS à l'aide de 1080 tirs laser sur un fragment de minerai de palladium mouillé, jusqu'à ce que la roche sèche complètement.

Enfin, nous avons étudié le nombre de mesures (spectres ou tirs laser) minimum nécessaires pour évaluer la concentration moyenne de palladium dans les carottes de LDI pour une précision donnée.

Mots-clés : spectroscopie laser plasma (LIBS), analyse des carottes solides, concentration de palladium, étalonnage LIBS, ablation laser, phases minérales, morphologie des cratères d'ablation laser, humidité, temps de mesure, distribution du palladium.

ABSTRACT

Traditional mining sample analysis provides essential information on the composition and quality of mineral deposits. These analyses are carried out using methods such as wet chemistry or pyroanalysis and involve waiting times of at least 24 hours. Such delays lead to production bottlenecks at mining sites, resulting in increased operating and production costs. To address these challenges, the mining industry is exploring new technologies to reduce costs. One such innovation is the real-time, on-site measurement of platinum group element (PGE) concentrations at various stages of exploration. Laser Induced Breakdown Spectroscopy (LIBS) is emerging as a promising technique for performing multi-element analyses under desired conditions in real time and on-site.

This doctoral thesis focuses on various aspects of using LIBS technology to determine the concentration of palladium (Pd) in drill cores from the Lac des Iles (LDI) palladium mine, located 127 km north of Thunder Bay, Ontario, Canada. We used three sets of reference materials in the form of compressed powders with nearly homogeneous palladium concentrations ranging from approximately one part per million (ppm) to 500 ppm to calibrate the LIBS instrument. The average Pd concentration was determined using LIBS and compared to the results obtained from laboratory analyses of the mine for half of the original mine core.

We also investigated the plasma characterisation and morphology of laser ablation craters in ambient air at atmospheric pressure over different mineral phases composing the ore. Specifically, the temperature and electron density of the plasma were determined for each phase (plagioclase, feldspar and amphibole) using iron and nickel spectral lines from LIBS spectra.

The LIBS technique was used to investigate the effect of rock moisture on the measurements and the effect of water on the plasma. To address this issue and to monitor the signal evolution over time, we performed LIBS measurements with 1,080 laser shots on a wet palladium ore fragment until the rock was completely dry.

Finally, we investigated the minimum number of measurements (spectra or laser shots) required to estimate the average palladium concentration in LDI drill cores with a given precision.

Keywords: Laser-Induced Breakdown Spectroscopy (LIBS), solid core analysis, palladium concentration, LIBS calibration, laser ablation, mineral phases, laser ablation crater morphology, moisture, measurement time, palladium distribution.

TABLE DES MATIÈRES

LISTE DES FIGURES

LISTE DES TABLEAUX

LISTE DES ABRÉVIATIONS

AMC : Association Minière du Canada

AEMQ : Association de l'Exploitation Minière du Québec

ASE : Agence Spatiale Européenne

ACP : Analyse en Composantes Principales

CCIM : Conseil Canadien de l'Innovation Minière

ÉGP: Éléments du Groupe du Platine

Fe: Fer

ICP-MS : Spectrométrie de Masse à Plasma à Couplage Inductif

Ir: Iridium

IUPAC: International Union of Pure and Applied Chemistry

LDI : Lac Des Iles

LIBS : Laser-Induced Breakdown Spectroscopy/ Spectroscopie des Plasmas Induits par Laser

LoD: Limite de Detection

MEB : Microscope Electronique à Balayage

MR : Matériaux de Rréférence certifiés : LDI-1, CDN-ME-1208 et PTC-1b

NASA : Agence Spatiale Américaine

Ni: Nickel

Os: Osmium

Pd: Palladium

ppm : partie par million

Pt: Platine

Rh: Rhodium

Ru: Ruthénium

S/N : Rapport Signal/Bruit (Noise)

USGS : US Geological Survey

XRF : Spectrométrie de fluorescence X

CHAPITRE I

1 INTRODUCTION

1.1 Contexte général

Les matériaux géologiques sont le plus souvent difficiles à étudier visuellement en raison de la diversité et de la complexité des processus géologiques qui ont conduit à leur formation. Cependant, les analyses d'échantillons miniers réalisées à l'aide de techniques conventionnelles (Inductively Coupled Plasma – Mass Spectrometry (ICP-MS), Inductively Coupled Plasma – Atomic Emission Spectroscopy (ICP-AES), Atomic Absorption Spectroscopy (AAS), etc.) basées sur la chimie humide, la pyroanalyse, l'ICP [1] ou l'absorption atomique [2], impliquent des temps d'attente d'au moins 24 heures. Cela entraîne des retards sur les sites miniers et augmente ainsi les coûts d'exploitation et de production [3]. En effet, la caractérisation des matériaux géologiques à l'aide de ces techniques implique des méthodes de préparation longues et exigeantes qui nécessitent le concassage des échantillons sous forme de poudres, puis leur dissolution dans des acides, ce qui entraîne une perte d'informations spatiales liées à l'identification minéralogique, et à la composition élémentaire et à la distribution des matériaux dans les échantillons. En outre, ces techniques de laboratoire ne sont pas adaptées aux conditions de terrain en raison de leur nature hors ligne qui nécessite une infrastructure spéciale, de la main-d'œuvre hautement qualifiée, l'élimination des consommables et des déchets chimiques.

Alors que la demande de minéraux et de métaux ne cesse de croître, l'attention se porte de plus en plus sur ce que l'on appelle les « minéraux critiques ». Ces minéraux critiques englobent plusieurs minéraux et métaux essentiels aux nouvelles technologies, notamment le cobalt, le cuivre, les métaux précieux, le nickel, l'uranium, le lithium, le magnésium, et bien d'autres encore. Ces dernières années, la demande en métaux précieux a augmenté de manière exponentielle, en grande partie en raison de leur importance dans divers secteurs clés de l'économie mondiale. Les métaux précieux, tels que l'or, et les éléments du groupe du platine (ÉGP), ne sont plus uniquement considérés comme des valeurs refuges pour les investisseurs en temps de crise économique, ils jouent désormais un rôle important dans le développement technologique et industriel. L'importance économique de l'extraction des métaux précieux ainsi que l'épuisement de la ressource poussent l'industrie minière canadienne des métaux précieux à être toujours à la recherche de nouvelles technologies qui favorisent les activités minières [4]. L'une de ces technologies novatrices, qui constituerait une avancée majeure selon le Conseil canadien de l'innovation minière (CCIM) et l'Association minière du Canada (AMC) [5], est la mesure en temps

réel de la teneur en métaux précieux lors des différentes étapes de l'exploration et de la production minière, y compris le traitement du minerai.

La spectroscopie de plasma induite par laser, aussi appelée spectroscopie laser plasma (LIBS pour « Laser-Induced Breakdown Spectroscopy ») est une technologie prometteuse pour réaliser des analyses élémentaires dans les conditions souhaitées, en temps réel et sur site. Le principe de cette méthode d'analyse consiste à focaliser un faisceau laser intense sur la surface d'un échantillon de matériau (solide, liquide ou gazeux) pour atomiser une fraction de la surface et générer un plasma. La lumière émise par le plasma est ensuite recueillie et analysée spectralement pour déterminer la composition chimique de l'échantillon. En utilisant des étalons, elle permet de déterminer la concentration des éléments contenus dans n'importe quel échantillon de la même famille de composition [6]. Les principaux avantages potentiels de la LIBS pour l'industrie minière par rapport aux techniques analytiques conventionnelles sont sa capacité à analyser rapidement les échantillons sur site avec une préparation minimale ou nulle, quelle que soit la nature de l'échantillon [6].

1.2 Les éléments du groupe du platine (ÉGP)

Les géologues du secteur minier s'intéressent à la détermination des concentrations des ÉGP : le platine (Pt), le palladium (Pd), le rhodium (Rh), le ruthénium (Ru), l'osmium (Os) et l'iridium (Ir), collectivement appelés métaux nobles dans les minéraux sulfurés naturels. Les ÉGP se présentent généralement sous la forme de sulfures magmatiques qui se forment lors du refroidissement du magma remontant des profondeurs de la terre vers la surface. Ces métaux se distinguent par leurs propriétés chimiques et physiques uniques, telles qu'une résistance exceptionnelle à la corrosion, une grande stabilité chimique et un point de fusion élevé. En raison de ces caractéristiques, les ÉGP sont largement utilisés dans diverses applications industrielles, notamment dans les catalyseurs automobiles, les dispositifs électroniques, ainsi que dans de nombreuses technologies émergentes. Leur rareté dans la croûte terrestre, combinée à leur importance stratégique, confère à ces métaux une valeur économique considérable. Dans ce contexte, le Canada occupe une place significative sur la scène mondiale en tant que troisième plus grand producteur d'ÉGP [7], après l'Afrique du Sud et la Russie (AEMQ: Association de l'exploitation minière du Québec et US Geological Survey (USGS)). La valeur monétaire annuelle des ÉGP produits au Canada est proche d'un milliard de dollars [7]. Les ÉGP sont largement exploités au Canada comme produits secondaires du minerai de cuivre et de nickel, ainsi que dans la mine de Lac des Iles (LDI), située près de Thunder Bay dans l'Ouest de l'Ontario. Cette

mine est la seule source primaire d'ÉGP au Canada. Exploitée par notre partenaire dans le projet de recherche qui fait l'objet de cette thèse, Impala Canada, elle joue un rôle important dans l'approvisionnement en ÉGP du pays, et contribue ainsi à l'industrie mondiale de ces métaux précieux.

Cependant, l'exploitation minière traditionnelle des ÉGP implique des analyses chimiques laborieuses à toutes ses étapes, ce qui prolonge les délais de traitement et augmente les coûts, réduisant ainsi la rentabilité des opérations minières. Les principales techniques d'analyse chimique utilisées dans ce domaine sont pyroanalyse, la spectrométrie d'absorption atomique, la fluorescence X et l'ICP-MS. Chacune de ces techniques présente des avantages spécifiques en fonction des éléments à analyser et de la précision requise. Dès les phases d'exploration et de prospection, les analyses chimiques permettent d'identifier les zones minéralisées en détectant la présence de métaux précieux dans les échantillons. Elles servent également à évaluer le potentiel économique d'un gisement en déterminant sa teneur en métaux et sa taille. Lors de la conception des opérations minières, les analyses chimiques sont indispensables pour optimiser l'extraction en fonction de la nature du minerai. Elles permettent de dimensionner correctement les équipements et de choisir les méthodes d'extraction les plus adaptées. Pendant l'exploitation, les analyses chimiques assurent un contrôle qualité continu. Elles permettent de suivre l'évolution de la teneur en métaux précieux au fil du temps et d'ajuster les procédés de traitement en conséquence. De plus, elles sont essentielles pour garantir le respect des normes environnementales en contrôlant la qualité des rejets miniers.

En raison de leur faible concentration dans le minerai, les ÉGP, y compris le palladium, n'échappent pas au problème de la complexité, de la durée et du coût élevé des analyses chimiques. Face à ces défis, les industries minières auraient avantage à se tourner vers des techniques plus rapides et économiques, telles que la LIBS. Cette technique permet de réaliser des analyses quantitatives in situ et en temps réel des ÉGP dans les minerais, permettant de déterminer des concentration moyennes sous la partie par million (ppm), comme cela a été démontré dans l'analyse du palladium dans cette thèse [8]. En adoptant des méthodes telles que la LIBS, les coûts et les délais associés aux méthodes traditionnelles seraient considérablement réduits, offrant ainsi une solution efficace pour l'exploitation des métaux précieux à faible concentration.

Il est important de souligner que la seule technique d'analyse actuellement disponible pour le palladium et les autres métaux précieux est la fluorescence des rayons X portative (pXRF pour « Portable X-Ray Fluorescence »). Cependant, cette technique est mal adaptée à la mesure de la teneur en éléments traces, en raison de sa limite de détection (LoD pour « Limit of Detection »)

élevée. C'est ici que la spectroscopie par ablation laser (LIBS) se distingue comme la solution la plus prometteuse grâce à sa capacité à fournir des concentrations beaucoup plus basses, adaptées aux exigences de l'industrie minière moderne pour les ÉGP.

En adoptant des technologies comme la LIBS, l'industrie minière canadienne des métaux précieux, notamment notre partenaire, Impala Canada, pourrait bénéficier d'un atout significatif. Non seulement cette technologie permettrait d'exploiter des gisements à plus faible teneur en métaux de base, augmentant ainsi les réserves disponibles, mais elle contribuerait également à améliorer l'efficacité énergétique en réduisant le traitement de la gangue (minerai non précieux) et, par conséquent, les émissions de gaz à effet de serre.

1.3 Historique et évolution de la spectroscopie LIBS pour les applications minières

La LIBS a vu le jour dans les années 1960, marquant le début d'une révolution dans l'analyse spectroscopique des matériaux. Avant l'année 1980, la LIBS est plutôt restée confinée dans les laboratoires, où de nombreuses preuves de concept ont été effectuées pour l'analyse d'échantillons sous forme gazeuse [9,10] ou solide [11]. L'année 1984 marque le début des analyses de liquides, ouvrant ainsi de nouvelles perspectives pour cette technologie [12-14]. Au fil des décennies, la LIBS a connu une évolution significative, passant d'une méthode exploratoire à un outil analytique. Au cours des 30 dernières années, des applications concrètes du LIBS ont vu le jour en raison des avantages uniques que présente cette technique par rapport aux autres méthodes d'analyse. Ces avantages résident notamment dans l'absence ou la faible préparation des échantillons, la possibilité de mesures à distance et sans contact, la réponse instantanée et l'analyse d'échantillons de dimensions micrométriques.

Les premières applications de la LIBS ont été réalisées au laboratoire de Los Alamos pour la détection de vapeurs et de gaz dangereux dans l'air [15,16], ainsi que pour la détection de faibles quantités de béryllium dans l'air ou sur des filtres [16,17]. Dans les années 1980 et 1990, des améliorations majeures ont été apportées à la technique, notamment grâce à l'avènement des lasers pulsés à haut taux de répétition et à l'intégration de détecteurs plus sensibles comme les dispositifs à couplage de charge (CCD), ce qui a permis d'augmenter la précision et la sensibilité des mesures. Par la suite, la LIBS a été perfectionnée pour résoudre des problèmes pratiques tels que le suivi de la contamination environnementale [18-21], le contrôle des procédés industriels [22-24], et le tri des matériaux pour en faciliter le recyclage [24-27]. De plus, la capacité de la LIBS d'effectuer une détection à distance et instantanée a stimulé son implantation dans les

domaines du nucléaire [28-30] et de la sécurité, comme pour la détection et l'analyse de bactéries [31-37] et d'explosifs [38-41]. D'autre part, l'agence spatiale américaine (NASA), en collaboration avec l'agence spatiale européenne (ASE), a intégré un système LIBS dans la navette d'exploration planétaire dans le but d'analyser le sol de Mars [42-46].

Actuellement, la LIBS continue de prouver son efficacité et sa pertinence dans l'industrie minière, en raison de sa rapidité et de sa capacité à détecter une large gamme d'éléments [47,48]. Elle a aussi démontré sa pertinence dans diverses applications géochimiques [49-51], géologiques [52], ainsi que dans les géosciences [53-56]. Les avancées technologiques récentes ont permis de développer des systèmes LIBS spécifiques, qui ont été produits et mis en œuvre par l'industrie minière pour l'analyse en ligne, le traitement et le classement rapides du minerai [57-62], ainsi que pour la caractérisation des boues de minerai [63-66]. Des études récentes ont démontré que la LIBS peut être utilisée pour l'analyse quantitative rapide des carottes de forage, offrant ainsi une solution efficace pour évaluer la composition élémentaire directement sur le terrain [67-69]. De nombreux travaux se sont concentrés sur l'application de la LIBS en minéralogie, notamment pour la classification et la discrimination des échantillons, et l'analyse géochimique quantitative in situ [70,71]. Récemment, la forte demande pour les métaux précieux a considérablement augmenté, poussant l'industrie minière à adopter des méthodes d'analyse plus rapides et efficaces. En réponse à cette demande croissante, l'industrie s'est de plus en plus tournée vers l'utilisation de la LIBS pour quantifier et caractériser ces métaux. En raison de sa capacité à fournir des analyses élémentaires rapides, sur le terrain, et sans nécessiter de préparation complexe des échantillons, la LIBS est perçue comme une solution idéale pour répondre aux besoins croissants de l'industrie. De plus, des recherches récentes ont révélé que la LIBS est capable de quantifier les éléments traces dans les minerais, ce qui est important pour l'identification des zones à haute teneur en métaux précieux comme l'or et le palladium. En particulier, le groupe du CNRC de Boucherville [72-73] et notre équipe ont récemment étudié la LIBS pour la quantification de l'or [74], du palladium [75,76] et du platine [77] dans les minerais solides où ils sont présents en faibles quantités, de l'ordre de la ppm. Nous nous sommes aussi intéressés à l'ablation laser et aux propriétés d'émission du plasma des différentes phases minéralogiques dans le minerai de palladium [78].

Il est également important de noter que les avancées récentes en matière d'ingénierie et de miniaturisation ont permis au CNRC de Boucherville de créer un prototype d'instrument LIBS portable, nommé ProspectOre, capable de mesurer in situ la concentration d'or dans le minerai [79,80]. Cette technologie, a été développée avec la participation de compagnies minières et a

été testée sur site. Une technologie similaire pourra être développée pour l'évaluation rapide et in situ des gisements d'ÉGP.

De plus en plus, les entreprises minières reconnaissent la LIBS comme la méthode la plus rapide et la plus rentable pour les analyses in situ, pouvant réduire les coûts et les délais associés aux techniques analytiques conventionnelles. D'autres études ont également démontré l'efficacité de la LIBS pour détecter des éléments présents dans un échantillon à des niveaux d'abondance de l'ordre de la ppm [81] pour réaliser des cartographies multi-élémentaires rapides et à haute résolution d'échantillons géologiques [82], et pour identifier les teneurs en minéraux et en métaux précieux dans des échantillons de minerai [83]. Bien que les LoD élémentaires pour l'analyse LIBS soient variables [81-85], la sensibilité a augmenté et LoD a été amélioré au cours des deux dernières décennies, grâce aux progrès technologiques de l'instrumentation. Ces avancées récentes confirment la place centrale que la LIBS pourrait occuper dans les applications minières actuelles, en particulier pour les ÉGP, où elle attend d'être intégrée aux processus d'exploration et de production.

1.4 Les avantages et les défis de la recherche sur la LIBS

La technique LIBS présente de nombreux avantages par rapport aux autres méthodes spectroscopiques, notamment une mise en œuvre simple et rapide. Elle permet une analyse en temps réel, nécessitant peu ou pas de préparation des échantillons, avec des résultats obtenus en quelques secondes ou minutes. Polyvalente, elle s'adapte à différents types de matériaux (solides, liquides, gazeux) et d'échantillons (métaux, minéraux ou verres, etc.,). De plus, elle offre une analyse multi-élémentaire, détectant simultanément plusieurs éléments dans un échantillon. Compacte, elle permet l'utilisation de systèmes portables pour des analyses in situ, avec une capacité d'analyse à distance sur plusieurs dizaines de mètres. Elle est quasi non destructive, puisqu'elle ne prélève que quelques nanogrammes ou microgrammes de matière.

Néanmoins, la LIBS continue de poser de nombreux défis aux chercheurs qui travaillent à l'adapter à l'analyse des métaux précieux dans le domaine minier. Ces défis incluent principalement : (i) l'amélioration des limites de détection pour répondre aux exigences de précision nécessaires dans l'exploitation de gisements à faible teneur, (ii) l'identification précise des différentes phases minéralogiques dans les roches ou les carottes de forage, (iii) la quantification du palladium dans les carottes de forage, et (iv) le développement de systèmes LIBS robustes et portables capables de fonctionner efficacement dans des environnements miniers difficiles. Nous avons abordé ces défis dans cette thèse en nous concentrant sur

l'optimisation de la technologie LIBS pour améliorer la reproductibilité des résultats sur le terrain et proposer une solution pratique et précise à l'industrie minière.

1.5 Objectifs de la thèse

L'objectif général de cette thèse est de jeter les bases du développement d'un instrument portable basé sur la LIBS, permettant une analyse quantitative en temps réel et in situ des minerais d'ÉGP. Cet instrument innovant vise à offrir une solution rapide, précise et efficace pour identifier et quantifier les éléments précieux présents dans les échantillons miniers directement sur le site d'extraction. En intégrant les dernières avancées technologiques en matière de laser et de détection spectrale, ce projet ambitionne de répondre aux besoins de l'industrie minière pour des analyses immédiates, réduisant ainsi les délais et les coûts associés aux méthodes traditionnelles. Ce développement constitue une étape vers l'amélioration des techniques d'exploration minérale et la gestion plus durable et rentable des ressources naturelles.

Ce travail de thèse s'est concentré spécifiquement sur le palladium car cet ÉGP est la préoccupation principale de notre partenaire, Impala Canda, qui opère la mine de Lac des Iles. De plus, la mesure des autres ÉGP pose des défis particuliers en raison de leur plus faible concentration dans le minerai et des interférences spectrales avec des éléments très émissifs, présents dans le minerai, comme le fer et le nickel.

Les sous-objectifs de ce projet de thèse ainsi que les résumés de leur réalisation sont décrits ci-dessous.

Objectif 1 : *Établir des courbes d'étalonnage (i.e. l'intensité nette normalisée d'une raie de palladium en fonction de sa concentration) permettant de mesurer la concentration de palladium directement dans le minerai solide de Lac des Iles.*

Les courbes d'étalonnage ont été établies à l'aide de matériaux de référence (MR) certifiés, LDI-1, CDN-ME-1208 et PTC-1b, sous forme de pastilles de poudre homogène et compactée. Trois MR ont été utilisés au lieu d'un seul afin de fournir une plus grande variété de matrices et améliorer la détermination des concentrations dans le minerai rocheux. Ces pastilles ont été dopées au moyen de solutions aqueuses de chlorure de palladium pour obtenir des concentrations de 25, 50, 100, 200 et 500 ppm de palladium. Ces concentrations ont été vérifiées par des méthodes analytiques conventionnelles. Puis, nous avons préparé des courbes d'étalonnage selon une technique originale que nous avons développée pour les minerais d'or [73,75]. Des concentrations aussi élevées que 500 ppm sont nécessaires car la concentration

locale, à l'échelle de la tache focale laser, sur des échantillons de roche peut être beaucoup plus élevée que leur concentration moyenne, généralement de l'ordre de la ppm. Ces courbes d'étalonnage ont été utilisées pour déterminer la concentration de palladium dans les échantillons de carottes de forage provenant de la mine de Lac des Iles dont l'analyse chimique de la moitié longue de la carotte originale a été effectuée au moyen de techniques de laboratoire standards.

Objectif 2 : *Évaluer quantitativement la concentration moyenne de palladium dans les carottes de forage de la mine de Lac des Iles au moyen de la distribution spatiale du palladium dans le minerai obtenu par un balayage laser.*

La technique LIBS est basée sur l'utilisation d'une courbe d'étalonnage (objectif 1) établie à l'aide d'un ensemble d'échantillons homogènes, les MR, pour lesquels la concentration de l'ÉGP d'intérêt est connue. Dans ce contexte, nous avons exploré principalement trois aspects de l'analyse LIBS d'une carotte de forage de LDI : (1) la distribution spatiale du palladium dans le minerai, (2) l'évaluation quantitative de la concentration moyenne de palladium, et (3) l'analyse qualitative des phases du minerai à l'aide de l'analyse en composantes principales (ACP) effectuée à l'aide des spectres LIBS. Pour l'évaluation quantitative de la concentration moyenne de palladium, nous avons utilisé trois courbes d'étalonnage basées sur les trois MR et nous avons utilisé la corrélation de Pearson entre les spectres de référence et les spectres des échantillons de roche pour déterminer le MR le plus pertinent pour chaque tir lasera été utilisé pour identifier la courbe de calibration.

Objectif 3 : *Caractériser la morphologie des cratères d'ablation laser créés à la surface des échantillons de minerai de LDI pour les trois principales phases minéralogiques (plagioclase, amphibole et sulfures) pour plusieurs séries de nombres de tirs laser et déterminer les propriétés d'émission du plasma créé dans ces phases en fonction du nombre de tirs.*

Cet objectif consiste à donner un aperçu de l'interaction laser-minéral dans le contexte de l'analyse géochimique LIBS d'échantillons de minerais, en mettant l'accent sur la caractérisation du plasma, soit sa température et densité électronique, et la morphologie des cratères d'ablation laser pour 50, 250, 500 et 1 000 tirs laser sur le même site. Nous avons spécifiquement sélectionné une roche de type gabbronorite, représentative du minerai de palladium de la mine LDI, dont nous avons au préalable identifié la minéralogie et les différentes phases à l'aide d'un microscope électronique à balayage MEB et d'un instrument micro-XRF.

Objectif 4 : *Déterminer l'effet de l'humidité de la roche sur l'émission du plasma, et élaborer une stratégie de balayage laser pour optimiser la mesure de la concentration moyenne en EGP.*

Ces deux objectifs complémentaires visent à résoudre des problèmes pratiques que la LIBS rencontrera lors de son implantation sur le site minier. Le premier consiste à étudier l'effet de l'humidité de la roche sur les mesures LIBS et à comprendre comment la présence d'eau affecte le plasma induit par laser. Cette étude s'est imposée suite au constat que les échantillons miniers à analyser sur site présentent généralement un fort taux d'humidité. Pour mener cette étude, nous avons plongé un échantillon de minerai dans l'eau, puis suivi son processus de séchage à l'air libre à l'aide d'une succession de 1 080 tirs laser dans une matrice rectangulaire de 18 x 60, à raison de deux tirs par seconde (2 Hz), soit pendant neuf minutes, jusqu'à ce que la roche soit presque complètement séchée. Le second objectif est de minimiser le nombre de tirs laser nécessaires pour mesurer la concentration moyenne en palladium pour une précision donnée, jugée acceptable. Pour ce faire, nous avons utilisé les résultats d'un balayage laser détaillé de la surface de la carotte, puis un modèle mathématique de la densité de probabilité de la distribution du palladium pour explorer l'espace des paramètres, en particulier l'effet du bruit sur les mesures.

1.6 Organisation de la thèse

Cette thèse, structurée en articles, est organisée en huit chapitres avec une annexe (chapitre 9) :

- Le chapitre 1 offre un aperçu général de la technique LIBS et de ses performances. Il explore également l'analyse des ÉGP, notamment le palladium. L'accent est mis sur l'importance de cette technique pour l'industrie minière, car elle permet une analyse in situ et en temps réel. Enfin, les objectifs principaux de cette thèse y sont présentés.
- Le chapitre 2 décrit les concepts importants de la LIBS tels que les courbes de calibration, la limite de détection et les effets de matrice, ainsi que les mécanismes physiques qui sont à la base de cette technique analytique, notamment l'ablation laser, la génération des raies d'émission, du fond spectral et l'auto-absorption des raies.
- Le chapitre 3 est consacré à la présentation des équipements utilisés pour réaliser ce travail de thèse, c'est-à-dire les lasers, les spectromètres et les détecteurs. Nous décrirons leurs caractéristiques intrinsèques ainsi que la méthodologie utilisée au cours de nos travaux expérimentaux.

Les trois chapitres suivants présentent les trois principaux articles qui font l'objet de cette thèse. Deux d'entre eux sont déjà publiés dans les revues Spectrochimica Acta Part B et Applied Physics A, et le troisième est en cours de révision dans Atomic Spectroscopy au moment du dépôt de cette thèse. L'annexe continent un article supplémentaires dont je ne

suis pas l'auteure principale, mais auxquels j'ai apporté une contribution significative. Cet article est accepté pour la revue PLOS ONE.

- Dans le chapitre 4 je présenterai les résultats que nous avons obtenus pour évaluer quantitativement la concentration moyenne de palladium dans les carottes de forage du site du Lac des Iles.
- Dans le chapitre 5 nous présentons nos résultats concernant la caractérisation de la morphologie des cratères d'ablation laser créés à la surface d'un échantillon de minerai LDI pour les trois principales phases minéralogiques, ainsi que l'émission et les propriétés des plasmas créés dans ces trois phases.
- Le chapitre 6 consiste en une étude spectroscopique dont le but est d'évaluer l'effet de l'humidité de la roche sur le refroidissement du plasma ainsi que sur les mesures effectuées par la spectroscopie de claquage induite par laser (LIBS).
- Enfin le chapitre 7 contient la conclusion générale

La liste complète des articles révisés par des pairs et des présentations à des conférences auxquels j'ai contribué est présentée ci-dessous :

Articles publiés:

1- S. Selmani, N. Mohamed, I. Elhamdaoui, J. Fernandes, P. Bouchard, M. Constantin, M. Sabsabi, F. Vidal, "Laser-induced breakdown spectroscopy analysis of palladium in rock ore", Spectrochimica Acta B 196, 106523 (2022). https://doi.org/10.1016/j.sab.2022.106523

2- S. Selmani, I. Elhamdaoui, N. Mohamed, P. Bouchard, M. Constantin, M. Sabsabi, F. Vidal, "Laser-produced craters in minerals of a palladium ore sample", Applied Physics A: Materials Science and Processing 129, 737 (2023). https://doi.org/10.1007/s00339-023-06966-7

3- S. Selmani, I. Elhamdaoui, P. Bouchard, M. Constantin, M. Sabsabi, F. Vidal, "Effect of rock moisture on laser induced breakdown spectroscopy (LIBS) spectra and plasma properties", accepté pour publication dans Atomic Spectroscopy (2025).

4- F. Vidal, **S. Selmani**, I. Elhamdaoui, N. Mohamed, P. Bouchard, M. Constantin, M. Sabsabi, "Assessment of palladium concentration in drill cores using laser-induced breakdown spectroscopy (LIBS)", accepté pour publication dans PLOS ONE (2025).

5- I. Elhamdaoui, **S. Selmani**, N. Mohamed, P. Bouchard, M. Sabsabi, M. Constantin, F. Vidal, "Quantifying platinum and palladium in solid ore using laser-induced breakdown spectroscopy asssisted by the laser-induced fluorescence (LIBS-LIF) technique", Appl. Spectrosc. 77, 1382 (2023). https://doi.org/10.1177/00037028231202804

6- I. Elhamdaoui, **S. Selmani**, P. Bouchard, M. Sabsabi, M. Constantin, F. Vidal, "Double pulse RLIBS: A new approach for sensitive and quasi-non-destructive sample analysis", prêt à être soumis à Analytical Chemistry (2025) dès que le brevet correspondant sera déposé par le CNRC.

7- I. Elhamdaoui, N. Mohamed, **S. Selmani**, P. Bouchard, M. Sabsabi, M. Constantin, F. Vidal, "Rapid quantitative analysis of palladium in ores using Laser-Induced Breakdown Spectroscopy assisted with laser-induced fluorescence (LIBS-LIF)" J. Anal. At. Spectrom 37, 2537 (2022). https://doi.org/10.1039/d2ja00120a

8- I. Elhamdaoui, K. Rifai, J. Iqbal, N. Mohamed, **S. Selmani**, J. Fernandes, P. Bouchard, M. Constantin, M. Lafamme, M. Sabsabi, F. Vidal, Measuring the concentration of gold in ore samples by laser-induced breakdown spectroscopy (LIBS) and comparison with the gravimetry/ atomic absorption techniques. Spectrochim. Acta Part B, 183106256 (2021).

9- N. Mohamed, K. Rifai, **S. Selmani**, M. Constantin, F. R. Doucet, Ç. Lütfü Ozcan, M. Sabsabi, F. Vidal, “Chemical and mineralogical mapping of platinum-group element ore samples using laser-induced breakdown spectroscopy and micro-X-ray fluorescence”, Geostandards and Geoanalytical Research 45, 539 (2021). https://doi.org/10.1111/ggr.12385

Présentations à des conférences :

1- **S. Selmani**, P. Bouchard, I. Elhamdaoui, N. Mohamed, M. constantin, M. Sabsabi, F. Vidal, “Quantitative analysis of palladium in cores samples using laser-induced breakdown spectroscopy”, GAC-MAC (conférence virtuelle), 1-5 novembrer 2021(orale).

2- **13- S. Selmani**, I. Elhamdaoui, P. Bouchard, M. Constantin, M. Sabsabi, F. Vidal, “Performance of New LIBS Technology for Palladium Analysis in Rock Ore and Characterization of Laser-Induced Crater Morphology”, Québec Mines, Québec, 18-21 novembre 2024(affiche).

3- **14- S. Selmani**, I. Elhamdaoui, P. Bouchard, M. Constantin, M. Sabsabi, F. Vidal, “Laser-induced breakdown spectroscopy analysis of palladium in rock ore, Colloque scientifique INRS-EMT, Montréal, 15-16 février 2024(orale).

4- **15- S. Selmani**, “The performance of laser induced breakdown spectroscopy (LIBS) for the analysis of palladium in rock ore and the characterization of the morphology of laser-generated craters”, The Euro-Mediterranean Symposium on Laser-induced Breakdown Spectroscopy, EMSLIBS 2023, Porto, Portugal, 4-7 septembre 2023(orale).

5- **S. Selmani**, P. Bouchard, I. Elhamdaoui, N. Mohamed, M. Constantin, M. Sabsabi, F. Vidal, “Quantitative analysis of palladium in Lac des Iles core samples using laser-induced breakdown spectroscopy” EMSLIBS (conference virtuelle), 29 novembre -2 décembre 2021.

6- **S. Selmani**, N. Mohamed, I. Elhamdaoui, J. Fernandes, P. Bouchard, M. Constantin, M. Sabsabi, F. Vidal, "Laser-induced breakdown spectroscopy analysis of palladium in rock ore”, LIBS 2022, Bari, Italie, 5-9 septembre 2022 (affiche).

7- **S. Selmani**, I. Elhamdaoui, N. Mohamed, P. Bouchard, M. Constantin, M. Sabsabi, F. Vidal, « Performance de la spectroscopie de rupture induite par laser (LIBS) pour l’analyse du palladium dans le minerai rocheux et la caractérisation de la morphologie des cratères produits par laser », Spectratom 2023, Ottawa, 26-28 juillet 2023(orale).

8- **S. Selmani**, I. Elhamdaoui, N. Mohamed, P. Bouchard, M. Constantin, M. Sabsabi, F. Vidal “Performance of laser-induced breakdown spectroscopy (LIBS) for the analysis of palladium in rock ore and characterisation of the morphology of laser-generated craters”, ICASS 2023, Ottawa, 26-28 juillet, 2023 (orale).

9- **S. Selmani**, I. Elhamdaoui, P. Bouchard, M. Constantin, M. Sabsabi, F. Vidal, “Analysis of palladium in rock ore by Laser-Induced Breakdown Spectroscopy (LIBS) and characterization of the morphology of laser-produced craters”, ICASS 2024, Niagara Falls, Ontario, 26-28 juin, 2024(affiche).

10- I. Elhamdaoui, N. Mohamed, **S. Selmani**, M. Sabsabi, F. Vidal, M. Constantin, P. Bouchard, “Toward in situ and rapid quantitative analysis of platinum-group elements (Pd, Pt and Rh) in ores using Laser-Induced Breakdown Spectroscopy combined with Laser-Induced Fluorescence (LIBS-LIF)”, GAC-MAC (conference virtuelle), 1-5 novembre 2021 (orale).

11- I. Elhamdaoui, **S. Selmani**, F. Vidal, M. Sabsabi, M. Constantin, P. Bouchard, “Rapid quantitative analysis of PGE (Pd, Pt, and Rh) in rock ore using Laser-Induced Breakdown Spectroscopy assisted with laser-induced fluorescence (LIBS-LIF)”, LIBS 2022, Bari, Italie, 5-9 septembre 2022(orale).

12- Elhamdaoui, **S. Selmani**, M. Sabsabi, M. Constantin, P. Bouchard, F. Vidal, « Potentiel de la spectroscopie de claquage assistée par fluorescence induite par laser (LIBS-LIF) pour la détermination des concentrations de métaux précieux dans les minerais solides », Spectratom 2023, Ottawa, 26-28 juillet 2023(orale).

13- I. Elhamdaoui, A. Adame, **S. Selmani**, M. Sabsabi, F. Vidal, M. Constantin, P. Bouchard, « Validation of laser-induced breakdown spectroscopy assisted by laser-induced fluorescence (LIBS-LIF) for the measurement of platinum and palladium in solid ore, SciX, Sparks, Nevada, 8-13 octobre 2023(orale).

14-I Elhamdaoui, **S. Selmani**, M. Sabsabi, M. Constantin, P. Bouchard, F. Vidal, “The potential of laser-induced breakdown spectroscopy assisted by laser-induced fluorescence (LIBS-LIF) for determining precious metal concentrations in solid ores”, ICASS 2023, Ottawa, 26-28 juillet 2023(orale).

15- I. Elhamdaoui, **S. Selmani**, M. sabsabi, F. Vidal, M. Constantin, P. Bouchard, « Application de la Spectroscopie de Plasma Induit par Laser assistée par Fluorescence Induite par Laser (LIBS-LIF) pour la mesure du platine et du palladium dans le minerai solide », Québec Mines, Québec, 18-21 novembre 2024(orale).

2 BIBLIOGRAPHIE

[1] E. Herincs, M. Puschenreiter, W. Wenzel, A. Limbeck, A novel flow-injection method for simultaneous measurement of platinum (Pt), palladium (Pd) and rhodium (Rh) in aqueous soil extracts of contaminated soil by ICP-OES, J. Anal. At. Spectrom, vol. 28, pp. 354–363, 2013.

[2] J.L. Molloy, J.A. Holcombe, Detection of palladium by cold atom solution atomic absorption, Anal. Chem, vol. 78, pp. 6634–6639, 2006.

[3] R.H. Sillitoe, The Challenge of Finding New Mineral Resources: An Introduction 15, Society of Economic Geologists, Special Publication, pp. 1–4, 2010.

[4] M.B. Mooiman, K.C. Sole, N. Dinham, The precious metals industry: global challenges, responses, and prospects, in: R.M. Izatt (Ed.), Metal Sustainability: Global Challenges, Consequences, and Prospects, J. Wiley, pp. 361–396, 2016.

[5] https://mining.ca/our-focus/critical-minerals/. Accédé in June 15, 2022.

[6] D.A. Cremers, L.J. Radziemski, Handbook of laser-induced breakdown spectroscopy, J. Wiley, pp 437, 2013.

[7] S. Buckley. Geochemical analysis using laser-induced breakdown spectroscopy. Spectroscopy, vol. 36, pp. 9–15, 2021.

[8] S. Selmani, N. Mohamed, I. Elhamdaoui, J. Fernandes, P. Bouchard, M. Constantin, M. Sabsabi, F. Vidal, Laser-induced breakdown spectroscopy analysis of palladium in rock ore. Spectrochim. Acta Part B, 196, pp. 106523, 2022.

[9] P.D. Maker, R.W. Terhune, C.M. Savage, Proceedings of Third International Conference on Quantum Electronics, Paris, Columbia University Press, New York, Vol. VI, Pt. 2, pp. 209-374, 1964.

[10] M. Young, M. Hercher, C.-Y. Yu, Some Characteristics of Laser-Induced Air Sparks, J. Appl. Phys, vol. 37, pp. 4938, 1966.

[11] A. Felske, W.-D. Hagenah, K. Laqua, Spectrochimica Acta Partie B : Spectroscopie atomique, vol. 27, pp. E1-E10, 1972.

[12] D. A. Cremers, L. J. Radziemski, and T. R. Loree, Spectrochemical Analysis of Liquids Using the Laser Spark, Appl. Spectrosc, vol. 38, 721-729, 1984.

[13] J. R. Wachter, D. A. Cremers, Determination of Uranium in Solution Using Laser-Induced Breakdown Spectroscopy, Appl. Spectrosc, vol. 41, pp. 1042-1048, 1987.

[14] H. A. Archontaki and S. R. Crouch, Evaluation of an Isolated Droplet Sample Introduction System for Laser-Induced Breakdown Spectroscopy, Appl. Spectrosc, vol. 42, pp.741-746, 1988.

[15] L.J. Radziemski, T.R. Loree, Laser-induced breakdown spectroscopy: Time-resolved spectrochemical applications, J. Plasma Chem. Plasma Proc, tome 1, pp.281-293, 1981.

[16] D.A. Cremers, L.J. Radziemski, Detection of chlorine and fluorine in air by laser-induced breakdown spectrometry, Anal. Chem, vol.55, pp.1252, 1983.

[17] L.J. Radziemski, D.A. Cremers, T.R. Loree, Detection of beryllium by laser-induced-breakdown spectroscopy, Spectrochim. Acta Part B, vol. 38, 349-355, 1983.

[18] D.A. Cremers, L.J. Radziemski, Appl. Spectrosc, Direct Detection of Beryllium on Filters Using the Laser Spark, vol. 39, pp. 57, 1985.

[19] R. Wisbrun, I. Schechter, R. Niessner, H. Schroeder, and K. L. Kompa, Anal. Chem, Detector for Trace Elemental Analysis of Solid Environmental Samples by Laser Plasma Spectroscopy, vol. 66, pp. 2964-2975, 1994.

[20] A. Ciucci, V. Palleschi, S. Rastelli et al, Trace pollutants analysis in soil by a time-resolved laser-induced breakdown spectroscopy technique, Appl. Phys. B –Las. Opt, vol. 63, pp.185-190, 1996.

[21] I. B. Gornushikin, J. I. Kim, B. W. Smith, S. A. Baker and Winefordner, Determination of Cobalt in Soil, Steel, and Graphite Using Excited-State Laser Fluorescence Induced in a Laser Spark, Appl. Spectrosc, vol. 51, pp. 1055 1997.

[22] F. Hilbk-Kortenbruck, R. Noll, P. Wintjens, H. Falk, and C. Becker, Analysis of heavy metals in soils using laser-induced breakdown spectrometry combined with laser-induced fluorescence, Spectrochim. Acta Part B, vol. 56, pp. 933-945, 2001.

[23] C. Aragon, J.A. Aguilera, J. Campos, Appl. Spectrosc, Determination of Carbon Content in Molten Steel Using Laser-Induced Breakdown Spectroscopy, vol. 47, pp. 606-608, 1993.

[24] J.A. Aguilera, C. Aragon, J. Campos, Determination of Carbon Content in Steel Using Laser-Induced Breakdown Spectroscopy, Appl. Spectrosc, vol. 46, pp. 1382-1387, 1992.

[25] M. Sabsabi, P. Cielo, Quantitative Analysis of Aluminum Alloys by Laser-Induced Breakdown Spectroscopy and Plasma Characterization, Appl. Spectrosc, vol. 49, pp. 499, 1995.

[26] R. Sattmann, I. Mönch, H. Krause, R. Noll, S. Couris, A. Hatziapostolou, A. Mavromanolakis, C. Fotakis, E. Larrauri, and R. Miguel, Laser-Induced Breakdown Spectroscopy for Polymer Identification, Appl. Spectrosc, vol. 52, pp. 456-46, 1998.

[27] I. Mönch, R. Noll, R. Buchholz, and J. Worringer, Laser identifies steel grades, Fraunhofer, vol. 12, pp. 25 2000.

[28] H. Fink, U. Panne and R. Niessner, Analysis of recycled thermoplasts from consumer electronics by laser-induced plasma spectroscopy, Anal. Chem. Acta, vol. 440, pp. 17-25, 2001

[29] C. M. Davies, H. H. Telle and A. W. Williams, Remote in situ analytical spectroscopy and its applications in the nuclear industry, J. Anal. Chem, vol. 355, pp. 895-899, 1996.

[30] A. I. Whitehouse, J. Young, I. M. Botheroyd, S. Lawson, C. P. Evans and J. Wright, Remote material analysis of nuclear power station steam generator tubes by laser-induced breakdown spectroscopy, Spectrochim. Acta Part B, vol. 56, pp. 821-830, 2001.

[31] L. Salmon, Analyse LIBS en milieu nucléaire, présentation aux Journées LIBS, Bordeaux, France pp.18- 19, Mai, 2009.

[32] J. Hybl, G. Lithgow, and S. G. Buckley, Laser-Induced Breakdown Spectroscopy Detection and Classification of Biological Aerosols, Appl. Spectrosc, vol. 57, pp. 1207-1215, 2003.

[**33]** A. C. Samuels, F. C. De Lucia, Jr., K. L. McNesby, and A. W. Miziolek, Laser-induced breakdown spectroscopy of bacterial spores, molds, pollens, and protein: initial studies of discrimination potential, Appl. Opt, vol. 42, pp. 6205-6209, 2003.

[34] S. Morel, N. Leon, P. Adam, and J. Amouroux, Detection of bacteria by time-resolved laser-induced breakdown spectroscopy, Appl. Opt, vol. 42, pp. 6184-6191, 2003.

[35] C. A. Munson, F. C. De Lucia Jr., T. Piehler, K. L. McNesby, and A. W. Miziolek, Investigation of statistics strategies for improving the discriminating power of laser-induced breakdown spectroscopy for chemical and biological warfare agent simulants, Spectrochim. Acta, Part B, vol. 60, pp. 1217-1224, 2005.

[36] M. Baudelet, L. Guyon, J. Yu, J. P. Wolf, T. Amodeo, E. Fréjafon, P. Laloi, Spectral signature of native CN bonds for bacterium detection and identification using femtosecond laser-induced breakdown spectroscopy, Appl. Phys. Lett, vol. 88, pp. 063901, 2006.

[37] M. Baudelet, L. Guyon, J. Yu, J. P. Wolf, T. Amodeo, E. Fréjafon, P. Laloi, Femtosecond time-resolved laser-induced breakdown spectroscopy for detection and identification of bacteria: A comparison to the nanosecond regime, J. Appl. Phys, vol. 99, pp. 084701, 2006.

[38] M. Baudelet, L. Guyon, J. Yu, J. P. Wolf, T. Amodeo, E. Fréjafon, P. Laloi, Discrimination of microbiological samples using femtosecond laser-induced breakdown spectroscopy, Appl. Phys. Lett, vol. 89, pp. 163903, 2006.

[39] R. S. Harmon, F. C. DeLucia Jr., A. LaPointe, R. J. Winkel Jr., A. W. Miziolek, LIBS for landmine detection and discrimination, Anal. Bioanal. Chem, vol. 385, pp. 1140-1148, 2006.

[40] F. C. De Lucia Jr., R. S. Harmon, K. L. McNesby, R. J. Wonkel Jr., A. W. Miziolek, Laser-induced breakdown spectroscopy analysis of energetic materials, Appl. Opt, vol 42, 6148-6152, 2003.

[41] A. Portnov, S. Rosenwaks, I. Bar, Emission following laser-induced breakdown spectroscopy of organic compounds in ambient air, Appl. Opt, vol. 42, pp. 2835-2842, 2003.

[42] C. Lopez-Moreno, S. Palanco, J. J. Laserna, F. DeLucia Jr., A. Miziolek, J. Rose, R. A. Walter, A. I. Whitehouse, Test of a stand-off laser-induced breakdown spectroscopy sensor for the detection of explosive residues on solid surfaces, J. Anal. At. Spectrom, vol. 21, pp. 55-66, 2006.

[43] C.B. Dreyer, G. S. Mungas, P. Thanh, and J.G. Radziszewski, Study of sub-mJ-excited laser-induced plasma combined with Raman spectroscopy under Mars atmosphere-simulated conditions, Spectrochim. Acta Part B, vol. 62, pp.1448-1459, 2007.

[44] A. K. Knight, N. L. Scherbarth, D. A. Cremers, and M. J. Ferris, Characterization of Laser-Induced Breakdown Spectroscopy (LIBS) for Application to Space Exploration, Appl. Spectrosc, vol. 54, pp. 331-340, 2000.

[45] F. Colao, R. Fantoni, V. Lazic, A. Paolini, F. Fabbri, G.G. Ori, L. Marinangeli, A. Baliva, Investigation of LIBS feasibility for in situ planetary exploration: An analysis on Martian rock analogues, Planetary and Space Science, vol. 52, pp. 117-123, 2004.

[46] B. Sallé, D. A. Cremer, S. Maurice, R. C. Wens, Laser-induced breakdown spectroscopy for space exploration applications: Influence of the ambient pressure on the calibration curves prepared from soil and clay samples, Spectrochim. Acta Part B, vol. 60, pp. 479-490, 2005.

[47] J. B. Sirven, B. Sallé, P. Mauchien, J. L. Lacour, S. Maurice, G. Manhès, Feasibility study of rock identification at the surface of Mars by remote laser-induced breakdown spectroscopy and three chemometric methods, J. Anal. At. Spectrom, vol. 22, pp. 1471-1480, 2007.

[48] N. Khajehzadeh. and T. Kauppinen, Fast mineral identification using elemental LIBS technique. IFAC-Papers Online, vol. 48, pp. 119–124, 2015.

[49] R.S. Harmon, C.J.M. Lawley, J. Watts, C.T. Harraden, A.M. Somers, R.R. Hark, Laser-induced breakdown spectroscopy – an emerging analytical tool for mineral exploration. Minerals, vol 9(12), pp.718, 2019.

[50] F.F. Fontana, B. van der Hoek, S. Tassios, C. Tiddy, J. Stromberg, N. Francis, Y.A. Uvarova, D.G. Lancaster, Laser-Induced Breakdown Spectroscopy (LIBS) for whole rock geochemistry. J. Geochem. Explor, Vol. 246, pp. 107160, 2023.

[51] K. Rifai, F. Doucet, L. Ozcan, F. Vidal, LIBS core imaging at kHz speed: paving the way for real-time geochemical applications. Spectrochim. Acta Part B, vol. 150, pp. 43–48, 2018.

[52] K. Kuhn, J.A. Meima, D. Rammlmair, C. Ohlendorf, Chemical mapping of mine waste drill cores with laser-induced breakdown spectroscopy (LIBS) and energy dispersive X-ray fuorescence (EDXRF) for mineral resource exploration. J. Geochem. Explor, vol. 161, pp.72–84, 2016.

[53] R. S. Harmon, Laser-Induced Breakdown Spectroscopy in Mineral Exploration and Ore Processing, Minerals, vol. 14(7), pp. 731, 2024.

[54] R.S. Harmon, F.C. De Lucia, A.W. Miziolek, K.L. McNesby, R.A. Walters, P.D. French, Laser-induced breakdown spectroscopy (LIBS)—An emerging field-portable sensor technology for real-time, in-situ geochemical and environmental analysis. Geochem. Explor. Environ. Anal. vol 5(1), pp. 21–28, 2005.

[55] Harmon, R.S.; Russo, R.E. Laser-induced breakdown spectroscopy. In Treatise on Geochemistry, Analytical Geochemistry and Inorganic Instrumental Analysis; McDonough, W., Ed.; Elsevier: Amsterdam, The Netherlands, vol. 15, pp. 245–272, 2014.

[56] C. Fabre, Advances in Laser-Induced Breakdown Spectroscopy analysis for geology: A critical review. Acta Part B At. Spectrosc, vol. 166, pp.105799, 2020.

[57] R.S. Harmon, G.S. Senesi, Laser-induced breakdown Spectroscopy—A geochemical tool for the 21st century. Appl. Geochem, vol. 128, pp. 104929, 2021.

[58] S. Rosenwasser, G. Asimellis, B. Bromley, R. Hazlett, J. Martin, T. Pearce, A. Zigler, Development of a method for automated quantitative analysis of ores using LIBS. Spectrochim. Acta Part B At. Spectrosc, vol 56, pp. 707–714, 2001.

[59] Death, D.L.; Cunningham, A.P.; Pollard, L.J. multi-element and mineralogical analysis of mineral ores using laser induced breakdown spectroscopy and chemometric analysis. Spectrochim. Acta Part B At. Spectrom, vol. 64, pp. 1048–1058, 2009.

[60] O. Haavisto, T. Kauppinen, H. Häkkänen, Laser-induced breakdown spectroscopy for rapid elemental analysis of drill core. IFAC-PapersOnLine, vol. 46, pp. 87–91, 2013.

[61] P. Porízka, A. Demidov, J. Kaiser, J. Keivanian, I. Gornushkin, U. Panne, J. Riedel, Laser-induced breakdown spectroscopy for in situ qualitative and quantitative analysis of mineral ores. Spectrochim. Acta Part B At. Spectrom, vol. 101, pp. 155–163, 2014.

[62] J.D. Pedarnig, S. Trautner, S. Grünberger, N. Giannakaris, S. Eschlböck-Fuchs, J. Hofstadler, Review of element analysis of industrial materials by in-line laser-induced breakdown spectroscopy (LIBS). Appl. Sci, vol 11, pp. 9274, 2021.

[63] L. Barrette, S. Turmel, On-line iron-ore slurry monitoring for real-time process control of pellet making processes using laser-induced breakdown spectroscopy: Graphitic vs. total carbon detection. Spectrochim. Acta Part B At. Spectrom, vol. 56, pp. 715–723, 2001.

[64] K.E. Eseller, M.M.Tripathi, F.Y. Yueh, J.P. Singh, Elemental analysis of slurry samples with laser induced breakdown spectroscopy. Appl. Opt, vol. 49, pp. C21–C26, 2010.

[65] N. Khajehzadeh, O. Haavisto, L. Koresaar, On-stream and quantitative mineral identification of tailing slurries using LIBS technique, Miner. Eng, vol. 98, pp.101–109, 2016.

[66] X. Cheng, X. Yang, Zhu, Z. Guo, L. Li, X. Lu, Y. Zeng, X. On-stream analysis of iron ore slurry using laser-induced breakdown spectroscopy. Appl. Opt, vol. 56, pp. 9144–9149, 2017.

[67] C.R.Ytsma, C.A. Knudson, M.D. Dyar, A.C. McAdam, D.D. Michaud, L.M. Rollosson, Accuracies and detection limits of major, minor, and trace element quantification in rocks by portable laser-induced breakdown spectroscopy. Spectrochim. Acta Part B At. Spectrom, vol. 171, pp. 105946, 2020.

[68] C. Fabre, P. Mauchien, S. Grégoire, and C. Pinard. In Situ Quantitative Analysis of Ore Samples Using a Portable LIBS Instrument. Spectrochimica Acta Part B: Atomic Spectroscopy, vol.101, pp. 9-18, 2014.

[69] S. M. Clegg, R. C. Wiens, J. E. Barefield, and D. Vaniman,. Laser-Induced Breakdown Spectroscopy (LIBS): Capabilities for Rapid, In Situ Geochemical Analysis. Spectroscopy, vol. 24(4), pp. 32-39, 2009.

[70] J. Pierce, E. Diaz, and P. Schaffer, Field Portable LIBS Analyzer for Rapid Elemental Analysis of Geological Samples. Journal of Analytical Atomic Spectrometry, vol. 31(12), pp. 2591-2602, 2016.

[71] R.S. Harmon, R.E. Russo, R.R. Hark, Applications of laser-induced breakdown spectroscopy for geochemical and environmental analysis: a comprehensive review, Spectrochim. Acta Part B, vol. 87, pp. 11–26, 2013.

[72] R.S. Harmon, J.M. Lawley C, J. Watts, C.T. Harraden, A.M. Somers, R.R. Hark, Laser-induced breakdown spectroscopy – an emerging analytical tool for mineral exploration, Minerals, vol. 9, pp. 718. 2019.

[73] A. Harhira, P. Bouchard, K. Rifai, J. El Haddad, M. Sabsabi, A. Blouin, M. Lafamme, Advanced Laser-induced breakdown spectroscopy (LIBS) sensor for gold mining. In Proceedings of the Conference of Metallurgists (COM), Vancouver, BC, Canada, pp. 27–30, 2017.

[74] K. Rifai, M. Lafamme, M. Constantin, F. Vidal, M. Sabsabi, A. Blouin, P. Bouchard, K. Fytas, M. Castello, B. NguegangKamwa, Analysis of gold in rock samples using laser-induced breakdown spectroscopy: matrix and heterogeneity efects. Spectrochim. Acta Part B. vol. 134, pp. 33–41, 2017.

[75] I. Elhamdaoui, K. Rifai, J. Iqbal, N. Mohamed, S. Selmani, J. Fernandes, P. Bouchard, M. Constantin, M. Lafamme, M. Sabsabi, F. Vidal, Measuring the concentration of gold in ore samples by laser-induced breakdown spectroscopy (LIBS) and comparison with the gravimetry/ atomic absorption techniques. Spectrochim. Acta Part B, vol. 183, pp. 106256, 2021.

[76] I. Elhamdaoui, N. Mohamed, S. Selmani, P. Bouchard, M. Sabsabi, M. Constantin, F. Vidal, Rapid quantitative analysis of palladium in ores using Laser-Induced Breakdown Spectroscopy assisted with laser-induced fuorescence (LIBS-LIF). J. Anal. At. Spectrom. Vol. 37, pp. 2537, 2022.

[77] I. Elhamdaoui, S. Selmani, M. Sabsabi, M. Constantin, P. Bouchard, F. Vidal, Rapid Quantifying Platinum and Palladium in Solid Ore Using Laser-Induced Breakdown Spectroscopy Assisted by the Laser-Induced Fluorescence (LIBS-LIF) Technique. Applied Spectroscopy Vol. 77(12), pp. 1382–1392, 2023,

[78] S. Selmani, I. Elhamdaoui, N. Mohamed, J. Fernandes, P. Bouchard, M. Constantin, M. Sabsabi, F. Laser-produced craters in minerals of a palladium ore sample, Applied Physics A, vol. 129, pp. 737, 2023.

[79] P. Bouchard, M. Sabsabi, C. Padioleau, A. Blouin, “Hybrid LIBS System and method for gold ore mineral analysis”. US provisional application Filed in May 2018. NRC 2018–068, published November 2019—US patent 11,385,182 issued July 2022.

[80] P. Bouchard, M. Sabsabi, C. Padioleau, “High resolution and high throughput spectrometer”. US provisional application (NRC 2018–093). Filed May 2018, published October 2019. US patent 11,385,101 issued July 2022.

[81] D. Cremers, L. Radziemski, Handbook of Laser-Induced Breakdown Spectroscopy; Wiley: Hoboken, NJ, USA, 2013.

[82] A. Nardecchia, C.Fabre, J. Cauzid, F.Pelascini, V. MottoRos and L. Duponchel, Detection of minor compounds in complex mineral samples from millions of spectra: A new data analysis strategy in LIBS imaging. Analytica Chimica Acta, 1114, 66–73 2020.

[83] K. Rifai, F. Doucet, L. Ozcan, F. Vidal, LIBS core imaging at kHz speed: paving the way for real-time geochemical applications, Spectrochim. Acta Part B, vol. 150, pp. 43–48, 2018.

[84] D.W. Hahn, N. Omenetto, Laser-induced breakdown spectroscopy (LIBS), part II: Review of instrumental and methodological approaches to material analysis and applications to different fields. Appl. Spectrosc, vol. 66, pp. 347–419, 2012.

[85] B. Marshall, “F&F 2015: Facts and Figures of the Canadian Mining Industry”, pp. 97, 2015.

CHAPITRE II

2 SPECTROSCOPIE DES PLASMAS INDUITS PAR LASER (LIBS)

Depuis près de 30 ans, les techniques d'analyse basées sur l'ablation laser, qui comprennent la LIBS conventionnelle, la LIBS couplée à la fluorescence induite par laser, la LIBS à double impulsions, etc., se sont considérablement développées en raison de l'avantage majeur qu'elles présentent : la possibilité d'analyser directement les matériaux sans nécessiter de préparation de l'échantillon. Il est à noter que l'ablation laser ne produit pas de rejets toxiques et nécessite une quantité de matière bien moindre par rapport à une mise en solution. Rappelons que dans la technique LIBS conventionnelle, un faisceau laser de haute intensité est focalisé sur la surface d'un échantillon pour vaporiser une petite quantité de matière. Cette interaction génère un plasma lumineux, composé d'ions, d'électrons et d'atomes excités, dont le spectre de lumière émise est ensuite analysé.

Ce chapitre est consacré à une étude bibliographique des différents aspects de la LIBS conventionnelle. Nous aborderons d'abord les concepts importants pour sa mise en œuvre, puis nous discuterons brièvement des principes physiques qui forment notre compréhension des mécanismes physiques à la base de cette technique.

2.1 Principe de la technique LIBS

Le principe général de la LIBS est représenté à la figure 2.1. Il consiste à focaliser un faisceau laser sur la surface d'un échantillon de nature solide, liquide ou gazeux [1] afin de créer un plasma et d'analyser le spectre de la lumière émise par le plasma. Les lasers utilisés en LIBS sont généralement du type Nd:YAG, ayant des impulsions de quelques nanosecondes et une longueur d'onde de 1064 µm. Des impulsions plus brèves sont utilisées pour des applications spécifiques de la LIBS, comme pour des mesures très localisées, mais elles sont plus coûteuses à produire et généralement considérées comme moins efficaces en raison de l'absence d'interaction du laser avec le plasma crée à la surface du matériau. Lorsque la densité d'énergie laser est suffisante, le matériau est alors vaporisé au niveau du point focal. Dans le cas des impulsions laser nanosecondes généralement utilisées en LIBS, le laser ionise et chauffe la vapeur qui se développe au-dessus de la surface de l'échantillon, initiant ainsi un plasma dans lequel les ions, atomes et molécules sont excités (figure 2.1A). Lorsque l'impulsion laser est terminée, le plasma poursuit son expansion dans l'atmosphère ambiante en se refroidissant. Les atomes et les ions présents dans le plasma se désexcitent spontanément en émettant un rayonnement lumineux composé de raies et d'un fond continu. Un dispositif optique, composé d'une lentille et d'une fibre

optique, collecte cette lumière et l'achemine vers un spectromètre, où elle est décomposée en un spectre de raies dans la gamme de longueurs d'onde ultraviolet – visible, jusqu'au proche infrarouge (200 – 800 nm), puis vers un détecteur qui enregistre le spectre (figure 2.1B). Ce spectre composé de raies d'émission atomique (figure 2.1C) permet alors de déterminer qualitativement et quantitativement (figure 21.D) la composition de l'échantillon.

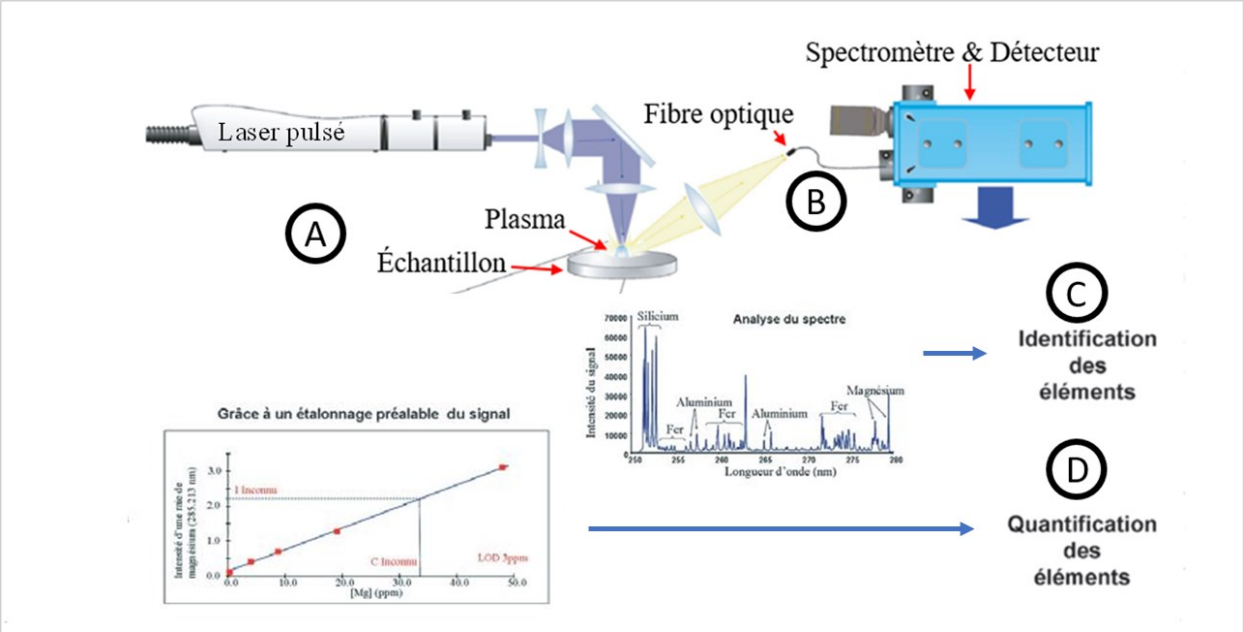

Figure 2-1 Principe expérimental du LIBS conventionnel [2].

2.1.1 Analyse qualitative et quantitative

La technique LIBS permet de réaliser des analyses qualitatives visant à identifier tel ou tel élément dans un échantillon ou bien à identifier un matériau à l'aide des raies d'émission qui constituent la signature propre à chaque élément chimique. L'analyse quantitative en LIBS repose sur la capacité de cette technique à déterminer la concentration des éléments présents dans un échantillon. Dans les deux cas, ce processus implique plusieurs étapes clés, dont la calibration de l'instrument (longueur d'onde, reproductibilité du signal) l'optimisation du montage (maximisation du rapport signal sur bruit, minimisation de la limite de détection), la collecte et le traitement des données spectrales (identification des raies spectrales au moyen de bases de données, normalisation des spectres), ainsi que l'interprétation des résultats obtenus. L'analyse quantitative requiert une étape supplémentaire : comme dans la plupart des techniques de chimie analytique, la détermination quantitative de la composition élémentaire d'un échantillon par LIBS consiste à tracer une courbe d'étalonnage [3] à l'aide de matériaux de référence (MR) certifiés,

c’est-à-dire dont les concentrations des éléments d’intérêt ont été déterminées avec précision au moyen de techniques analytiques conventionnelles.

2.1.2 Courbe de calibration ou d'étalonnage

La calibration au moyen de MR certifiés consiste, dans un premier temps, à sélectionner une raie spectrale de l'élément dont on veut connaître la concentration (analyte dans l’échantillon), puis dans un second temps à représenter l'intensité du signal émis par cet élément en fonction de sa concentration dans des étalons, c'est-à-dire des échantillons dont les concentrations sont connues avec une grande précision. En associant l'intensité émise par l’élément à analyser (en concentration inconnue dans un échantillon d'analyse) et la courbe de calibration préalablement obtenue, on peut ainsi remonter à la concentration de l'élément chimique (figures 2.1D et 2.2). On caractérise alors la réponse du système d'analyse par la limite de détection (LoD).

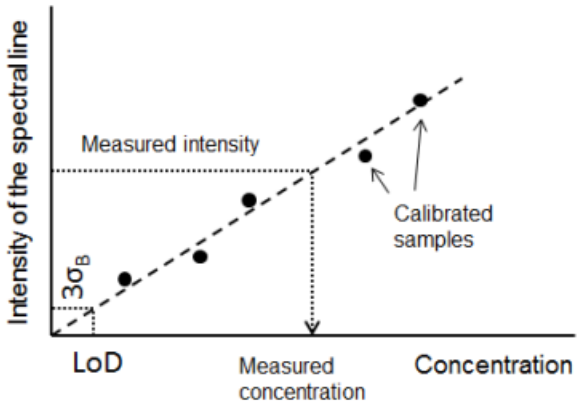

Figure 2-2 Principe de la courbe d’étalonnage

2.1.3 Limite de détection (LoD)

La LoD est un paramètre fondamental en LIBS car il indique la plus petite concentration de l’élément d’intérêt qu’il est possible de détecter dans le type de matrice étudié. La LoD d'une analyse LIBS est déterminée par le rapport signal-bruit (S/N) des raies spectrales. Elle est définie comme étant la plus faible concentration de l’élément à déterminer qui donne un signal trois fois supérieur à l’écart-type σ_B du bruit de fond associé aux spectres (figure 2.2). Ce bruit de fond est mesuré dans une plage spectrale exempte de raies. Il provient des processus aléatoires qui se produisent dans le plasma, tels que les processus collisionnels, la recombinaison radiative, le rayonnement du corps noir, les instabilités du plasma, etc., ainsi que dans l’appareillage

électronique, notamment dans la caméra associée au spectromètre. Connaissant la pente p de la courbe de calibration, obtenue par le detecteur, la LoD s'obtient par l'expression

$$\mathrm{LoD} = \frac{3\sigma_B}{p} \tag{2.1}$$

Le σ_B est déterminée dans les mêmes conditions expérimentales que la mesure des intensités des raies spectrales, en utilisant un échantillon ne contenant pas d'analyte (nommé « blank » en anglais) à la même position spectrale ou dans une région du spectre située à proximité de la raie d'analyse, mais libre de toutes autres raies spectrales. On peut démontrer mathématiquement que toute valeur du signal associé à une raie d'émission supérieure à $3\sigma_B$ aura 99% de chance d'être due à la présence effective de l'élément à analyser. Cette convention, communément acceptée par les chimistes, est basée sur les recommandations de l'IUPAC (« International Union of Pure and Applied Chemistry ») [4]. En raison de la nature aléatoire du bruit, la somme des signaux de N tirs laser fait croitre le bruit comme $\sqrt{N}$ alors que la somme des signaux des raies croit comme N. Par conséquent, la LoD diminue comme $1/\sqrt{N}$.

La LoD est très variable en fonction de l'élément analysé ou de la matrice dans laquelle se trouve cet élément, mais aussi en fonction de la longueur d'onde de la raie mesurée. D'autres paramètres, sont susceptibles de faire varier l'intensité de la raie d'émission utilisée pour obtenir la courbe de calibration, comme les paramètres instrumentaux, les conditions de mesure telles que la longueur d'onde, la distance de focalisation, le type de spectromètre et de détecteur, les paramètres temporels de mesure, le traitement des données, etc. De plus, le signal LIBS peut être affecté par différents phénomènes. En effet, les fluctuations de l'énergie du laser ou l'homogénéité des échantillons solides peuvent faire varier significativement l'intensité de la raie d'émission. Pour s'affranchir de ce type d'effets, il est possible d'accumuler les tirs laser et les sites d'ablation, et par conséquent, d'accumuler les acquisitions. Plusieurs techniques de normalisation interne sont utilisées dans la littérature pour atténuer ces effets, comme par exemple l'utilisation du rapport entre l'intensité nette de la raie de l'élément à déterminer (le fond soustrait l'intensité brute de la raie) et le fond ou une raie d'un élément dont la concentration est à peu près constante dans tous les échantillons.

Il est à noter que l'utilisation de la méthode des courbes de calibration pour la détermination de la composition chimique d'un échantillon inconnu nécessite, d'une part, de disposer d'étalons certifiés de composition parfaitement connue, et, d'autre part, il faut que l'échantillon à analyser soit de même nature que les étalons. Dans le cas contraire, des effets de matrice peuvent perturber l'interprétation des données expérimentales.

2.1.4 Effets de matrice

En LIBS, les effets de matrice désignent l'influence de la composition chimique et physique de l'échantillon sur le signal d'un élément donné. Ces effets peuvent compliquer l'analyse quantitative et nuire à la précision des résultats. Ils sont essentiellement dus aux variations des propriétés thermodynamiques, physiques et optiques des matériaux en fonction de leur composition. La présence d'éléments ou de composés différents dans un échantillon peut également altérer les intensités des raies spectrales. Par exemple, des éléments à forte énergie de liaison peuvent nécessiter plus d'énergie pour être ablatés, modifiant ainsi le signal LIBS. La variation de la concentration des éléments de matrice peut également affecter l'ionisation et l'excitation des espèces analytiques dans le plasma, et donc modifier les intensités des raies spectrales. Les valeurs de la température d'excitation et de la densité d'atomes et d'électrons dans le plasma peuvent alors différer. Ces variations de comportement d'un matériau à l'autre induisent directement des variations du signal d'émission du plasma. Ainsi, pour une même concentration d'un élément donné dans deux matrices de compositions différentes, les intensités des raies d'émission mesurées seront différentes. Les pentes des droites d'étalonnages seront alors différentes pour chacune des matrices. Ce point souligne une limitation de la quantification à l'aide de courbes d'étalonnage : un instrument LIBS calibré sur une matrice particulière ne donnera à priori pas les mêmes valeurs de concentration pour des mesures dans une matrice différente. Les mesures quantitatives sur une matrice inconnue sont par conséquent très délicates. Les effets de matrice représentent un défi significatif pour l'analyse quantitative par LIBS. Notons cependant que ces effets de matrice se retrouvent dans la plupart des techniques d'analyse.

Dans le cas où le nombre d'échantillons de calibration est suffisamment élevé et que ces derniers sont représentatifs d'une variété de matrices pertinentes, il est possible d'utiliser un algorithme d'apprentissage machine, comme par exemple un réseau de neurones artificiels (ANN), pour associer plusieurs raies de l'analyte ainsi que des raies d'autres éléments présents dans la matrice, à la concentration de l'analyte et ainsi prédire la concentration de l'analyte dans un échantillon inconnu. Cependant, comme la préparation des échantillons de calibration est généralement un processus long, complexe et qui peut s'avérer coûteux en raison du prix élevé des MR certifiés, le nombre de ces échantillons est alors restreint et il est nécessaire de recourir à des solutions alternatives. Celle que nous avons utilisé dans cette thèse consiste à établir trois courbes de calibration pour trois matrices différentes, puis de se référer à la plus pertinente par la comparaison entre le spectre de l'échantillon inconnu et ceux des MR.

2.1.5 Auto-absorption

L'auto-absorption des raies est un phénomène important à considérer dans les analyses spectroscopiques, notamment en LIBS. Comme le nom l'indique, l'auto-absorption se produit lorsque les photons émis lors de la désexcitation spontanée d'un élément chimique sont absorbés par le même élément dans le plasma. Le rayonnement se trouve piégé dans le plasma. Cet effet est d'autant plus important que la densité d'atomes de l'élément considéré au sein du plasma est élevée. Ceci a pour effet de diminuer le taux d'émission spontané effectif des raies car les états excités sont continuellement pompés par la réabsorption des photons, ce qui conduit à une diminution de l'intensité des raies. Lorsque les photons sont principalement émis dans une partie chaude du plasma (raies élargies par les effets Stark, Doppler et collisionnels) et absorbés puis réémis par des atomes dans une région plus froide du plasma, nous observons alors un aplatissement des raies, voire un creux au sommet des raies, qui conduit à un élargissement apparent des raies à mi-hauteur. Les plasmas induits par laser sont en effet inhomogènes : il existe un gradient de température et de densité électronique au sein du plasma, les zones centrales étant beaucoup plus chaudes que les zones périphériques [5-7]. La densité d'atomes dans un état excité est importante au centre du plasma, tandis que la périphérie du plasma, plus froide, contient principalement des atomes dans leur état fondamental. Dans cette situation, un photon émis par un atome depuis une zone centrale du plasma a une probabilité importante d'être réabsorbé par un atome situé en périphérie du plasma. Étant donné que l'intensité mesurée de cette raie d'émission apparaît plus faible que l'intensité réellement émise par le plasma et que cet effet est d'autant plus important que la densité d'atomes de l'élément considéré au sein du plasma est élevée, il se produira un infléchissement concave de la pente de la courbe d'étalonnage pour les hautes concentrations (figure 2.3).

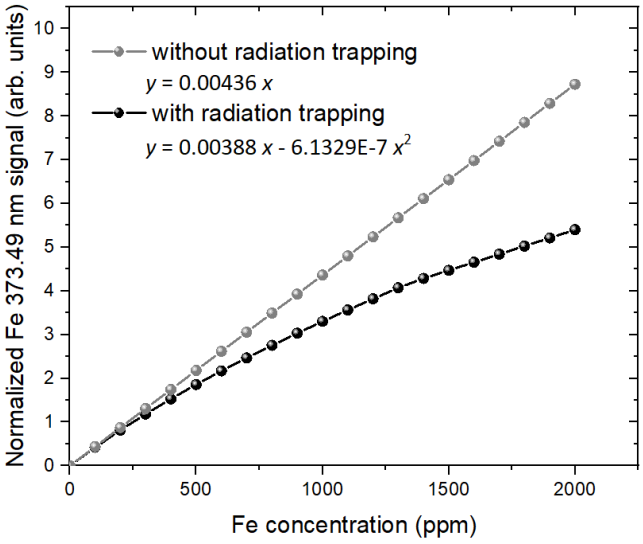

Figure 2-3 **Courbes de calibration calculées pour la raie Fe I 373.49 dans des alliages de cuivre avec et sans auto-absorption ou piégeage du rayonnement.**

2.1.6 Délai d'acquisition du signal LIBS

Un autre aspect important de la technique LIBS concerne le contrôle du début et de la fin de l'acquisition du rayonnement émis par le plasma. Comme la LIBS porte essentiellement sur la mesure et l'utilisation des raies d'émission du plasma, il est important de maximiser leur amplitude par rapport au bruit de fond afin d'obtenir les LoD optimales. Immédiatement après l'impulsion laser, la densité d'électrons est maximale, ce qui conduit à l'élargissement des raies par l'effet Stark, associé aux variations locales du champ électrique causées par la séparation aléatoire des charges à proximité des atomes émetteurs. À ce stade, les raies sont fortement élargies et elles se confondent avec le fond spectral intense et bruité (figure 2.4). À mesure que la température et la densité électronique du plasma diminuent, les raies deviennent plus nettes et se distinguent du fond continu et du bruit. C'est à ce moment que l'acquisition des spectres commence généralement, soit après environ 1 µs, dépendamment des paramètres laser utilisés. La durée totale de l'acquisition des spectres est moins critique que le début de l'acquisition. Cependant, elle peut être optimisée afin de minimiser la LoD. Généralement, le temps d'acquisition se mesure en dizaines de µs.

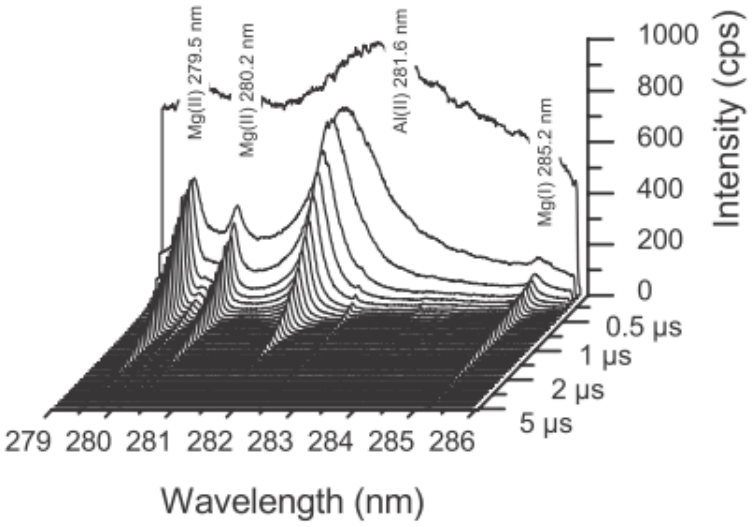

Figure 2-4 **Évolution temporelle du spectre d'émission d'un plasma provenant d'un alliage d'aluminium [8].**

2.2 Principes physiques

2.2.1 Formation du plasma

La formation d'un plasma par ablation laser repose sur plusieurs étapes et paramètres clés. La vaporisation du matériau est influencée par plusieurs facteurs, notamment la fluence laser (énergie par unité de surface), le seuil d'ablation du matériau, la durée de l'impulsion laser et la longueur d'onde utilisée. Ces paramètres ont une influence importante sur les processus fondamentaux de l'ablation incluant l'absorption de l'énergie laser, la vaporisation, l'ionisation et l'expansion du plasma. Ces étapes conduisent à la formation d'un plasma lumineux, composé d'électrons libres, d'ions et d'atomes excités (figure 2.5).

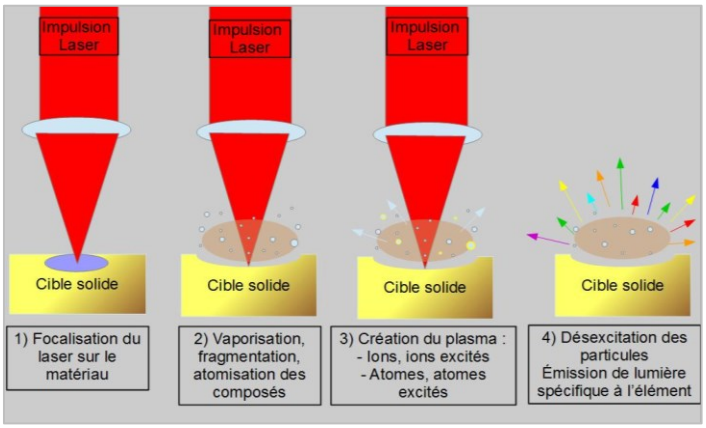

Figure 2-5 **Formation du plasma [2]**

Lorsque le faisceau laser atteint la surface du matériau, de l'énergie laser est d'abord transférée aux électrons libres par le mécanisme de Bremsstrahlung inverse où les électrons libres gagnent en moyenne leur énergie d'oscillation dans le champ laser à chaque collision avec les atomes neutres et les ions. Ce phénomène est décrit par l'expression

$$\frac{d\varepsilon_e}{dt} = \nu_{ei}\varepsilon_{osc} \tag{2.2}$$

où ε_e est la densité d'énergie des électrons, ν_{ei} est la fréquence de collision entre les électrons et les ions (qui peuvent aussi être des atomes neutres) et ε_{osc} est la densité d'énergie d'oscillation des électrons dans le champ laser, donnée par l'expression

$$\varepsilon_{osc} = \frac{1}{2}N_e m_e \left(\frac{e\lambda E}{2\pi c m_e}\right)^2 \tag{2.3}$$

où N_e est la densité d'électrons, E est le champ électrique du laser, λ est sa longueur d'onde, e est la charge de l'électron et m_e est sa masse. Considérant que l'intensité laser I (puissance par unité de surface) est proportionnelle à E^2, le taux d'absorption de l'énergie laser est donc proportionnel à $I\lambda^2$, ce qui signifie qu'une intensité et une longueur d'onde élevées seront favorables à la formation d'un plasma chaud et dense qui est généralement favorable aux mesures LIBS.

Les électrons libres peuvent être initialement présents dans le matériau (métaux ou semi-conducteurs) ou produits par photoionisation par le laser lui-même. Les électrons énergétiques transfèrent ensuite leur énergie aux atomes provoquant ainsi une élévation rapide de la température et vaporisant une petite quantité de matière. Les électrons énergétiques peuvent également ioniser les atomes et les ions par collision, causant une avalanche électronique, qui accélère l'absorption de l'énergie laser en vertu de l'équation (2.3). La densité d'électrons peut éventuellement excéder la densité critique du plasma pour la longueur d'onde du laser (i.e. la densité électronique seuil où le laser est réfléchi), faisant en sorte que le plasma devienne partiellement, voire totalement opaque au faisceau laser, le matériau reçoit alors moins d'énergie laser et donc la vaporisation à sa surface ralentit.

La fluence du laser, définie comme l'énergie par unité de surface, doit dépasser un certain seuil pour initier l'ablation du matériau. Ce seuil d'ablation varie en fonction des propriétés de l'impulsion laser telles que sa durée et sa longueur d'onde ainsi que des propriétés physiques et chimiques du matériau. Chaque matériau possède un seuil d'ablation spécifique, qui se trouve typiquement entre 1 et 10 J cm^{-2} pour les diélectriques et les semi-conducteurs [9] dans le cas d'impulsions laser nanosecondes à une longueur d'onde d'environ 1 µm. Il est établi que le seuil

d'ablation augmente comme la racine carrée de la durée d'impulsion en raison de la conduction thermique dans la cible [10].

2.2.2 Émission de rayonnement

Comme illustré à la figure 2.6, l'émission du plasma est composée d'un fond spectral bruité et de raies d'émission. Les raies d'émission proviennent de la désexcitation spontanée des atomes neutres et des ions dont les électrons ont gagné les niveaux quantiques supérieurs, principalement à la suite de collisions avec les électrons libres énergétiques du plasma.

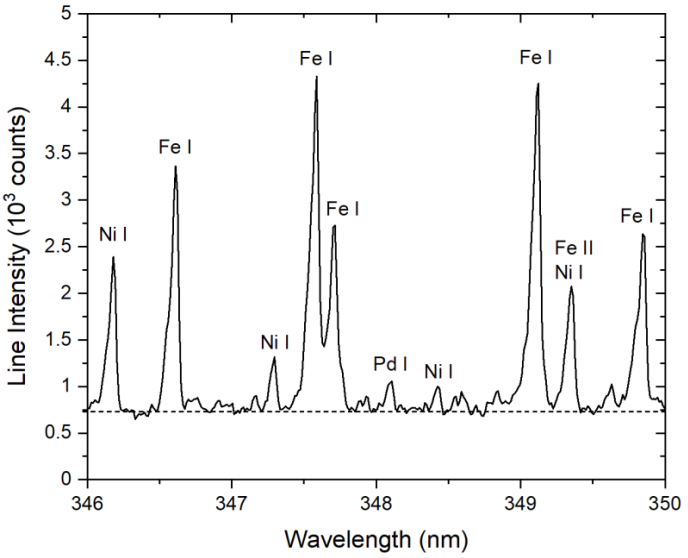

Figure 2-6 **Exemple de spectre mesuré sur le minerai près d'une raie de palladium. Les principales raies de fer, nickel et palladium sont identifiées. La ligne pointillée représente la valeur moyenne du fond spectral.**

Il est établi que, pour un plasma à l'équilibre thermodynamique local, la puissance émise par unité de volume entre les niveaux j et i s'exprime comme

$$\varepsilon_{ij} = hc\left(\frac{A_{ji}g_j}{\lambda_{ij}}\right)\frac{N_0}{U_s(T_e)}e^{-E_j/T_e} \text{ W cm}^{-3} \quad (2.4)$$

où A_{ji} est le taux de désexcitation spontanée en s^{-1}, g_j est le facteur de dégénérescence, E_j est l'énergie du niveau j en électron Volt (eV), λ_{ij} est la longueur d'onde des photons émis lors de la transition, U_s est la fonction de partition de l'espèce émissive, qui dépend de la température électronique T_e, et N_0 est la densité totale de l'espèce neutre ou ionique dans le plasma. Dans cette expression, h et c sont respectivement la constante de Planck et la vitesse de la lumière dans le vide. Cette expression indique que l'intensité des raies d'émission est proportionnelle à

la densité totale N_0 de l'espèce émissive, d'où la linéarité des courbes de calibration (négligeant les effets d'auto-absorption), et dépend des propriétés intrinsèques de chaque élément chimique par l'intermédiaire des paramètres $A_{ji}g_j$, E_j et λ_{ij}. Elle indique aussi qu'un plasma chaud favorise l'occupation de niveaux quantiques supérieurs et donc l'émission des raies spectrales. Il faut cependant se rappeler que cette expression représente une limite supérieure car elle ne tient pas compte de la désexcitation par les collisions électroniques (collisions super-élastiques).

Le fond spectral quant à lui est déterminé par l'émission Bremsstrahlung, causée principalement par la décélération des électrons passant au voisinage d'un ion. Pour des ions hydrogénoïdes de charge Z et de densité N_Z, la puissance rayonnée par unité de volume s'exprime

$$P_{Br}(Z) = 1.69 \times 10^{-32} N_e T_e^{1/2} Z^2 N_Z \quad \text{W cm}^{-3} \tag{2.5}$$

où N_e est la densité d'électrons en cm^{-3}. Par conséquent cet effet sera plus prononcé pour un plasma dense et chaud.

L'autre contribution importante au fond spectral est la recombinaison des électrons et des ions, qui s'accompagne de l'émission de rayonnement en vertu de la conservation de l'énergie. La puissance rayonnée par unité de volume lors de la recombinaison entre les électrons libres et les ions de charge Z s'exprime

$$P_r(Z) = P_{Br}\left(\frac{E_{Z-1}}{T_e}\right) \quad \text{W cm}^{-3} \tag{2.6}$$

où E_{Z-1} est l'énergie d'ionisation des ions de charge $Z-1$, cette énergie étant émise sous forme de rayonnement lorsque l'électron se recombine à l'ion, en plus de l'énergie de l'électron libre. Cette expression indique que le fond spectral est favorisé dans un plasma dense mais pas dans un plasma chaud, qui encourage plutôt l'ionisation aux dépens de la recombinaison.

2.2.3 Densité et température des électrons dans les plasmas LIBS

Comme on l'a vu dans la section précédente, dans un plasma généré par laser, la densité et la température des électrons sont des paramètres critiques qui déterminent les résultats des analyses élémentaires. Pour les plasmas produits par des lasers Nd:YAG à haute puissance, la densité d'électrons se situe généralement entre 10^{16} et 10^{19} cm^{-3}. Elle dépend de l'énergie du laser et du type de matériau ablaté. Pour des plasmas générés par des impulsions laser de quelques nanosecondes, la température des électrons varie typiquement entre 6 000 et 30 000 K (0.517 et 2.59 eV). Cette température est influencée par l'énergie de l'impulsion laser et les propriétés du matériau cible.

Après la fin de l'impulsion laser, le plasma se refroidit progressivement en raison de deux effets : le travail effectué lors de son expansion contre la pression exercée par l'air ambient, et l'émission de rayonnement. Des molécules peuvent se former lorsque le plasma est suffisamment froid. Celles ayant une forte énergie de liaison, comme C_2 ou CN, peuvent aussi exister dès les premiers instants.

La température et la densité électronique peuvent être déterminées par l'analyse des spectres d'émission du plasma. En utilisant les raies spectrales d'éléments comportant de nombreuses raies, comme le fer et le nickel, il est possible de calculer la densité et la température des électrons.

La température électronique peut être déterminée en utilisant au moins deux raies spectrales de la même espèce ionique, l'une résultant de la transition $j \rightarrow i$ et l'autre de la transition $n \rightarrow m$, en faisant le rapport de l'expression (2.4) pour ces deux raies. On obtient

$$T_e = \frac{E_j - E_n}{\ln\left(\frac{\varepsilon_{ij} A_{ji} g_j \lambda_{mn}}{\varepsilon_{mn} A_{nm} g_n \lambda_{ij}}\right)} \tag{2.7}$$

Plus de deux raies peuvent être utilisées en effectuant une régression linéaire entre toutes les données.

Pour la plupart des éléments, la densité d'électrons peut être estimée en mesurant l'élargissement des raies spectrales à mi-hauteur $\Delta\lambda_{FWHM}$ due à l'effet Stark

$$N_e \approx \frac{\Delta\lambda_{FWHM}}{2\Delta\lambda_0}\left(\frac{T_e}{T_{e0}}\right)^{1/2} N_{e0} \tag{2.8}$$

Dans cette expression, $\Delta\lambda_0$ est la largeur de la raie mesurée à la température T_{e0} et à la densité électronique N_{e0}. Ce paramètre a été mesuré pour un nombre plutôt limité de raies, dont les valeurs sont disponibles dans la littérature.

Une autre manière de déterminer la température électronique, connaissant la densité d'électrons, ou alors de déterminer la densité d'électrons, connaissant la température électronique, consiste à combiner la loi de Saha, déterminant le rapport des densités ioniques N_Z/N_{Z-1}, avec l'expression (2.4) pour les états de charge Z et $Z-1$. Il en résulte une expression de la forme

$$\frac{\varepsilon_{ij}^{Z}}{\varepsilon_{mn}^{Z-1}} N_e = f(T_e, N_e) \tag{2.9}$$

où $f(T_e, N_e)$ est une fonction non-linéaire de T_e et N_e.

Ces mesures de la température et la densité électronique permettent de mieux comprendre les conditions du plasma et permettent de situer nos conditions expérimentales dans l'ensemble des connaissances concernant les plasmas produits par laser.

2.3 Conclusion

Au cours des dernières décennies, la LIBS a connu des avancées significatives en matière de précision, de rapidité et de facilité d'utilisation, ainsi que dans la compréhension des mécanismes physiques sous-jacents. Ce chapitre propose un survol succinct des notions essentielles. Bien que la LIBS soit désormais une technique d'analyse élémentaire digne d'attention, capable de fournir des résultats en temps réel et sur site, certains défis persistent, notamment en ce qui concerne la reproductibilité des mesures et les effets de matrice. Toutefois, les progrès continus et les approches innovantes ouvrent la voie à leur résolution.

3 BIBLIOGRAPHIE

[1] D. Hahn and N. Omenetto, “Laser-Induced Breakdown Spectroscopy (LIBS), Part 2: Review of Instrumental and Methodological Approaches to Material Analysis and Applications to Different Fields,” Applied Spectroscopy, vol. 66, 2012.

[2] V. Detalle, Q. Glorieux, R. Bruder, D. L’Hermite, A. Semerok, La spectroscopie d’émission optique sur plasma induit par laser (LIBS). L’actualité chimique, no 312-313, pp. 98 – 104. 2007.

[3] K. Danzer, L. A. Currie, IUPAC. Guideline for calibration in analytical chemistry, Pure Appl. Chem, vol. 70, pp. 993, 1998.

[4] IUPAC, General aspects of trace analytical methods – IV. Recommendations for nomenclature, standard procedures and reporting of experimental data for surface analysis techniques, vol. 51, pp. 2243, 1979.

[5] D. W. Hahn and N. Omenetto, Laser-Induced Breakdown Spectroscopy (LIBS), Part I: Review of Basic Diagnostics and Plasma–Particle Interactions: Still-Challenging Issues Within the Analytical Plasma Community, Appl. Spectrosc, vol. 64, pp. 335A-366A, 2010.

[6] X. L. Mao, W. T. Chan, R. E. Russo, Influence of Sample Surface Condition on Chemical Analysis Using Laser Ablation Inductively Coupled Plasma Atomic Emission Spectroscopy, Appl. Spectrosc, vol. 51, pp. 1047, 1997.

[7] J. A. Aguilera, C. Aragon, Characterization of a laser-induced plasma by spatially resolved spectroscopy of neutral atom and ion emissions: Comparison of local and spatially integrated measurements, Spectrochim. Acta Part B, vol. 59, pp. 1861-1876, 2004.

[8] B. Le Drogoff, J. Margot, F. Vidal, S. Laville, M. Chaker, M Sabsabi, T. W. Johnston and O. Barthelemy. Influence of the laser pulse duration on laser-produced plasma properties, Plasma Sources Sci. Technol. Vol 13. 223–230, 2004.

[9] J.B. Sirven, Détection de métaux lourds dans les sols par spectroscopie d'émission sur plasma induit par laser (LIBS), Thèse de l'Université Bordeaux I, Bordeaux, pp. 159, 2006.

[10] S. Laville, F. Vidal, T. W. Johnston, O. Barthélemy, M. Chaker, B. Le Drogoff, J. Margot and M. Sabsabi, Phys. Rev. E 66, 066415, 2002

CHAPITRE III

3 INSTRUMENTATION ET METHODOLOGIE EXPERIMENTALE

Ce chapitre présente le montage expérimental et la méthodologie utilisés tout au long de ce projet de thèse. Nous y expliquons en détail les différents montages expérimentaux, en mettant en lumière les caractéristiques des systèmes laser et des systèmes de détection employés. Nous présenterons également les procédures expérimentales adoptées pour mener à bien nos analyses, en incluant des détails sur l'échantillonnage. Le montage expérimental utilisé pour effectuer des mesures LIBS au cours de ces travaux de thèse a été conçu pour répondre au mieux à l'objectif fixé, qui est l'analyse quantitative du palladium dans des échantillons miniers.

3.1 Montage expérimental

Un système LIBS de base est composé d'une source laser, d'un spectromètre et d'un système de détection optique (figure 3.1). Les paramètres de travail utilisés dans cette étude sont inspirés de des travaux récents dans notre groupe concernant la mesure de l'or et le Palladium dans le minerai solide [1-4].

3.1.1 Système laser

Un laser pulsé Nd:YAG Surelite I de la compagnie Continuum a été utilisé dans cette étude pour l'ablation et la génération de plasma. Ce laser peut fournir des énergies d'impulsion jusqu'à 600 mJ avec un taux de répétition réglable jusqu'à 20 Hz, une longueur d'onde fondamentale de 1064 nm et une largeur totale à mi-hauteur (FWHM) du profil de temps d'impulsion laser de 8 ns. L'interaction du laser avec l'échantillon étudié étant à l'origine du plasma, tous ces paramètres ont une incidence importante sur le signal LIBS obtenu.

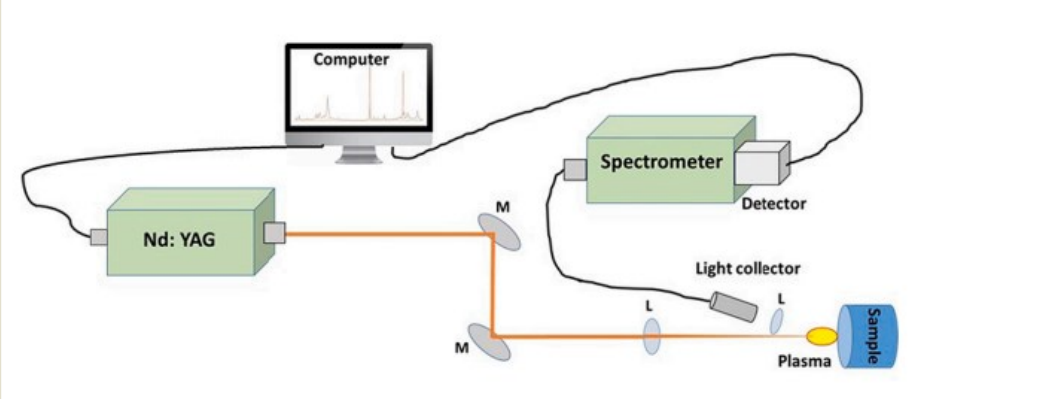

Figure 3-1 Schéma Représentatif du montage LIBS [3].

3.1.2 Systèmes de collection optique

3.1.2.1 Spectromètre McPherson

Nous avons utilisé un spectromètre Czerny-Turner (McPherson modèle 207) avec une distance focale de 0,67 m et une ouverture numérique de F/5,8. Le spectromètre était équipé d'un réseau de 2400 lignes/mm blazé à 300 nm. Ce réseau peut couvrir des longueurs d'onde allant de 180 nm à 650 nm. La dispersion linéaire réciproque correspondante est d'environ 0,53 nm/mm à 267 nm. La rotation de réseau était contrôlée par un moteur pas à pas. La bande passante de ce spectromètre est de 15,5 pm à 267 nm, avec des largeurs de fente d'entrée et de sortie égales de 25 µm.

3.1.3 Système de détection optique

Le détecteur couplé au spectromètre était une caméra à dispositif à couplage de charge intensifié (ICCD) (Istar DH720-25H-05, Andor Technology). La dispersion linéaire réciproque correspondante est d'environ 12 pm/pixel à 267 nm. Le faisceau laser a été focalisé sur la surface plane des échantillons par une lentille de focale de 20 cm pour générer un plasma. Les échantillons ont été montés sur une platine motorisée à trois axes (Newport, UTM 100 mm) pilotée par un contrôleur programmable (Newport, modèle ESP 300). L'émission de plasma était concentrée sur l'extrémité d'entrée circulaire d'un faisceau de fibres optiques composé de vingt-cinq fibres de 100 µm de diamètre. La sortie alignée de ce faisceau a été positionnée devant la fente d'entrée du spectromètre McPherson pour correspondre à la matrice de pixels ICCD.

Les paramètres laser utilisés dans cette thèse sont présentés dans le tableau 3.1. L'énergie laser était de 80 mJ par impulsion tandis que le diamètre du point laser sur la cible était de 750 µm, produisant une fluence d'environ 18 J cm^{-2} et une intensié ou irradiance de 2,3 GW cm^{-2}. Un délai d'acquisition de 4 µs après l'impulsion laser (délai avant de commencer à intégrer le signal) et un temps d'intégration de 10 µs (temps d'intégration du signal) ont été utilisés. Toutes les mesures ont été effectuées dans l'air à pression atmosphérique et à une fréquence de répétition laser de 2 Hz pour s'adapter à la vitesse de la platine de translation qui déplaçait les échantillons dans nos conditions. Cependant, il est possible d'obtenir des vitesses de balayage beaucoup plus élevées (plusieurs kHz) avec certains lasers en déplaçant optiquement le faisceau laser au lieu de l'échantillon. L'instrument LIBS a été calibré en longueur d'onde à l'aide des quatre raies de palladium les plus intenses de notre fenêtre spectrale : 340,45 nm, 342,12 nm, 348,115 nm et 351,69 nm. Comme le montre le tableau 3. 2, ces raies sont proches de raies de fer, un élément

toujours présent dans les géomatériaux que nous avons étudiés. Les intensités relatives des raies de Pd et de Fe fournies par le NIST sont également présentées à titre indicatif et qualitatif [5]. La raie spectrale Pd I 348,115 nm a été utilisée pour les mesures de concentration de palladium en raison de la faiblesse relative de la raie proche Fe I 348,04 nm. En fait, l'interférence entre la raie de Pd et la raie de Fe la plus proche a été considérablement réduite en réduisant l'ouverture de la fente du spectromètre, ce qui a amélioré la résolution spectrale. Plus de détails sont fournis dans le chapitre 4 (article 1).

Tableau 3-1 Principaux paramètres d'analyse LIBS utilisés dans cette étude [3].

Énergie	80 mJ
Diamètre du spot laser	750 µm
Délai d'acquisition	4 µs
Temps d'intégration	10 µs
Distance entre les spots laser	1 mm
Taux de répétition	2Hz
Fente du spectromètre	20 µm

Tableau 3-2 Les raies de palladium dans notre fenêtre spectrale et les raies de fer les plus proches (intensités fournies par NIST)

Pd I	340.45 nm	342.12 nm	348.115 nm	351.69 nm
raies	24000	13000	10000	12000
Fe I	340.43 nm	342.26 nm	348.04 nm	351.65 nm
raies	(31600)	(19500)	(324)	(1410)

3.2 Échantillons

Une collecte d'échantillons miniers contenant des ÉGP a été effectuée dans le cadre de cette thèse, visant à mesurer la concentration de palladium par la technique LIBS. Des échantillons miniers provenant de trois sites distincts ont été rassemblés : des carottes de la mine de Lac des Iles (Ontario, Canada), des roches de la mine de Ni-Cu-ÉGP de Sudbury (Ontario, Canada) et des carottes de la mine Raglan Ni-Cu-ÉGP à Katinniq (Québec, Canada). Chaque site offre des caractéristiques géologiques uniques pour la mesure du palladium. Ces échantillons ont été caractérisés en termes de minéralogie et de géochimie, avant d'être analysés par la LIBS.

Bien que des échantillons des trois mines aient été analysés, nous nous sommes surtout concentrés sur les échantillons provenant de la mine de Lac des Iles car l'opérateur de cette

mine, Impala Canada, était partenaire dans ce projet. Les données relatives aux deux autres mines n'ont pas encore fait l'objet d'une synthèse.

3.3 Mode opératoire

La calibration du montage LIBS se base sur des mesures obtenues sur des étalons ou des MR présentant à la fois une matrice et une lithologie proche de celle des échantillons naturels mesurés. Ces étalons doivent présenter une variété chimique suffisante pour permettre d'établir une calibration de la concentration en palladium. Comme discuté dans le chapitre 2, les courbes de calibration sont construites sur un rapport arithmétique entre les concentrations connues des standards et l'intensité mesurée et normalisée des raies.

***Préparation d'échantillons d'étalonnages**

Les trois types de MR utilisés dans notre étude ont été reçus sous forme de poudre de granulométrie < 74 µm pour les MR LDI-1 et PTC-1b, et < 53 µm pour CDN-ME-1208. Ces matériaux sont constitués d'un mélange homogène de minerai naturel contenant des ÉGP. Le matériau de référence LDI-1 (Geo Labs) est un gabbro à faible teneur en ÉGP provenant du gisement de la mine de Lac des Iles. Les deux autres MR, CDN-ME-1208 (CDN Resource Laboratories Ltd.) et PTC-1b (Canadian Certified Reference Material Project - CCRMP), sont respectivement constitués du minerai de la mine de sulfures de Ni-Cu-ÉGP Raglan et le concentré de la mine de sulfures de Ni-Cu-ÉGP Clarabelle. Ces deux derniers matériaux de référence ont été sélectionnés principalement pour leur teneur plus élevée en fer et en nickel par rapport au MR LDI-1, la forte émissivité de ces éléments ayant un impact direct sur l'étalonnage de l'instrument LIBS [3,4].

Pour calibrer l'instrument LIBS, nous avons enrichi chacun des trois types de MR avec une solution certifiée de chlorure de palladium ($Pd(NH_3)4Cl_2.xH_2O$)) à 1 000 ppm (Sigma Aldrich). Cette solution a été utilisée pour doper les MR avec des teneurs moyennes cibles de la solution de chlorure de palladium de 25, 50, 100, 200 et 500 ppm. La solution saline de chlorure de palladium a été choisie par suite d'essais infructueux avec une solution acide qui provoquait une réaction chimique avec l'échantillon et affectait la composition chimique de la matrice. Les MR non dopés, ayant une concentration en Pd de 0,83, 0,81 et 6,47 ppm pour, respectivement, LDI-1, CDN-ME-1208 et PTC-1b, ont été ajoutés aux 5 échantillons dopés, ce qui fait un total de 18 MR. Pour chaque MR dopé, nous avons mélangé uniformément la solution de palladium avec la poudre. Puis nous avons séché le mélange à une température de 60 °C pendant 24 heures dans une étuve de laboratoire. Nous avons ensuite broyé et homogénéisé le mélange à l'aide d'un

mortier en agate et d'un homogénéisateur (figure 3.2). Enfin, nous avons compressé les échantillons à l'aide d'une presse automatique sous un poids de 30 tonnes, soit une pression de 0,71 GPa exercée sur des pastilles rectangulaires de 3,20 × 4,16 cm de section. Les concentrations de palladium ont ensuite été déterminées sur des sous-échantillons de 30 g chez ALS Canada Ltd, par pyroanalyse et ICP-AES. La photo d'une pastille comprimée est présentée sur la figure 3.3.

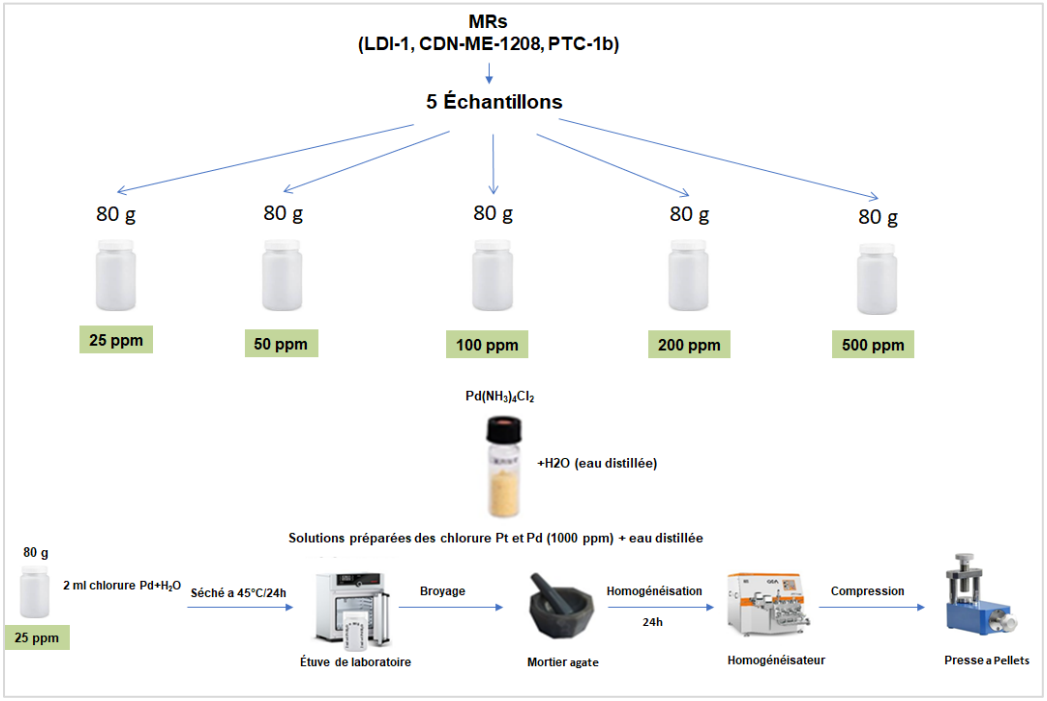

Figure 3-2 **Étapes de préparation des matériaux de référence pour l'étalonnage LIBS**

Figure 3-3 **Exemples de matériaux de référence sous la forme de pastilles comprimées**

Chaque carotte de la mine LDI étudiée dans ce travail est en fait un quart de carotte découpé dans le sens de la longueur. Elles présentent deux faces planes perpendiculaires d'environ 3 cm de large ainsi qu'une face arrondie. Ces quarts de carottes étaient composées de plusieurs morceaux de longueurs inégales. La carotte illustrée à la figure 3.4, qui fait l'objet du chapitre 4 (article 1). était initialement composée de 9 morceaux et mesurait environ 100 cm de long. Afin d'analyser la plus grande surface possible de cette carotte, la face arrondie a été découpée pour

former une surface plane mieux adaptée à la configuration LIBS de notre montage de laboratoire. Pour réaliser cette opération délicate, les pièces les plus longues ont été coupées transversalement. Même si le nombre de fragments était de 15 après l'opération, nous avons regroupé les fragments coupés et conservé la numérotation initiale des pièces.

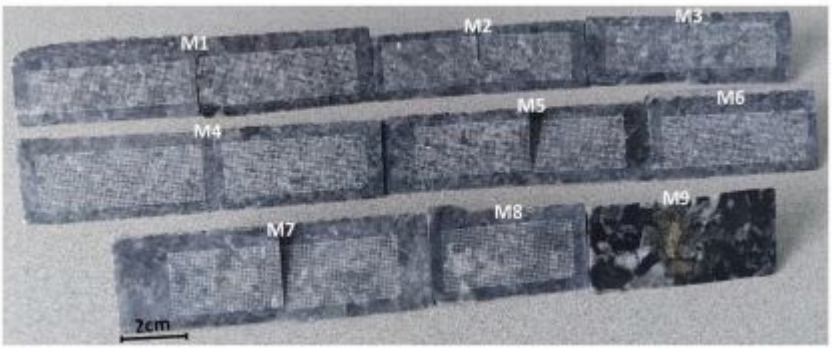

Figure 3-4 Photographie d'une carotte de Lac Des Iles analysée par LIBS

***Protocole de mesure des carottes**

La moitié de la carotte originale de 1 m de long a été analysée par le laboratoire ALS Canada Ltd sous contrat avec la mine LDI. Les concentrations moyennes de palladium de ces demi-carottes ont été comparées avec nos mesures LIBS effectuées sur les portions de carottes dont nous disposions.

Nous avons balayé les faces de chacun des fragments de la carotte avec plusieurs milliers de tirs laser (25 165 au total, pour la carotte de la figure 3.4) espacés de 1 mm selon des matrices rectangulaires. Nous avons ensuite utilisé les spectres LIBS (de 340 nm à 352 nm) de ces réseaux rectangulaires pour construire des cartes basées sur l'analyse en composantes principales (ACP) et la corrélation de Pearson entre les spectres de la carotte et les MR. Ces dernières cartes nous ont permis de démontrer la pertinence de cette corrélation pour construire nos courbes d'étalonnage permettant de déterminer la concentration locale en palladium, et donc la concentration moyenne de chaque face de fragment, ainsi que de l'ensemble du fragment de carotte.

Les phases minérales du minerai de LDI peuvent être caractérisées en première approximation par leur teneur en silicium et en sulfures. Compte tenu de la diversité chimique de nos trois types de MR, la majorité des spectres LIBS collectés à partir de la carotte analysée se sont avérés être similaires à l'un ou l'autre des trois MR. Pour cette raison, nous avons utilisé les trois MR pour calibrer l'instrument LIBS. La courbe de calibration appropriée a été sélectionnée par

comparaison du spectre obtenu pour chaque tir laser avec ceux des MR. C'est le MR dont le spectre était le plus ressemblant (i.e. qui avait le coefficient de corrélation de Pearson le plus élevé) qui a été utilisé pour la calibration.

4 BIBLIOGRAPHIE

[1] K. Rifai, M. Laflamme, M. Constantin, F. Vidal, M. Sabsabi, A. Blouin, P. Bouchard, K. Fytas, M. Castello, B. Nguegang Kamwa, Analysis of gold in rock samples using laser-induced breakdown spectroscopy: matrix and heterogeneity effects, Spectrochim. Acta Part B, vol. 134 pp. 33–41, 2017.

[2] I. Elhamdaoui, K. Rifai, J. Iqbal, N. Mohamed, S. Selmani, J. Fernandes, P. Bouchard, M. Constantin, M. Laflamme, M. Sabsabi, F. Vidal, Measuring the concentration of gold in ore samples by laser-induced breakdown spectroscopy (LIBS) and comparison with the gravimetry/ atomic absorption techniques, Spectrochim. Acta B, vol. 183, pp. 106256, 2021.

[3] S. Selmani, N. Mohamed, I. Elhamdaoui, J. Fernandes, P. Bouchard, M. Constantin, M. Sabsabi, F. Vidal, Laser-induced breakdown spectroscopy analysis of palladium in rock ore. Spectrochimica. Acta Part B, vol. 196, pp. 106523, 2022.

[4] S. Selmani, I. Elhamdaoui, N. Mohamed, J. Fernandes, P. Bouchard, M. Constantin, M. Sabsabi, F. Laser-produced craters in minerals of a palladium ore sample, Applied Physics A, vol. 129, pp. 737, 2023.

[5] NIST Atomic Spectra Database Lines Data. https://physics.nist.gov/PhysRefData/ASD/lines_form.html, 2024. Accédé in september, 2024.

CHAPITRE IV

4 ARTICLE 1 - ANALYSE DU PALLADIUM DANS LE MINERAI DE ROCHE PAR SPECTROSCOPIE DE PLASMA INDUIT PAR LASER (LIBS)

Laser-induced breakdown spectroscopy analysis of palladium in rock ore

Analyse du palladium dans le minerai de roche par spectroscopie de plasma induit par laser (LIBS)

Auteurs :

Samira Selmani [1] , Nessrine Mohamed [2], Ismail Elhamdaoui [1], Jordan Fernandes [1], Paul Bouchard [3], Marc Constantin [2], Mohamad Sabsabi [3] ,François Vidal [1]

[1]Institut National de la Recherche Scientifique, Centre énergie matériaux télécommunications, 1650 Lionel-Boulet blvd, Varennes, QC J3X 1P7, Canada

[2] Departement de Geologie et de Genie Geologique, Universite Laval, 1065 Avenue de la Medecine, Quebec, QC G1V 0A6, Canada

[3] National Research Council of Canada, 75 de Mortagne Blvd., Boucherville, QC J4B 6Y4, Canada

Titre de la revue ou de l'ouvrage :

Article publié le 23 aout 2022 dans la revue Spectrochimica Acta Part B : Atomic Spectroscopy, numéro 196, volume 106523.

https://doi.org/10.1016/j.sab.2022.106523

Contribution des auteurs :

Dans cet article, chaque auteur a apporté une contribution essentielle et complémentaire pour atteindre les objectifs de la recherche.

Samira Selmani, en tant que premier auteur, a effectué l'optimisation du montage expérimental et a été pris les mesures expérimentales sur la carotte. Ensuite elle a analysée et interprété les données, puis a chargée de la rédaction du manuscrit, et ensuite elle a procédé aux corrections et révisions nécessaires pour finaliser l'article (avec une aide particulière de François Vidal).

François Vidal, physicien, a été le directeur principal de ce projet. Il a contribué de manière significative par ses remarques pertinentes et son interprétation pour améliorer l'article. De plus, il a joué un rôle clé dans l'analyse chimiométrique (ACP) est une méthode de visualisation et d'analyse qualitative la concentration de palladium dans les carottes, et a supervisé la correction et la révision de l'article.

Marc Constantin, expert en géologie et en mines à l'université Laval, a joué un rôle important dans l'interprétation de la minéralogie des roches. Ses compétences ont permis de fournir une compréhension approfondie des échantillons miniers étudiés.

Mohamad Sabsabi, reconnu comme un expert en LIBS au CNRC, a apporté son expertise pour optimiser les paramètres expérimentaux et interpréter les résultats obtenus par cette technique. Sa connaissance approfondie de la LIBS a été déterminante pour garantir la précision et la fiabilité des analyses.

Paul Bouchard, expert de la technique LIBS au CNRC Boucherville, a supervisé les aspects techniques et méthodologiques liés à l'utilisation de la LIBS. Il a assuré que toutes les procédures expérimentales respectaient les normes nécessaires et que les équipements étaient utilisés de manière optimale.

Nessrine Mohamad a été responsable de la préparation des matériaux de référence et l'analyse micro-XRF à l'université Laval, ce qui a permis d'obtenir des résultats quantitatifs fiables pour la concentration de palladium dans les échantillons miniers.

Ismail Hamdaoui a apporté une aide précieuse en optimisant le montage expérimental. Ses remarques pertinentes ont permis d'améliorer la configuration et l'efficacité des expérimentations, contribuant ainsi à la fiabilité des données collectées.

Jordan Fernandes a contribué à l'élaboration de la procédure de la calibration au moyen des trois matériaux de référence.

François Vidal, Marc Constantin, et Mohamad Sabsabi ont supervisé le projet dans son ensemble.

Tous les coauteurs ont offert leur soutien pour la rédaction et ont contribué à la révision du manuscrit.

Chacun de ces contributeurs a joué un rôle clé dans le succès de cette recherche, permettant une analyse complète et rigoureuse des échantillons de minerai, et assurant la robustesse et la validité des conclusions tirées.

4.1 Abstract

An emerging geochemical analytical technique, laser-induced breakdown spectroscopy (LIBS), was applied to determine the concentration of palladium (Pd) in a one-meter-long quarter-core ore sample from the Lac des ˆIles palladium mine (Ontario, Canada). This paper demonstrates for the first time the analytical applicability of LIBS as a large-scale, high-performance analyzer for assessing the palladium content of ore. Principal component analysis of LIBS spectra shows three main mineralogical phases: a major silicon-rich and moderately iron-rich (5%) phase, a sulfide-rich phase, and a predominantly silicate phase. To calibrate the LIBS instrument, we used three sets of certified reference materials in the form of compressed powders with a quasi-homogeneous concentration of palladium ranging from around one part per million (ppm) to 500 ppm. Pearson correlation between the unknown spectra and the reference material spectra was used to select the appropriate reference material for quantitative Pd analysis for each single laser shot on the core sample. The palladium concentration of the three sides of nine quarter-core solid fragments was determined by LIBS using the Pd line at 348.115 nm and the average Pd concentration was compared to that obtained from the mine laboratory assay results for the remainder of the core. The LIBS analysis highlighted the significant heterogeneity of the palladium distribution on the surface of the ore and revealed that the sulfide-rich zones are particularly rich in palladium.

4.2 Introduction

As the demand for minerals and metals continues to grow, attention is increasingly focused on what are known as “critical minerals.” More than just rare earth elements, critical minerals encompass several minerals and metals essential to new technologies, including cobalt, copper, precious metals, nickel, uranium, lithium, magnesium and many others. Platinum group elements (PGE) are precious metals and are considered essential minerals by the Mining Association of Canada (MAC) [1]. PGE, which include Pt, Pd, Rh, Ru, Os and Ir, are scarce resources that are in increasing demand in many applications (such as automotive catalysts and fuel cells) due to their unique physical and chemical properties. As a result, PGE mines are very important economic assets for many countries around the world, resulting in billions of dollars of annual production and thousands of direct jobs. The economic importance of precious metal mining as well as the depletion of the resource drive the mining industry of precious metals, such as palladium, to always be on the lookout for new technologies that promote mining activities [2]. Precious metals, including gold and PGE, are commercially mined at concentrations of a few parts per million (ppm) and below. One of the desired advanced technologies would be to measure low average grades (~1 ppm) of precious metals in real time and on site during the various stages of exploration and mine production [3]. However, the analysis of mining samples is currently performed using conventional wet chemistry, fire assay, ICP [4] or atomic absorption [5] techniques. The laboratories where these analyses are performed are not necessarily at mine site which implies waiting times of at least 24 h and leads to production delays at mining or exploration sites, thus increasing operating and production costs. Indeed, the characterization of geological materials using these techniques involve time-consuming, labour intense and demanding preparation methods which require sample dissolution, resulting in loss of spatial information related to their mineralogical identification, elemental composition, and distribution in samples. In addition, these laboratory techniques are not suitable for field conditions due to their off-line nature in terms of the need for special infrastructure, availability of highly qualified personnel, consumables and chemical waste disposal. On-stream X-ray fluorescence (XRF) slurry analyzer has been developed for measuring PGE with precisions in few tens of ppb range [6]. However, in a portable format, XRF cannot quantify precious metals due to its low sensitivity and high limit of detection (LoD) [7,8]. As for infrared spectroscopy, it can determine the mineralogy of rock samples but not their elemental composition [9].

Laser-induced breakdown spectroscopy (LIBS) is a promising technology for performing elemental analysis under desired conditions in real time and on site. LIBS is an optical analysis

technique based on emission spectroscopy that uses a laser beam focused on the sample (solid, liquid or gas) to atomize a small fraction of the surface (<1 mm2) and generate a plasma. The light emitted by the plasma is then collected and analyzed spectrally to determine the chemical composition of the sample. Using reference materials (RMs), a relationship is established between the intensities of the spectral lines and the content of the element of interest [10–13]. LIBS calibration is used to determine the concentration of this element in samples with a similar chemical composition to that of the RMs. The main potential advantages of LIBS for the mining industry over conventional analytical techniques is its ability to rapidly analyze samples on site with minimal or no sample preparation, regardless of the nature of the sample [14]. LIBS has already found applications in several fields of industry [15].

Much work has been devoted to the application of LIBS to mineralogy [12,16]. This work involves qualitative detection of elements for geochemical fingerprinting, sample classification and discrimination, as well as quantitative geochemical analysis, rock characterization through particle size analysis, and in situ geochemical imaging. Despite the growth in LIBS development, it is only recently that the concentration of precious metals has been measured by LIBS, the work on this subject concerning mainly the quantitative measurement of gold developed in our group [10]. Nearly at the same time, Diaz et al. [17] developed an analytical protocol for the quantification of Au and Ag in ore samples naturally containing Au and Ag and in pressed pastilles of surrogate samples spiked with standard Au and Ag solutions. Subsequently, they examined the effects of wavelength and laser irradiation on gold quantification [18] and used principal component analysis (PCA) to identify the spectra containing the gold signal in the pressed gold ore pellets [19]. Harmon et al. [20] and Pochon et al. [21] used a portable LIBS instrument to determine the provenance of alluvial gold deposits using relative Ag and Au content. Rifai et al. [22] presented the new capabilities of LIBS for rapid and high-resolution multi-element mapping of geological samples, as well as for mineral phase identification. Gervais et al. [23] used their LIBS instrument to perform 3D tomography by successive layer ablation in a gold ore sample. Rifai et al. [10] and Elhamdaoui et al. [11] used pressed powder RMs with quasi-homogeneous gold concentrations between 0 and 1000 ppm to calibrate the LIBS instrument. The normalized calibration model was characterized by two separate branches, one for Si-rich samples and one for Fe-rich samples. The resulting LIBS calibration model was used to analyze uncompressed powders as well as ore samples. Elhamdaoui et al. [11] also evaluated a strategy to minimize the number of laser shots for the quantitative analysis of gold in solid mineral. For PGE, Snyder et al. [24] applied LIBS to aqueous suspensions of palladium particles in reformate water of palladium-containing proton exchange membrane fuel cells. They established a calibration curve and estimated the size of

the detected particles. Al Shuaili et al. [25] demonstrated that microwave-assisted LIBS (MW-LIBS) under ambient conditions improves the LoD of palladium in solid samples by a factor of 8. The mineralogy of PGE ore was also characterized by LIBS in the work of Rifai et al. [26, 27] and Mohamed et al. [28] using a database established by TIMA-X and electron probe microanalyses (EPMA). Elhamdaoui et al. [29] applied the LIBS assisted with Laser-Induced Fluorescence (LIBS-LIF) technique to measure trace amounts of palladium in solid ore samples at sub-ppm level using a single laser shot, which is not possible with the conventional LIBS technique. It is also worth mentioning that recent developments in engineering and miniaturization [30,31] have made it possible to develop a prototype portable LIBS instrument for measuring gold concentration in ore. In principle, the same technology could be adapted to quantitatively measure PGE in ore.

This paper deals with the use of LIBS to analyze the palladium content and mineralogical phases in a drill core from the Lac des ˆIles (LDI) palladium mine located 85 km north of Thunder Bay, Ontario, Canada. The Archean intrusive complex at LDI is composed of mafic to ultramafic intrusions and is known to host significant PGE deposits. The proven and probable mineral reserve of the LDI property is 40.88 Mt. at 2.31 g/t Pd, 0.21 g/t Pt, 0.174 g/t Au, 0.07% Ni, and 0.06% Cu [32]. The LDI palladium deposits occur in a small, roughly concentrically zoned intrusion [33] (Fig. 4. 1) and are primarily characterized by a gabbroic to gabbronoritic intrusion [34]. The gabbronorite cores used in this study were taken from the B3 Zone deposit. LDI gabbronorites are typically composed of Mg-Fe pyroxene (25–75%) or plagioclase (35–70%) [35]. Barnes and Gomwe suggest that collection of platinum group minerals (PGM) by sulfide liquid and enrichment of palladium by the fluids played a role in ore formation. In the LDI mine, the positive correlation between S, PGE, Au, Cu, and Ni suggests that the PGE-controlling phases are base metal sulfides [36]. In [28], we characterized a pyroxenite sample as well as a gabbronorite sample from the LDI mine, of the same type as the core studied in the present study, using μ-XRF, electron probe microanalysis (EPMA), polarized light microscopy, and a LIBS database [26, 27]. Gabbronorite samples were found to be composed primarily of hornblende (~50%), plagioclase feldspar (~25%), actinolite (~15%), sulfides, mainly pyrrhotite, pentlandite, chalcopyrite, and pyrite (~5%), and other minor minerals (~5%). The mineral phases are intermingled with domains ranging from ≤10 μm to ~10 mm.

In this paper, we primarily explore three aspects of LIBS analysis of a LDI drill core: (1) quantitative assessment of average palladium concentration, (2) spatial distribution of palladium in the ore, and (3) qualitative analysis of ore phases using principal component analysis (PCA). For the

quantitative assessment of average palladium concentration, we used three calibration curves based on three RMs consisting of compressed palladium-doped powders at different concentrations. Pearson correlation mapping between the reference spectra and the rock sample spectra was performed to assess the suitability of the RMs used.

Figure 4-1 Simplified geology of the Lac des ˆIles igneous complex [32].

4.3 Methods and experimental setup

4.3.1 Experimental setup

The experimental setup for LIBS analysis (Figure 4. 2) and the working parameters used in this study are inspired by our previous work [10, 11]. A Nd:YAG laser (Continuum Surelite I) was used for ablation and plasma generation. This laser can deliver pulse energies up to 600 mJ with adjustable repetition rate up to 20 Hz, a fundamental wavelength of 1064 nm, and a full width at half maximum (FWHM) of the laser pulse time profile of 8 ns. The spectrometer was a Czerny-Turner (McPherson model 207) with a focal length of about 0.67 m and a numerical aperture of F/5.8, covering wavelengths from 180 nm to 650 nm by using a 2400 grooves/mm UV enhanced grating. The detector coupled to the spectrometer was an intensified charge-coupled device (ICCD) camera (Istar DH720-25H-05, Andor Technology). The corresponding reciprocal linear dispersion is about 12 pm/pixel at 267 nm. The laser beam was focused on the flat surface of the samples by a 20 cm focal length lens to generate a plasma. The samples were mounted on a

three-axis motorized stage (Newport, UTM 100 mm) driven by a programmable controller (Newport, model ESP 300). The plasma emission was focused on the circular input end of a fiber optic bundle consisting of twenty-five 100 µm diameter fibers. The aligned output of this bundle was positioned in front of the McPherson spectrometer input slit to match the ICCD matrix of pixels.

The laser parameters used in this study are displayed in Table 4.1. The laser energy was 80 mJ per pulse while the laser spot diameter on the target was 750 µm, producing a fluence of around 18 J cm^{-2} or irradiance of 2.3 GW cm^{-2}. A delay time of 4 µs after the laser pulse (delay before starting to integrate the signal) and a gate width of 10 µs (signal integration time) were used. These two values were chosen to achieve a near-optimal signal-to-noise ratio for our setup. All measurements were performed in air at atmospheric pressure and at a laser repetition rate of 2 Hz to accommodate the speed of the translation stage that moved the samples in our conditions. However, much higher scanning speeds (several kHz) can be achieved with some lasers by displacing optically the laser beam instead of the sample. The LIBS instrument was calibrated in wavelength using the four most intense palladium lines in our spectral window: 340.45 nm, 342.12 nm, 348.115 nm, and 351.69 nm. As shown in Table 4.2, all three lines are close to iron lines. The relative intensities of the Pd and Fe lines provided by NIST are also given as a qualitative indication [37]. The Pd I 348.115 nm spectral line was used for the palladium concentration measurements due to the relative weakness of the Fe I 348.04 nm near line. In fact, the interference has been significantly reduced by using a small slit of the spectrometer. More details are provided in Section 4.4.2.

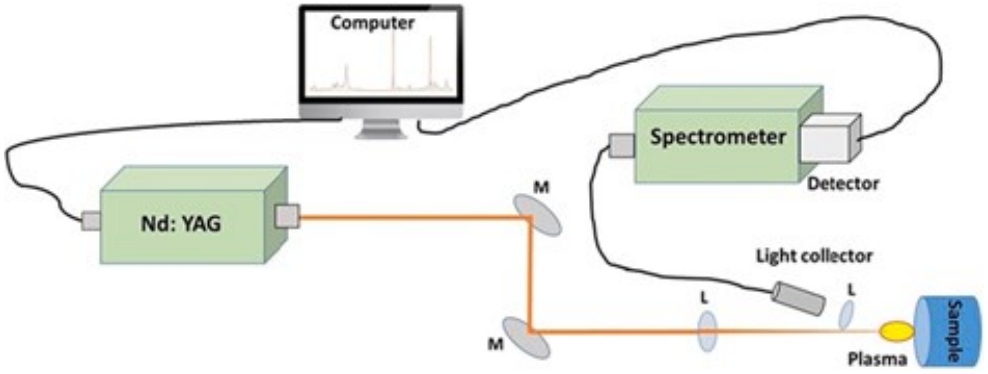

Figure 4-2 Schematic representation of the experimental LIBS setup.

Tableau 4-1 Main LIBS analysis parameters used for the calibration curves and core samples.

Laser energy	80 mJ
Laser spot diameter	750 µm
Integration delay	4 µs
Gate width	10 µs
Distance between laser spots	1 mm
Repetition rate	2 Hz
Spectrometer slit	20 µm

Tableau 4-2 Palladium lines in our spectral window and their closest iron lines. Line relative intensities given by NIST are provided in parentheses.

Pd I lines	340.45 nm (24000)	342.12 nm (13000)	348.115 nm (10000)	351.69 nm (12000)
Fe I lines	340.43 nm (31600)	342.26 nm (19500)	348.04 nm (324)	351.65 nm (1410)

4.3.2 Analyzed core and reference samples

The core sample studied in this work is a quarter core cut lengthwise with two perpendicular flat faces about 3 cm wide and a rounded face. The core was originally composed of 9 pieces and was approximately 100 cm long (Figure 4.3). In order to analyze the largest possible surface area of the core, the rounded face was cut away to form a flat surface better suited for our laboratory LIBS setup. For this purpose, the longest pieces had to be cut transversely. Although the number of fragments was 15 after the operation, we grouped the cut fragments and kept the initial numbering of the pieces. Each of the three faces was scanned by the laser (spot size of 750 µm) with a step distance of 1 mm between the centers of the laser spots.

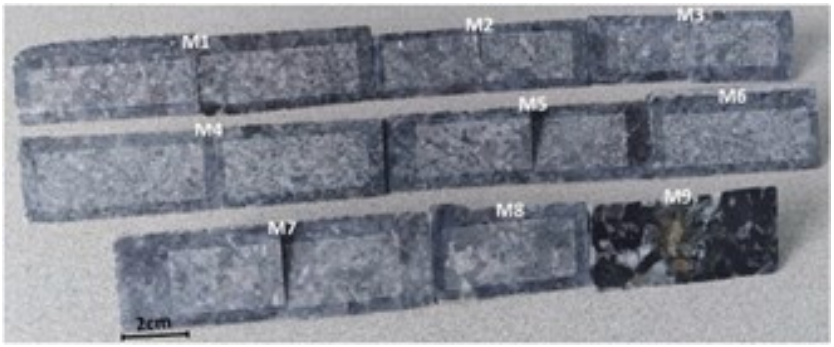

Figure 4-3 Photograph of the analyzed LDI quarter core. The laser scanned areas appear as lighter dotted rectangular areas. The side (side 3) of the M fragment shown in the photo looks different because it was freshly cut and not scanned with the laser.

Half of the original 1 m long core was analyzed according to a rigorous protocol for each chemical element by an ALS laboratory under contract to the LDI mine. Up to 250 g of the ground half-core was first reduced to a grain size of <75 µm. In particular, for Pd, Pt, and Au, 30–50 g of the powder was decomposed by fire assay, then digested in acidic solutions before being analyzed by ICP-AES. Some of the results of this quantitative analysis are presented in Table 4.3.

The LDI quarter-core studied here has different phases that can be characterized in first approximation by their silicon and sulfide content. For this reason, we used three RMs to calibrate the LIBS instrument. The chemical composition of these RMs before doping with different concentrations of palladium is presented in Table 4.4. These materials are in the form of powder with grain size of <74 µm for LDI-1 and PTC-1b, and <53 µm for CDN-ME-1208. These materials consist of a homogeneous mixture of natural ore containing PGE. The LDI-1 RM (Geo Labs) is a low-grade PGE-bearing gabbro collected from the LDI deposit. There- fore, the majority of LIBS spectra collected from the analyzed core is similar to those from this RM, as can be seen by comparing Tables 4.3 and 4.4. The other two RMs, CDN-ME-1208 (CDN Resource Laboratories Ltd.) and PTC-1b (Canadian Certified Reference Material Project - CCRMP), are respectively ore from the Raglan Ni-Cu-(PGE) sulfide mine (Katinniq, Quebec, Canada) and the Ni-Cu sulfide concentrate with noble metals from the Clarabelle mill (Sudbury, Ontario, Canada). These last two RMs were selected mainly for their high iron content, whose high emissivity has a direct impact on the calibration of the LIBS instrument. [10, 11].

To calibrate the LIBS instrument we spiked each of the 3 kinds RMs with palladium chloride solutions targeting concentrations of 25, 50, 100, 200 and 500 ppm. We added the undoped materials (Table 4.4) to this set to establish the calibration curves. This makes a total of 18 aliquots of RMs. As will be discussed later in this study (section 3.5), relatively high concentrations of palladium are found locally due to the discrete nature of the palladium distribution in ore samples, which can reach several thousand ppm in the laser spot area. For each doped RM, we uniformly mixed the palladium solution with the powder. We then dried the mixture at a temperature of 60 ◦C for 24 h. Finally, we com- pressed the samples using an automatic press under a weight of 30 tons, i.e. a pressure of 0.71 Gpa exerted on pastilles of 3.20 × 4.16 cm.

Tableau 4-3 Partial chemical composition of the Lac des ˆIles 1 m long half-core used in this study.

Identification	Rock type	Composition									
		Pt (ppm)	Pd (ppm)	Si (%)	Ca (%)	Fe (%)	S (%)	Cu (%)	Ni (%)	Al (%)	Mg (%)
18-805-X097924	Gabbronorite	0.568	4.93	24.2	6.6	4.7	0.35	0.14	0.31	7.7	7.8

4.4 Results and discussion

We scanned the 3 faces of each of the 9 core fragments (except face 3 of fragment M9 which was put aside for another use) following rectangular arrays for a total of 25,165 laser shots on the core. LIBS spectra cover the range from 340 nm to 352 nm. We then used the LIBS spectra of these rectangular arrays to construct maps based on principal component analysis (PCA) and the Pearson correlation between the core and RM spectra. The latter maps allowed us to use the appropriate calibration curve for each laser shot to determine the local palladium concentration, and from there, the average concentration of each frag- ment face, as well as the entire core.

4.4.1 Principal component analysis of a fragment of the core

To perform PCA of the LIBS spectra collected from the core, we first normalized each LIBS spectrum using the standard normal variate (SNV) method.

$$I_i^{SNV} = \frac{1}{\sigma}(I_i - \langle I \rangle) \tag{4.1}$$

to bring them on an equal footing. Here Ii is the intensity of the ith wavelength of the spectrum, with i ranging from 1 to 1024, σ is the standard deviation and 〈I〉 is the average value of the whole spectrum. All spectra thus have a mean value of 0 and a standard deviation of 1.

Fig. 4.4a shows a photograph of face 1 of the M9 fragment (hereafter called M9-F1) which will be discussed as a representative case because it clearly shows the 3 main mineral phases identified on the core. Fig.4.4b shows principal component 2 (PC2) versus principal component 1 (PC1) for the 980 spectra collected on M9-F1 as well as for the 18 aliquots of RMs. Each dot represents a spectrum. Since PC1 and PC2 represent 58% and 18%, respectively, of the total variance, they allow a useful classification of the main mineral phases of the core sample. PC3 represents only 4% of the total variance. One can distinguish in Fig.4.4b three main regions delimited approximately by dashed lines at PC1 = -6 and + 6. Nearly 2/3 of the dots are in the tight cluster between the two dashed lines. Consistent with the LDI origin of the core, these spectra are similar to those of the LDI-1 RM that was also collected at this location. The remaining points are almost evenly distributed in the tight group lying in PC1 > 6 and in the scattered group in PC1 < -6 that includes the spectra of the sulfide-rich RMs CND-ME-1208 and PTC-1b. With the SNV normalization, these two sulfide-rich materials are located close together in the PC2 vs PC1 diagram, even though their overall chemical composition is different (Table 4.4), due to their high iron content whose intense lines mask those of other elements.

Tableau 4-4 **Partial elemental composition of the 3 reference materials used in this study before doping at 25, 50, 100, 200 and 500 ppm palladium.**

Identification	Rock type	Composition									
		Pt (ppm)	Pd (ppm)	Si (%)	Ca (%)	Fe (%)	S (%)	Cu (%)	Ni (%)	Al (%)	Mg (%)
LDI-1	Silicate-rich	0.0982	0.834	22.79	7.26	5.38	0.12	0.0413	0.0656	9.19	6.56
CND-ME-1208	Sulfide-rich	0.807	3.42	16.07	3.72	18.45	8.98	1.635	4.77	5.72	4.40
PTC-1b	Sulfide-rich	6.47	9.46	2.468	0.571	36.78	29.95	7.97	11.29	0.75	0.44

Fig. 4.4c represents the reconstruction of the photograph of the scanned area using the PC1 values. There is apparent correspondence between Fig. 4.4c and the area delimited by the red dashed quadrangle in Fig. 4.4a. Our analyses of the LDI ore [28] allowed us to identify most of the mineralogical phases present in the sample studied here. The dark areas in Fig. 4.4c (PC1 < -6) correspond in particular to the yellowish areas in Fig. 4.4a (near the red triangle, for example) that are identified as composed mostly of chalcopyrite (CuFeS2), pentlandite ($(Ni, Fe)_9S_8$), pyrrhotite ($Fe_{1-x}S$ with $0 < x < 0.17$) and pyrite (FeS_2), which are sulfide minerals with a yellowish metallic appearance. The gray areas ($-6 \leq PC1 \leq 6$) correspond mainly to an amphibole identified as mainly hornblende $((Na, K)_{0.227}(Ca,Na,Fe,Mn)_2(Mg,Fe^{2+},Fe^{3+},Al,Ti,Cr,Ni,Co)_5(Si,Al,P)_8O_{22}((OH),F,Cl)_2)$. The white areas in Fig. 4.4c (PC1 > 6) correspond to the whitish areas in Fig. 4.4a that correspond to a plagioclase feldspar identified as predominantly bytownite ($(Ca,Na)(Si,Al)_4O_8$). No RM was prepared for this phase since PGE are not expected at all in feldspar. Indeed, no palladium lines above the noise level were detected in these areas.

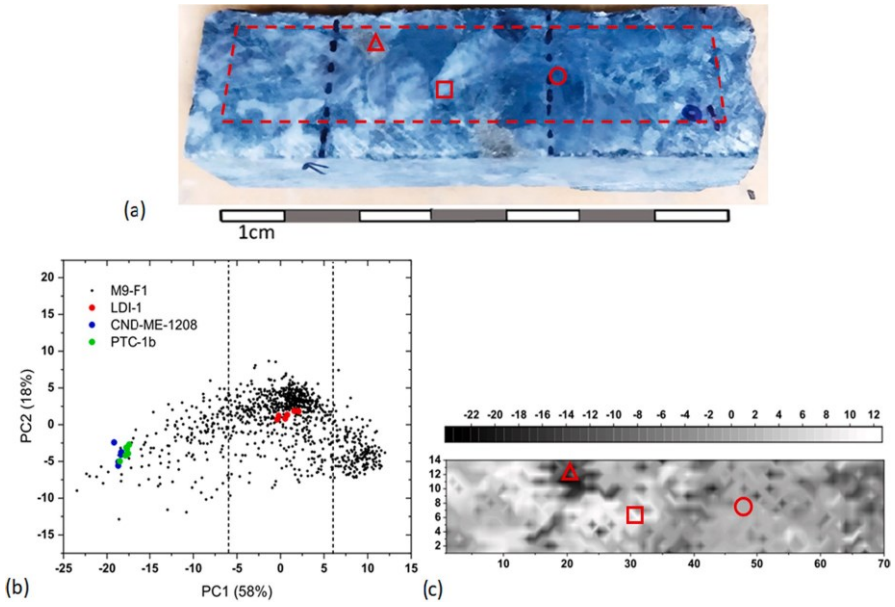

Figure 4-4 **(a) Photograph of M9-F1 with enhanced contrast before laser scanning. The red dashed quadrangle is the area where 70 × 14 = 980 spectra were collected. (b) Principal components PC2 vs PC1 diagram for the 980 spectra taken on M9-F1 as well as for the 18 aliquots of the reference materials. (c) Grayscale map of PC1 values with smoothing to be compared to the area included in the red dashed quadrangle in (a). The scales indicate the coordinates of the laser shots (equivalent to lengths in mm). The red circle, triangle and square in (a) and (c) correspond to the amphibole (LDI-1 type), sulfide phase (CDN-Me-1208 and PTC-1b type), and plagioclase feldspar, respectively. (For interpretation of the references to colour in this figure legend, the reader is referred to the web version of this article.).**

4.4.1 Calibration curves

Fig.4.5a shows the raw LIBS spectra of the three RMs doped with 500 ppm palladium and shows the 348.115 nm Pd I line used in this study. Each spectrum in Fig.4.5a, represents the average of 100 spectra taken at different locations on the RMs. It can be seen that the iron lines dominate the spectra. As mentioned above, the weak Fe 348.04 nm line is the closest line to the Pd 348.115 nm line (Fig.4.5b). Using the high-resolution spectrometer in our facility with a slit aperture of 20 µm, which leads to a linear dispersion of 12 pm per 25 µm pixel, the two lines are separated by 6 pixels. Since we use the net intensity and not the integral of the lines for the calibration curves, the Fe 348.04 nm line does not affect the peak of the 348.115 nm Pd line, as we verified using simple Lorentz fits, even for the sulfide rich RMs.

The calibration curves for the RMs were established by using the normalized net intensity of the Pd 348.115 nm line

$$I_{Pd,net} = \frac{I_{Pd,raw}}{B} - 1 \qquad \textbf{(4.2)}$$

where IPd, raw is the raw intensity of the Pd 348.115 nm line for each of the 6 concentrations of the 3 RMs. The raw intensity was normalized by B which is the average of the intensities between 342.95 and 343.05 nm that is free of lines (background), as shown in Fig.4.5c. Normalization of the spectra was performed to compensate for variations of the palladium signal from the laser-induced plasmas due to variations in the surface properties of the samples, especially when moving from RMs to the core. This region was also used to evaluate the noise to determine the LoD.

All experimental conditions were the same for the 18 aliquots of RMs. As in Fig.4.5, each measurement represents the average of 100 laser shots. The error on the net intensity was estimated by the standard deviation of 3 sets of 100 laser shots on each RM. As shown in Figs.4.6, 3 distinct calibration curves are obtained. The normalized net intensity of the palladium line at a given concentration decreases from LDI-1 to CDN-ME-1208 and PTC-1b due to the strong emission of the iron lines which increase the intensity of the background B. All calibration curves

show good linearity up to about 200 ppm and then increase faster as a function of IPd, net. The reason for the deviation from linearity at high concentration, which is particularly evident for the PTC-1b RM, is likely due to self-absorption even though the Pd line at 348.115 nm is not resonant (lower energy level = 1.25 eV [37]). For TPC-1b, the slope of the curve of growth (COG) is consistent with the theoretical expectations of m = 1 at low concentrations and m = ½ at higher concentrations [38] but the slope is between 0.4 and 0.7 at the highest concentrations (last 3 points), considering the error bars. Using the method of Hao et al. [39], we found that the self-absorption coefficient (SA) is 0.46 at 500 ppm. For the LDI-1 and CDN-ME-1208 RMs, SA is close to 1. We note that, unlike the SNV normalization used for PCA, normalization to background reveals significant differences between CDN-ME-1208 and PTC-1b RMs. SNV normalization is convenient for comparing spectra but it cannot be used to establish calibration curves.

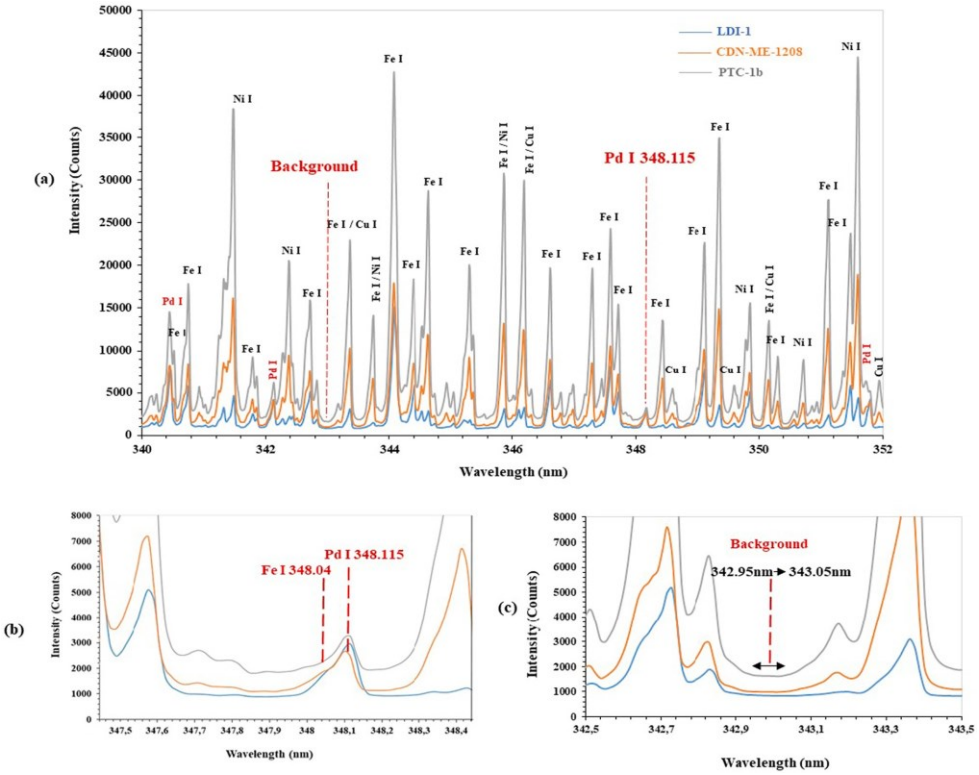

Figure 4-5 **(a) Raw LIBS spectra covering the 340–352 nm window for the three reference materials LDI-1 (blue), CDN-ME-1208 (orange) and PTC-1b (gray) doped with 500 ppm palladium. The strongest lines are identified. (b) Close-up view around the palladium line at 348.115 nm used for concentration measurements. (c) The line- free spectrum area between 342.95 and 343.05 nm used to calculate the normalized net intensity and the noise level. (For interpretation of the references to colour in this figure legend, the reader is referred to the web version of this article.)**

On the basis of the commonly used criterion that the minimum detectable intensity of the palladium line is three times the level of the background noise [40], the LoD of palladium for 100 shots is estimated to be around 0.5 ppm for the three RMs, i.e. around 5 ppm for a single laser shot.

These calibration curves were used to estimate the palladium con- centration for each laser shot on the core. To do this, the normalized net intensity of the 348.115 nm Pd line of the core spectra was obtained from Eq. (4.2), and then the appropriate calibration curve was used as a function of the local phase, as explained in Section 4.4.4. Fig. 4.7 shows the normalized average spectrum collected on M9-F1 in comparison with the normalized spectrum of LDI-1. Consistent with the PCA analysis, the two average spectra show many similarities. More detailed comparisons between the core and RM spectra are presented in Section 4.4.4.

4.4.2 Average palladium concentration of the drill core

The palladium concentration was determined for each laser shot. To do so we proceeded as follows:

Normalize a given spectrum taken on the rock Srock and the average spectra taken on the 3 types of undoped RMs Sref,i with i = 1, 2, 3, according to the SNV method.

Calculate the Pearson correlation between the SNV normalized spectra Srock and Sref,i

$$\rho_{S_{rock},S_{ref,i}} = cov(S_{rock}, S_{ref,i}) \tag{4.3}$$

for i = 1, 2, 3.

Identify the RM i giving the maximum value ρmax =

Max(ρSrock ,Sref ,i for i = 1, 2, 3).

Use the calibration curve corresponding to the RM identified in 3) or assign a concentration of 0 when ρmax < ρc where ρc is a chosen threshold value.

In the following, the value ρc = 0.92 was selected to be consistent with the PCA of M9-F1 (Fig. 4.4b) and with the Pearson correlation analysis shown in Fig.4.8. This figure shows the Pearson correlation maps (or similarity maps) of the scanned surface indicated in Fig.4.4a. In principle, Pearson correlation ranges between -1 and +1 but we have not found any value smaller than 0.5 for all the spectra collected on the core. Red colour means a correlation close to +1, i.e. a high similarity

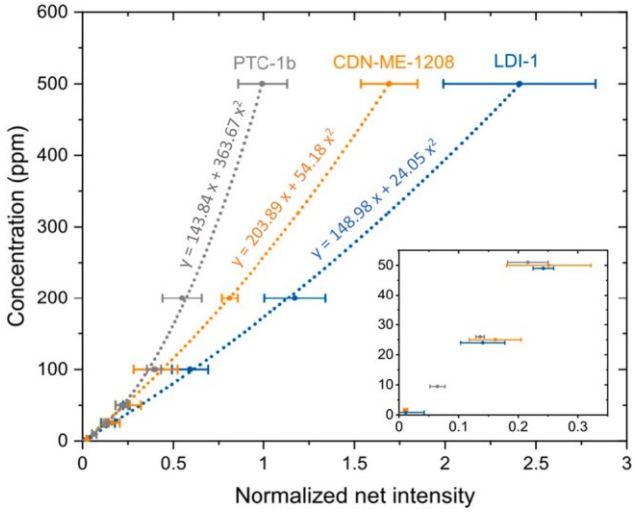

Figure 4-6 **Calibration curves using the Pd 348.115 nm line for the three types of RMs used in this work: LDI-1, CDN-ME-1208, and PTC-1b. The root mean square errors (RMSE) are 5.9, 5.4 and 6.7 ppm, respectively. The coefficient of determination R2 is >0.998 for the three quadratic fits. The inset shows the data at low concentration.**

between the spectra, while a lower similarity is represented by cooler colors. Comparison of Fig. 4.8a, b, and c shows that the spectra of M9-F1 are mostly similar to that of the LDI-1 RM. Several areas of lower correlation in Fig. 4.8a (yellow and green areas) correspond to high correlation with the CDN-ME-1208 or PTC-1b reference spectra (Fig, 8b and 8c). The correlation maps of CDN-ME-1208 and PTC-1b are very similar as already observed in the PCA (Fig. 4.4b). However, for some reason, the spectrum of PTC-1b has overall more similarities with the spectra of M9- F1 than that of CDN-ME-1208 since it shows more reddish and less blueish areas. The maximum correlation at each point for the 3 RMs is shown in Fig. 4.8d. The presence of yellow areas on this map indicates that the 3 RMs are not complementary. This is consistent with the PCA analysis in Fig.4.4, which shows that the white areas (Fig. 4.4a or c) composed of plagioclase feldspar do not match well any of our RMs. We observe that the yellow patterns in Fig. 4.8d correspond approximately to the white patterns in Fig. 4.4a and c. It can be seen that the criterion ρmax < ρc = 0.92 (yellowish spots in Fig. 4.8d) mentioned above denotes sufficient dissimilarity between the core and RM spectra, which means that none of the calibration curves are used in this case and the Pd concentration is set at 0. It should be noted that PCA could be used in some way to select the appropriate calibration curve, but the Pearson correlation method is preferred because it quantifies the similarity between spectra more accurately and is much faster from a computational perspective.

Fig.4.8e compares the spectra of M9-F1 with those of undoped RMs at the 3 points denoted A, B, and C at the positions indicated by × in Fig.4.8d. These positions correspond approximately to

the circle, triangle, and square symbols, respectively, in Fig.4.4a and c. The spectrum at point A shows very high similarity to the spectrum of LDI-1, with the corresponding point in the map in Fig.4.8a indicating high correlation. The spectrum at point B shows a high correlation with the spectrum of CDN- ME-1208. This point lies within the area with metallic reflections (chalcopyrite, pentlandite, pyrrhotite, and pyrite) in Fig.4.4a. The spectrum at point C does not match well with any of our RMs but it matches better with that of LDI-1. However, it can be seen in Fig.4.8e that the spectrum at point C is rather noisy and does not match well with the spectrum of LDI-1 by comparison with point A. The phase at point C, identified as plagioclase feldspar, includes Fe micro-inclusions, as already noticed in [28].

We used this procedure to evaluate the average palladium concentration of the 3 faces of the 9 core fragments from the laser shot spectra (with the exception of face 3 of M9). The results are presented in Table 4.5. With the 26 rectangular arrays of laser shots on the 26 faces, comprising between 525 and 1260 shots depending on the size of the surface, a weighted average (based on the number of laser shots on each face) was performed to determine the average palladium concentration of each fragment. In doing so, we assumed that the negative concentrations due to noise statistically offset the positive noise contributions around the zero concentration. The weighted standard deviation of the 3 faces of each fragment was also determined. There is significant inhomogeneity in the distribution of palladium as the average concentration of Pd in the fragment faces ranges from 0.1 to 24.3 ppm. The weighted standard

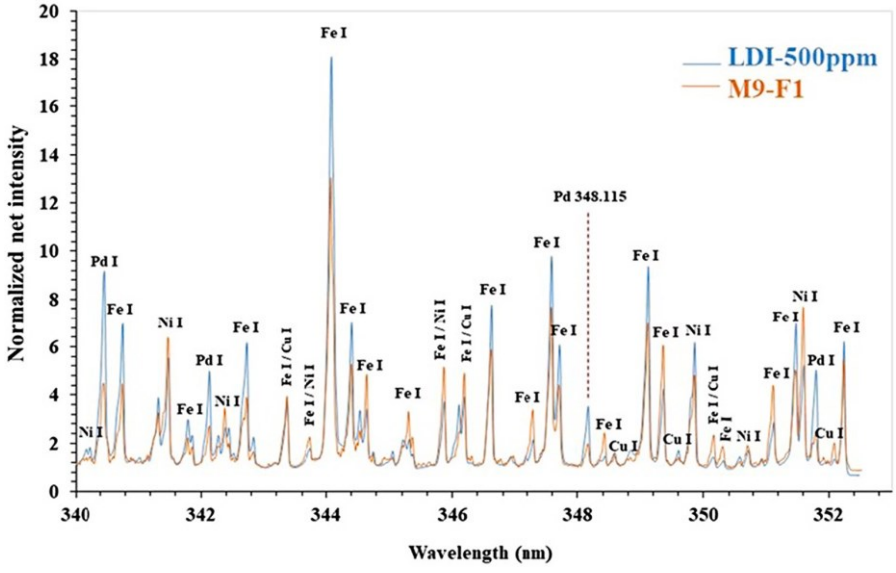

Figure 4-7 **Average spectrum of the 980 B-normalized spectra collected on M9-F1 compared to the average of 100 B-normalized spectra collected on the LDI-1 RM spiked at 500 ppm.**

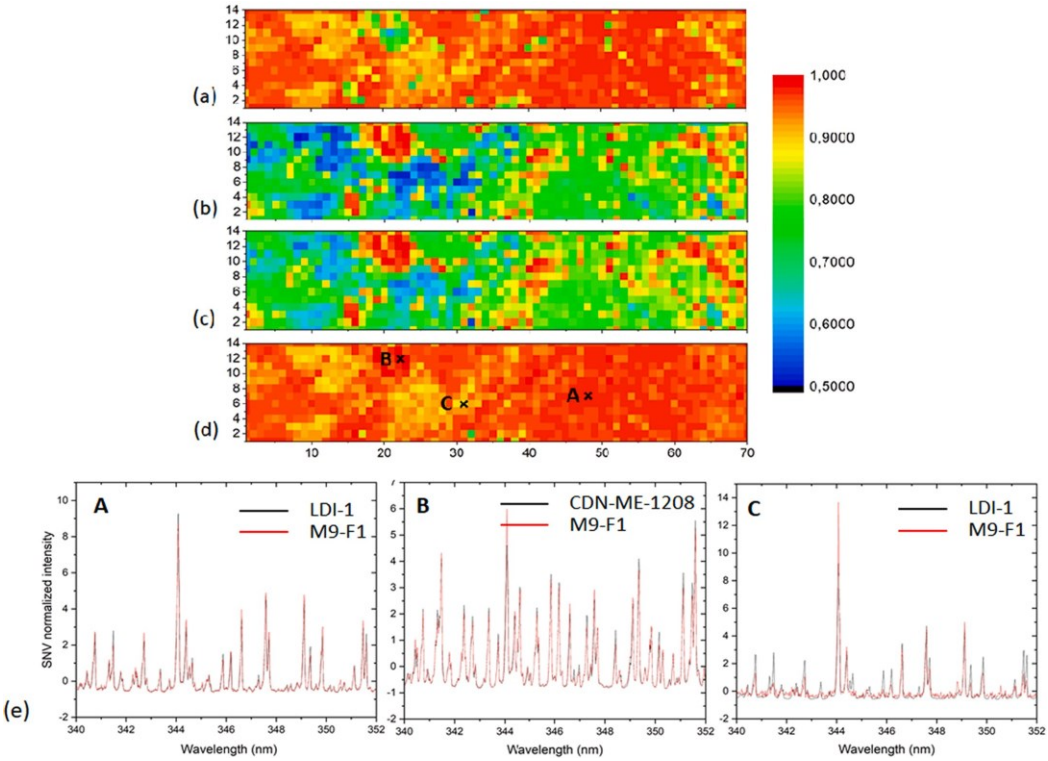

Figure 4-8 **Similarity maps between the SNV-normalized spectra taken on M9-F1 and those taken on the undoped reference materials (a) LDI-1, (b) CDN-ME-1208 and (c) PTC-1b with the lowest Pd concentration. The map (d) displays the maximum values of maps (a), (b) and (c) at each location. (e) SNV-normalized spectra at positions denoted by an × in (d). Black: reference spectra; red: M9-F1 spectra. (For interpretation of the references to colour in this figure legend, the reader is referred to the web version of this article.)**

Tableau 4-5 **Columns 2, 3, and 4: Average Pd concentrations for the 3 faces of the 9 drill core fragments. Column 5: Weighted average concentration. Column 6: Weighted standard deviation (WSD) of the 3 faces. Last row: average Pd concentration calculated using the 25,165 spectra taken from the entire drill core and WSD of the average concentrations of the 26 faces.**

Fragment	Face 1 (ppm)	Face 2 (ppm)	Face 3 (ppm)	Weighted average (ppm)	WSD (ppm)
M1	10.1	1.6	4.9	6.0	4.6
M2	24.3	8.8	2.9	12.8	11.9
M3	0.3	2.7	2.3	1.7	1.3
M4	2.1	0.1	4.4	2.1	2.2
M5	2.7	2.4	0.6	2.0	1.1
M6	1.4	4.5	4.3	3.3	1.8
M7	6.9	2.0	7.3	4.9	3.1
M8	2.8	3.6	3.3	3.3	0.4
M9	23.8	7.2	-	15.5	11.8
All fragments				5.2	6.2

deviation (WSD) generally represents a substantial fraction of the average value of the 3 faces. Table 4.5 also shows the average Pd con- centration obtained from the 25,165 laser shots taken on the 26 faces and the corresponding WSD. The average LIBS Pd concentration of 5.2 ppm must be compared to the average concentration of 4.93 ppm measured for the half of the original core by the mine laboratory using conventional methods. This result is quite satisfactory considering the inhomogeneous distribution of palladium throughout the core and the fact that the LIBS analysis is performed on the surface of the core, which involves analysis of a very small volume of material by laser ablation. It should be emphasized that the WSD of 6.2 ppm should be understood as a measure of the dispersion of the average Pd concentration on the 26 faces, not as an error on the average value. Note that the average concentration depends weakly on the chosen value of ρc provided it is around 0.9, as can be understood from Fig. 4.8d, although it influences the proportion of spectra not corresponding to any of the RMs.

4.4.3 Palladium distribution in the core

Table 4.6 presents some statistics on the proportion of spectra associated with undoped RMs with a Pearson correlation greater than ρc =0.92. Around 16% of the spectra fall below this threshold. It is not surprising that around 81% of the spectra are associated with those of the LDI-1 RM since the latter is a mixture of the ore taken from the LDI mine site. Only 2.5% of the spectra are associated with the sulfide-rich RMs CDN-ME-1208 and PTC-1b. Despite the scarcity of the sulfide-rich phase, it is found that 49% of the average Pd concentration of 5.2 ppm was associated with it, with the remaining 51% associated with the amphibole phase similar to that in LDI-1 RM. In the case of M9-F1 discussed in detail above, 72% of the spectra are similar to those of LDI-1, 12% are similar to the sulfide-rich spectra (consistently with the PCA of Fig.4.4b), and 76% of the average Pd concentration of 23.8 ppm is located in the sulfide-rich phase. This correspondence can be seen by comparing the concentration map for palladium in M9-F1 of Fig.4.9 with the similarity maps of CDN-ME-1208 or PTC-1b (Fig.4.8b or c). One can see the clear correspondence between the warm colors of the two maps. The black colour areas in Fig. 4.9 corresponds to Pd concentrations smaller than 5 ppm (the estimated LoD on RMs). These black areas correspond approximately to the yellowish areas in Fig. 4.8d which are associated with the feldspar phase as discussed above.

We observe in Fig. 4.9 that the palladium concentration reaches several thousand ppm in some locations, indicating its significant inhomogeneous distribution at the scale of the laser scan (750 μm diameter spots 1 mm apart). Such palladium concentrations justify the doping of our RMs up

to 500 ppm. When the Pd concentration exceeded 500 ppm, we extrapolated our calibration curves using the positive quadratic fit used for concentration up to 500 ppm (Fig. 4.6).

Fig. 4.10a shows a histogram of the number of laser shots per 5 ppm palladium concentration interval, and Fig.4.10b shows the % contribution of each 5 ppm interval to the average concentration of the entire core. The maximum Pd concentration was restricted to 400 ppm in Fig. 4.10a for better visibility of the low-concentration region. As mentioned above, we considered the negative concentrations in the average concentration calculation, assuming that they statistically offset the effect of noise in the positive concentrations. Fig. 4.10b shows that most of the negative concentrations (83%) are between -10 and 0 ppm, so 10 ppm appears to be a practical LoD value (different from the IUPAC definition) for the core, implying that local concentrations <10 ppm are meaningless. Summing all % contributions below 10 ppm in Fig. 4.10b, we see that this sum represents only 2% of the average core concentration although they include 88% of the collected spectra (Fig. 4.10a), with the remaining 98% of the average core concentration coming from local concentrations >10 ppm. Therefore, setting Pd local concentrations which are lower than the estimated LoD of 10 ppm to 0 would still have provided a good estimate of the average Pd concentration of the whole quarter core. These results are quite consistent with our recent LIBS assisted with laser-induced fluorescence (LIBS-LIF) measurements done on another LDI core where the LoD was estimated to be about 1 ppm on the LDI-1 RMs. In that study, the proportion of the 24,120 spectra taken on the core yielding Pd concentrations below 10 ppm was estimated to be 91% and the contribution of local concentrations <10 ppm to the average concentration was estimated to be about 9% [29].

Tableau 4-6 **Global statistics by considering all laser shots on the core. Column 2: Proportion of laser shots associated with a reference material. Column 3: Proportion of the average Pd concentration (5.2 ppm) found in the corresponding reference material.**

Reference material	Proportion of laser shots	Proportion of the average Pd concentration
LDI-1	81.4%	51%
CDN-ME-1208	0.4%	8%
PTC-1b	2.1%	41%
Other ($\rho_{max} < 0.92$)	16.1%	0%

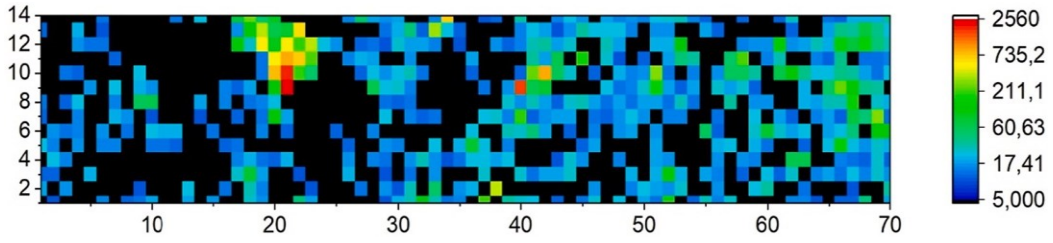

Figure 4-9 **Map of Pd concentration in M9-F1 on a logarithmic scale for values above 5 ppm.**

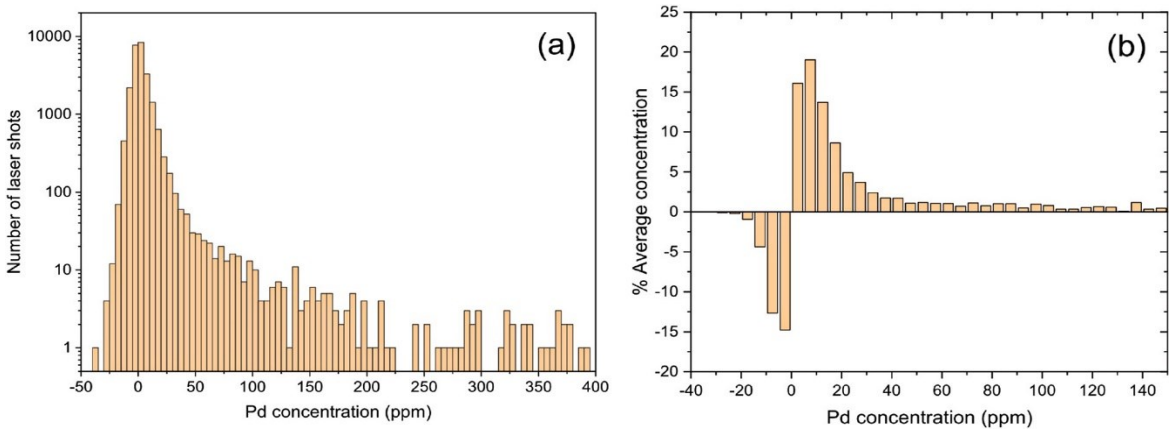

Figure 4-10 **(a) Histogram of the number of laser shots giving a concentration in intervals of 5 ppm for the whole quarter core. Zero concentrations corresponding to ρmax < 0.92 were evenly distributed between the +5 and - 5 ppm bins. The total number of laser shots is 25,165. (b) Histogram of the % contribution of each interval of 5 ppm to the average concentration.**

4.5 Conclusions

In this work, we developed a methodology to evaluate the palladium concentration of drill cores using LIBS. Our study involved a quarter of a drill core of about 100 cm long from the Lac des ˆIles palladium mine (Ontario, Canada) consisting of 9 fragments cut into 3 flat surfaces. The other half of the original core was analyzed by the mine laboratory using conventional methods. In order to determine the palladium concentration by LIBS, we prepared compressed pastilles of 3 reference material powders representative of the Lac des Iles mineralogy. These are an amphibole gabbro with low sulfide content (LDI-1) and two sulfide-rich materials (CDN-Me-1208 and PTC-1b) with different concentration of iron. These materials were doped with aqueous solutions of palladium chloride to give concentrations of around 25, 50, 100, 200 and 500 ppm. From the 3 sets of 6 compressed pellets (including the undoped samples), 3 univariate calibration curves were obtained for the Pd 348.115 nm line with an estimated limit of detection (LoD) of 5 ppm per single laser shot or 0.5 ppm for 100 shots. The palladium concentration was determined for each laser shot on the core using these calibration curves. To determine the appropriate calibration curve to use for a given laser shot, we selected the spectrum of the 3 undoped reference materials with the highest similarity to the local core spectrum by evaluating the Pearson correlation. A total of 25,165 spectra were collected from the core surface. Although the sulfide-rich phases account for only 2.5% of the surface area of the core analyzed, they contribute to nearly 50% of the average palladium concentration of the whole core. The core also contains around 16% feldspar for which no calibration curve was established due to the expected absence of palladium in this phase. Close examination of the palladium concentration distribution on the

core indicates that local concentrations below the practical value for LoD of 10 ppm on the core (as opposed to 5 ppm on reference materials using the IUPAC definition) contribute only about 2% of the average concentration although nearly 90% of the spectra yield local concentrations below 10 ppm. Analysis of LIBS results indicates significant variations in palladium concentration between fragment faces as well as across the 1 mm spacing of 750 µm diameter laser spots. Nevertheless, the measured average LIBS concentration of 5.2 ppm is close to the mine laboratory result (4.93 ppm) for half of the original core. However, the good agreement obtained by comparing the average value obtained by LIBS and that obtained in the laboratory must be taken with caution. Indeed, the laboratory analysis is linked to an average value on the total volume of the sample whereas the LIBS measurement is linked to a surface analysis. For a homogeneous sample, the surface is representative of the mass and it is then possible to obtain a good correlation between the LIBS and laboratory results. However, for a surface that is not necessarily representative of the mass, the two techniques can give different values. This effect is referred to as the nugget effect by the gold mining industry. Heterogeneity in the distribution of precious metals in the ore can cause the average concentrations of the two halves of a core sample to be different even when analyzed by conventional techniques.

The next step in this study will be to examine drill cores from Ni-Cu-PGE mines whose ore is much richer in sulfides than that of Lac des Iles. In addition, a measurement strategy to minimize the number of laser shots will be required for the practical application of LIBS at the mine site.

Declaration of Competing Interest

The authors declare the following financial interests/personal relationships which may be considered as potential competing interests: Francois Vidal reports financial support was provided by Natural Sciences and Engineering Research Council of Canada.

Data availability

Data will be made available on request.

Acknowledgements

We are grateful to Lionnel Djon from Impala Canada for providing us with quarter drill cores from the Lac des ˆIles mine and their laboratory analysis, as well as for the financial support of Impala Canada. This work was primarily supported by the National Science and Engineering Research Council of Canada (NSERC).

4.6 BIBLIOGRAHIE

[1] https://mining.ca/our-focus/critical-minerals/. Accessed in June 15, 2022.

[2] M.B. Mooiman, K.C. Sole, N. Dinham, The precious metals industry: global challenges, responses, and prospects, in: R.M. Izatt (Ed.), Metal Sustainability: Global Challenges, Consequences, and Prospects, J. Wiley, 2016, pp. 361–396.

[3] R.H. Sillitoe, The Challenge of Finding New Mineral Resources: An Introduction 15, Society of Economic Geologists, Special Publication, 2010, pp. 1–4.

[4] E. Herincs, M. Puschenreiter, W. Wenzel, A. Limbeck, A novel flow-injection method for simultaneous measurement of platinum (Pt), palladium (Pd) and rhodium (Rh) in aqueous soil extracts of contaminated soil by ICP-OES, J. Anal. At. Spectrom. 28 (2013) 354–363.

[5] J.L. Molloy, J.A. Holcombe, Detection of palladium by cold atom solution atomic absorption, Anal. Chem. 78 (2006) 6634–6639. [6] J. Tickner, J. O'Dwyer, G. Roach, M. Smith, Y. Van Haarlem, Analysis of precious metals at parts-per-billion levels in industrial applications, Radiat. Phys. Chem. 116 (2015) 43–47.

[7] Canadian Mining Industry Research Organization (CAMIRO) Exploration Division, Quality Control Assessment of Portable XRF Analyzers: Development of Standard Operating Procedures, Performance on Variable Media and Recommended Uses, CAMIRO Project 10E01, Phase I, June 9, https://www.appliedgeochemists.org/images/stories/XRF/pXRF%20Report%20Phase%20I%20Report%20rev% 20Oct%202013.pdf, 2011. Accessed in June 15, 2022.

[8] B. Lemi`ere, R.S. Harmon, XRF LIBS for Field Geology, John Wiley & Sons Ltd, 2021, pp. 1046–1173. Chapter 20.

[9] G.E. De Benedetto, R. Laviano, L. Sabbatini, P.G. Zambonin, Infrared spectroscopy in the mineralogical characterization of ancient pottery, J. Cult. Herit. 3 (2002) 177–186.

[10] K. Rifai, M. Laflamme, M. Constantin, F. Vidal, M. Sabsabi, A. Blouin, P. Bouchard, K. Fytas, M. Castello, B. Nguegang Kamwa, Analysis of gold in rock samples using laser-induced breakdown spectroscopy: matrix and heterogeneity effects, Spectrochim. Acta Part B 134 (2017) 33–41.

[11] I. Elhamdaoui, K. Rifai, J. Iqbal, N. Mohamed, S. Selmani, J. Fernandes, P. Bouchard, M. Constantin, M. Laflamme, M. Sabsabi, F. Vidal, Measuring the concentration of gold in ore samples by laser-induced breakdown spectroscopy (LIBS) and comparison with the gravimetry/ atomic absorption techniques, Spectrochim. Acta B 183 (2021), 106256.

[12] R.S. Harmon, R.E. Russo, R.R. Hark, Applications of laser-induced breakdown spectroscopy for geochemical and environmental analysis: a comprehensive review, Spectrochim. Acta Part B 87 (2013) 11–26.

[13] R.S. Harmon, G.S. Senesi, Laser-induced breakdown spectroscopy – a geochemical tool for the 21st century, Appl. Geochem. 128 (2021), 104929.

[14] D.A. Cremers, L.J. Radziemski, Handbook of laser-induced breakdown spectroscopy, J. Wiley (2013) 437.

[15] Y. Deguchi, Z. Wang, Industrial Applications of Laser-Induced Breakdown Spectroscopy, Plasma Science and Technology - Progress in Physical States and Chemical Reactions, Chapter 402, 2016, https://doi.org/10.5772/61915.

[16] R.S. Harmon, J.M. Lawley C, J. Watts, C.T. Harraden, A.M. Somers, R.R. Hark, Laser-induced breakdown spectroscopy – an emerging analytical tool for mineral exploration, Minerals 9 (2019) 718.

[17] D. Díaz, D.W. Hahn, A. Molina, Quantification of gold and silver in minerals by laser-induced breakdown spectroscopy, Spectrochim. Acta Part B 136 (2017) 106–115.

[18] D. Diaz, A. Molina, D.W. Hahn, Effect of laser irradiance and wavelength on the analysis of gold- and silver-bearing minerals with laser-induced breakdown spectroscopy, Spectrochim. Acta B 145 (2018) 86–95.

[19] D. Diaz, A. Molina, D.W. Hahn, Laser-induced breakdown spectroscopy and principal component analysis for the classification of spectra from gold-bearing ores, Appl. Spectrosc. 74 (2020) 42–54.

[20] R.S. Harmon, R.R. Hark, C.S. Throckmorton, E.C. Rankey, M.A. Wise, A.M. Somers, L.M. Collins, Laser-induced breakdown spectroscopy and principal component analysis for the classification of spectra from gold-bearing ores, Geostand. Geoanal. Res. 41 (2017) 563–584.

[21] A. Pochon, A.-M. Desaulty, L. Bailly, Handheld laser-induced breakdown spectroscopy (LIBS) as a fast and easy method to trace gold, J. Anal. At. Spectrom. 35 (2020) 254–264.

[22] K. Rifai, F. Doucet, L. Ozcan, ¨ F. Vidal, LIBS core imaging at kHz speed: paving the way for real-time geochemical applications, Spectrochim. Acta Part B 150 (2018) 43–48.

[23] F. Gervais, K. Rifai, P. Plamondon, L. Ozcan, ¨ F. Doucet, F. Vidal, Compositional tomography of a gold-bearing sample by laser-induced breakdown spectroscopy, Terra Nova 12417 (2019).

[24] S.C. Snyder, W.G. Wickun, J.M. Mode, B.D. Gurney, F.G. Michels, The detection of palladium particles in proton exchange membrane fuel-cell water by laser-induced breakdown spectroscopy (LIBS), Appl. Spectrosc. 65 (2011) 6.

[25] A.A. Al Shuaili, A.M. Al Hadhrami, M.A. Waki, Z.T. Alwahabi, Improvement of palladium limit of detection by microwave-assisted laser induced breakdown spectroscopy, Spectrochim. Acta B 159 (2019), 105666.

[26] K. Rifai, L.-Ç. Ozcan, ¨ F. Doucet, K. Rhoderick, F. Vidal, Ultrafast elemental mapping of platinum group elements and mineral identification in platinumpalladium ore using laser induced breakdown spectroscopy, Minerals 10 (2020) 207.

[27] K. Rifai, M.C. Michaud Paradis, Z. Swierczek, F. Doucet, L. Ozcan, ¨ A. Fayad, J. Li, F. Vidal, Emergences of new technology for ultrafast automated mineral phase identification and quantitative analysis using the CORIOSITY laser-induced breakdown spectroscopy (LIBS) system, Minerals 10 (2020) 918.

[28] N. Mohamed, K. Rifai, S. Selmani, M. Constantin, F. Doucet, L. Ozcan, M. Sabsabi, F. Vidal, Chemical and mineralogical mapping of platinum-group element ore samples using laser-induced breakdown spectroscopy and micro-X-ray fluorescence, Geostand. Geoanal. Res. 45 (2021) 539–550.

[29] I. Elhamdaoui, N. Mohamed, S. Selmani, P. Bouchard, M. Sabsabi, M. Constantin, F. Vidal, Rapid quantitative analysis of palladium in ores using Laser-Induced Breakdown Spectroscopy assisted with laser-induced fluorescence (LIBS-LIF), submitted to, J. Anal. At. Spectrom. (May 2022).

[30] P. Bouchard, M. Sabsabi, C. Padioleau, A. Blouin, “Hybrid LIBS System and method for gold ore mineral analysis”. US provisional application Filed in May 2018. NRC 2018–068, published November 2019. US patent 11,385,182 issued July 2022.

[31] P. Bouchard, M. Sabsabi, C. Padioleau, “High resolution and high throughput spectrometer”. US provisional application (NRC 2018–093). Filed May 2018, published October 2019. US patent 11,385,101 issued July 2022.

[32] D. Decharte, C. Perusse, T. Hofton, C. Roney, G. Marrs, S. Taylor, S. Olson, D. Thibodeau, D. Peck, B. Young, Feasibility study for Lac des Iles Mine incorporating underground mining of the Roby Zone, in: Technical Report, North American Palladium Ltd., 2018, p. 889.

[33] M.J. Lavigne, M.J. Michaud, Geology of North American Palladium Ltd'. Roby Zone Deposit, Lac des Iles 10, Explor Min Geol, 2001, pp. 1–17.

[34] B. Buss, C. Roney, D. Peck, D. Decharte, G. Marrs, J. Canosa, K. Hutton, L. Ritchie L. Therrien, Feasibility study incorporating the life of mine plan for Lac des Iles Mine, Thunder Bay, Ontario, Canada, in: NI 43-101 Technical Report, North American Palladium Ltd., 2017, p. 925.

[35] M.L. Djon, S.J. Barnes, Changes in sulfides and platinum-group minerals with the degree of alteration in the Roby, Twilight, and High Grade Zones of the Lac des Iles Complex, Ontario, Canada, Mineral. Deposita 47 (2012) 875–896.

[36] S.J. Barnes, T.S. Gomwe, The Pd deposits of the Lac des Iles complex, Northwestern Ontario, Rev. Econ. Geol. 17 (2011) 351–370.

[37] NIST Atomic Spectra Database Lines Data. https://physics.nist.gov/PhysRefData/ ASD/lines_form.html, 2022. Accessed in June 14, 2022.

[38] I.B. Gornushkin, J.M. Anzano, L.A. King, B.W. Smith, N. Omenetto, J. D. Winefordner, Curve of growth methodology applied to laser-induced plasma emission spectroscopy, Spectrochim. Acta B 54 (1999) 491.

[39] Z.Q. Hao, L. Liu, M. Shen, X.Y. Yang, K.H. Li, L.B. Guo, X.Y. Li, Y.F. Lu, X.Y. Zeng, Investigation on self-absorption at reduced air pressure in quantitative analysis using laser-induced breakdown spectroscopy, Opt. Express 24 (2016) 26521.

[40] IUPAC, General aspects of trace analytical methods – IV, in: Recommendations for Nomenclature, Standard Procedures and Reporting of Experimental Data for Surface Analysis Techniques 51, 1979, p. 2243.

CHAPITRE V

5 ARTICLE 2 - CRATERES PRODUITS PAR LASER DANS LES MINERAUX D'UN ECHANTILLON DE MINERAI DE PALLADIUM.

Laser-produced craters in minerals of a palladium ore sample.

Cratères produits par laser dans les minéraux d'un échantillon de minerai de palladium

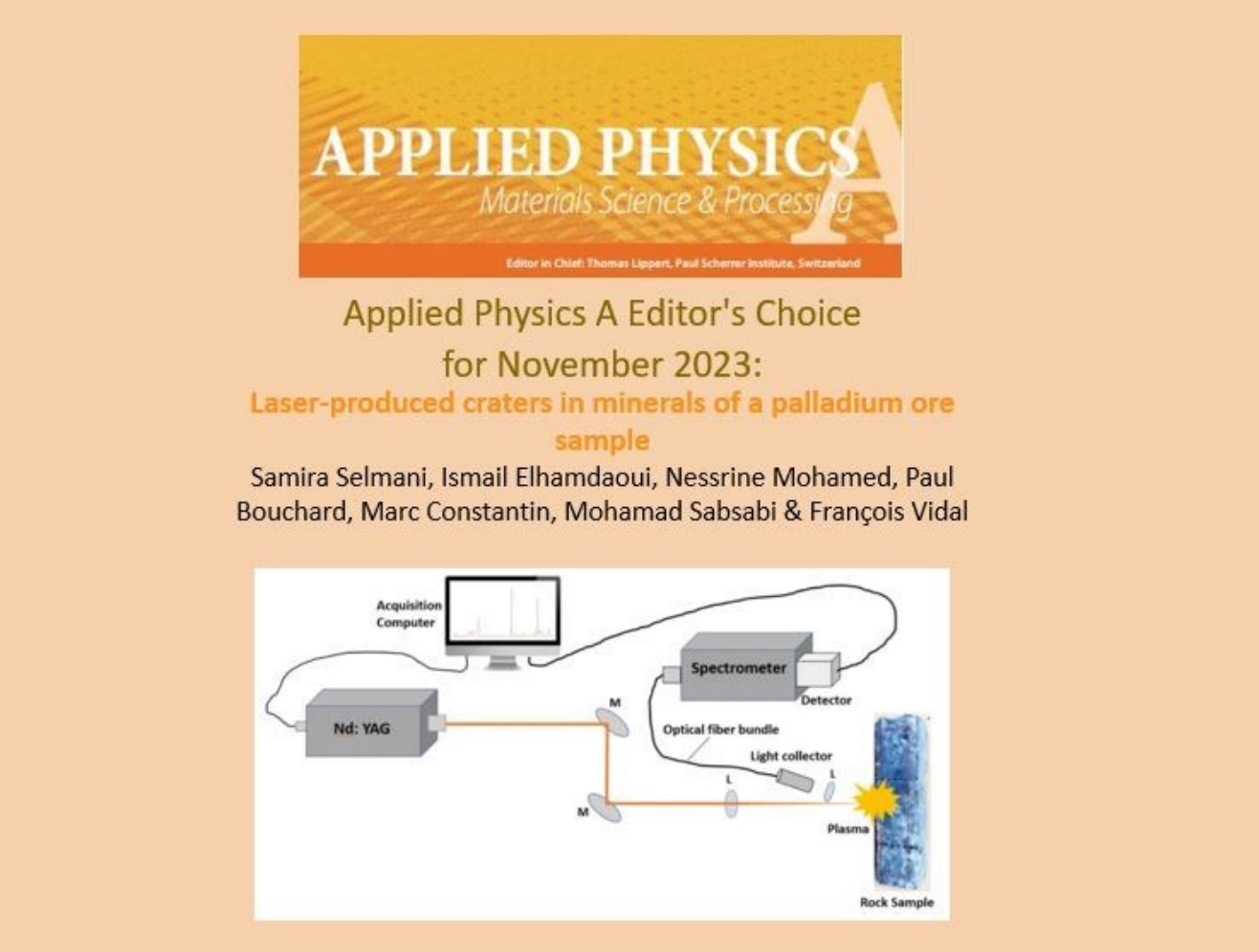

Notre figure 5.1 a fait la page couverture du numéro de novembre 2023 d'Applied Physics A

Auteurs :

Samira Selmani[1], Ismail Elhamdaoui[1], Nessrine Mohamed[2], Paul Bouchard[3], Marc Constantin[2], Mohamad Sabsabi[3], François Vidal[1]

[1]Institut National de la Recherche Scientifique, Centre ´énergie matériaux télécommunications, 1650 Lionel-Boulet blvd, Varennes, QC J3X 1P7, Canada

[2] Département de Géologie et de Génie Géologique, Université Laval, 1065 Avenue de la Médecine, Québec, QC G1V 0A6, Canada

[3] National Research Council of Canada, 75 de Mortagne Blvd., Boucherville, QC J4B 6Y4, Canada

Titre de la revue ou de l'ouvrage :

Article publié le 28 aout 2023 dans la revue Applied Physics A, numéro 129, volume 737.

https://doi.org/10.1007/s00339-023-06966-7

Contribution des auteurs :

Dans cet article, chaque auteur a apporté une contribution essentielle et complémentaire pour atteindre les objectifs de l'étude.

Samira Selmani, en tant que première auteure, a sélectionné l'échantillon, pris les mesures LIBS et les photos en microscopie optique. Elle a analysé et interprété les données, rédigé le manuscrit et effectué les corrections et révisions nécessaires pour finaliser l'article, avec une aide particulière de François Vidal.

François Vidal, a apporté des remarques pertinentes et des interprétations précieuses qui ont considérablement amélioré l'article. Il a également joué un rôle important dans l'amélioration de la qualité des images OCT des cratères, offrant des explications claires. Il a supervisé la correction et la révision de l'article.

Marc Constantin a validé l'interprétation de la partie minéralogique des roches, en apportant des remarques pertinentes basées sur l'analyse au microscope électronique à balayage (SEM) et la micro-XRF.

Mohamad Sabsabi a aidé à valider les résultats et les interprétations obtenus par LIBS (Spectroscopie de plasma induit par laser) et OCT (Tomographie par cohérence optique). Ses remarques pertinentes ont considérablement amélioré la qualité de l'article.

Paul Bouchard a aidé à préparer les échantillons pour les mesures OCT et la microscopie optique. Il a également apporté des conseils pertinents qui ont contribué à la précision des mesures et des analyses.

Nessrine Mohamed et moi avons préparés la cartographie élémentaire de l'échantillon. Elle a ensuite produit des images SEM de haute qualité pour caractériser les échantillons et a fourni des commentaires utiles pour améliorer le travail.

Ismail Hamdaoui a contribué à l'amélioration du contenu de l'article grâce à ses remarques constructives.

François Vidal, Marc Constantin et Mohamad Sabsabi ont supervisé l'article dans son ensemble.

Tous les coauteurs ont offert leur soutien pour la rédaction et ont contribué à la révision du manuscrit.

Chacun de ces contributeurs a joué un rôle clé dans le succès de cet article, permettant une analyse complète et rigoureuse de l’échantillon de minerai, et assurant la robustesse et la validité des conclusions tirées

5.1 Abstract

Laser-induced breakdown spectroscopy (LIBS) is an emerging technique in geochemistry that allows rapid in-situ analysis of the elemental composition and concentration of minerals by laser ablation of the material surface and measurement of the light emitted by the resulting plasma. However, this type of application is still under development for geochemical analyses. Indeed, it is still difficult to know how minerals are ablated under laser pulses in the context of LIBS geochemical analysis using a high-power Q-switched Nd:YAG laser operating at 1064 nm with pulse durations on the order of nanoseconds. Important questions remain unanswered regarding the volume sampled by the laser beam on the minerals to be analyzed, as well as the plasmas induced by the laser on the minerals in air at atmospheric pressure. The objective of this work is to provide insight into laser-mineral interactions within the framework of LIBS geochemical analysis of ore samples with emphasis on the characterization of plasmas and laser ablation craters under ambient air at atmospheric pressure. We study the crater morphology in the three main phases of a palladium ore fragment (Lac des Iles mine, Canada), namely plagioclase feldspar, amphibole and sulfides [Mohamed et al., Geostand Geoanal Res 45:539, (2021)] We performed four series of laser shots (50, 250, 500 and 1000 shots) in the three mineral phases and characterized the morphology of the craters obtained by scanning electron microscopy and optical coherence tomography. It turns out that laser ablation is most effective in plagioclase, presumably due to its lower thermal conductivity. In addition, the temperature and electron density of the plasma were determined for each phase from the iron and nickel lines of LIBS spectra taken 4 µs after the laser shots. They are between 6300 and 8600 °C and about 2 × 1017 cm^{-3}, respectively.

Keywords Laser-Induced Breakdown Spectroscopy (LIBS) · Laser ablation · Plasma characterization · Mineral phases · Crater morphology

5.2 Introduction

Many characteristics of laser-induced breakdown spectroscopy (LIBS) make it an attractive analytical tool for the analysis of geological materials, both in the conventional laboratory and in the field [1–3]. LIBS is a simple yet versatile technique that can detect all chemical elements in any material with a sensitivity suitable for many applications. It requires little or no sample preparation; multi-element analysis of samples can be performed in real time; only a small portion of the sample is required for analysis; and it can detect trace and minor elements in a sample, which is important in many geological studies. Several studies have focused on the LIBS technique for applications in geological and environmental materials analysis [4–8]. By using calibration samples, it is possible to determine the concentration of elements present in samples of the same compositional family. Compared to LIBS, X-ray fluorescence (XRF) techniques suffer from a lack of sensitivity for light elements below Mg. Furthermore, in a portable format, XRF can hardly quan- tify traces of precious metals due to its low sensitivity and thus high detection limit [9]. As for infrared spectroscopy, it can determine the mineralogy of rock samples but not their elemental composition [10].

In LIBS analysis, a pulsed laser beam with a fluence that can range from a fraction to hundreds of J cm^{-2}, depending on the duration of the laser pulses (typically from tens of femtoseconds to a few nanoseconds) and the material to study, is focused on the sample surface, causing localized ablation of a very small amount (typically less than 1 mg) of the material. The ablated material initially forms a weakly ionized atomized plasma at high temperature (~ 20,000 K) which fairly well reflects the stoichiometry of the material [11] in the interaction zone. The plasma cools by increasing its volume and by emitting radiation on a time scale of typically a few microseconds. The plasma radiation consists of spectral lines from the de-excitation of atoms and ions, which are the unique signature of the elements present in the plasma, and a background of continuous radiation from electron ion recombination and deflection of free electrons (bremsstrahlung radiation). A particularly interesting geochemical application of LIBS is the quantification of metals in ores at low ppm levels. Analysis of mine samples using conventional wet chemistry or fire assay techniques involves a lengthy sample preparation process and logistical waiting times of at least 24 h, resulting in production delays at mining or exploration sites [12]. LIBS can in principle provide quantitative results for a typical drill core within minutes without preparation. In particular, LIBS has been studied by our team for the quantification of gold [13–15] and palladium [16, 17] in solid ores where they are present in trace amounts, typically in the order of 1–10 ppm. Despite remarkable advances in the use of LIBS in geochemistry in recent years [7, 18–21], the

understanding of the interaction between the laser and the solid rock surface is still very limited. This issue is further complicated by the fact that ores are typically composite media containing several different minerals on scales ranging from micrometers to centimeters. For example, in the case of palladium ore from the Lac des Iles (LDI) mine, we have identified about ten different minerals using a variety of microanalytical techniques (electron probe microanalysis, scanning electron microscope, and μ-XRF) and a database of LIBS spectra [19]. In its gabbronorite variety (of the same type as the ore sample studied here), this ore presents three main phases that occupy dis- tinct areas of a few mm^2 on its surface, namely: (1) calcium-rich plagioclase feldspar (mainly bytownite), (2) amphibole (mainly hornblende), and (3) sulfides (mainly chalcopyrite, pentlandite, pyrrhotite and pyrite). In principle, the physical process of laser ablation and thus the amount of material ablated, is different for each mineral phase because they all have different compositions and physicochemical properties. Understanding laser-mineral interactions is relevant not only for practical applications on Earth, but also for extraplanetary exploration [22].

While laser ablation of rock samples for geochemical analysis has been little studied, ablation of materials by intense irradiation of laser pulses has been investigated in several other fundamental and applied fields [23, 24], particularly in analytical chemistry [25–27]. Since the first observation of laser ablation of a carbon rod in 1962 [28], laser ablation has been studied on many solid surfaces. The materials used include metals, semiconductors, dielectrics, ceramics and polymers [29]. The influence of laser parameters such as fluence [30, 31], pulse duration [32], laser spot size, number of laser shots [33], and wavelength [34] on crater morphology in different materials is still under investigation. The characterization of crater morphology has been mainly performed by methods such as scanning electron microscopy (SEM) [35], atomic force microscopy (AFM) [36], white light interferometry [37, 38], focused ion beam SEM (FIB-SEM) [39], optical microscopy [40], casting [41], and X-ray computed tomography [42].

Laser ablation is a complex process that depends on the nature of the material, the surrounding atmosphere, and the characteristics of the laser pulse [29]. Laser ablation is generally considered to result from a combination of photochemical processes, in which optically excited electrons lead directly to bond breakage, and photothermal processes, which lead to thermal bond breakage [43]. Photothermal processes are generally understood as the absorption of laser energy by free electrons through inverse bremsstrahlung and energy transfer from the hot electrons to the plasma and material [44]. The latter effect is favored by long laser pulses (>> 1 ps) and long wavelength. LIBS typically uses near-infrared nanosecond pulses, such as those provided by Nd:YAG lasers, to generate hot plasmas with strong emission lines.

The aim of this work is to provide an overview of laser- mineral interactions in the context of LIBS geochemical analysis of ore samples with a focus on plasma characterization and laser ablation craters under ambient conditions in air at atmospheric pressure. For this purpose, we specifically selected a gabbronorite that is representative of the palladium ore from the LDI mine and whose palladium concentration has been quantified by LIBS [16] as well as by LIBS assisted with laser induced fluorescence (LIBS- LIF) [17]. The sample studied here was characterized by μ-XRF in order to clearly identify and map the main mineral phases where laser ablation was performed. We studied the laser ablation craters created on the surface of LDI ore samples for the three main mineral phases (plagioclase, amphibole, sulfides) for several series of laser shot numbers (50, 250, 500 and 1000) using 2D images provided by the SEM and 3D profiles provided by an in-house optical coherence tomography (OCT) based system [45]. Although LIBS spectra can be obtained with a single laser shot [16], many laser shots are required to produce observable craters at the laser fluence and wavelength used, and thus to estimate the average amount of matter ablated per laser shot. The electron density and excitation temperature of the plasma were also estimated from the Fe and Ni emission lines of the LIBS spectra.

5.3 Materials and methods

5.3.1 Experimental setups

The experimental setup used for crater formation and LIBS spectra collection is schematically shown in Fig 5. 1. It basically consists of three elements: a laser, a spectrometer and a detector. The Nd:YAG laser used (CFR 200 from Quantel Laser by LUMIBIRD) can deliver pulse energies up to 200 mJ with a tunable repetition rate up to 20 Hz at a fundamental wavelength of 1064 nm, and with a full width at half maximum (FWHM) of the laser pulse time profile of 8 ns. The laser beam was focused on the rock surface by a 20 cm focal length lens. For the collection of LIBS spectra, the plasma emission was focused onto the circular input end of a fiber optic bundle consisting of twenty-five 100 μm diameter fibers. The vertically aligned output of this bundle was positioned in front of the entrance slit of a Czerny- Turner spectrometer (McPherson model 207) to match the pixel array of the intensified charge-coupled device (ICCD) (Istar DH720-25H-05, Andor Technology). The spectrometer has a focal length of approximately 0.67 m and a numerical aperture of F/5.8, covering wavelengths from 180 to 650 nm employing a UV-enhanced grating of 2400 grooves/mm. The corresponding reciprocal linear dispersion is approximately 12 pm/pixel at 267 nm. The spectrometer slit was set at 20 μm to obtain both good signal intensity and spectral resolution.

Before proceeding with the laser ablation experiments, we characterized the transverse energy distribution of the laser beam. For this purpose, we measured the laser beam in the focal plane of a plano-convex lens with a focal length of 250 mm at 1064 nm using an SP620U camera (with a pixel size of 4.4 µm × 4.4 µm) and the beam analysis software Ophir/Spiricon BeamGage. The 2D and 3D images of the energy profile are shown in Fig 5. 2. The beam has a circular shape with a diameter of approximately 750 µm at four standard deviations. The top of the beam contains some small speckles that form an overall slightly sloped profile.

The laser parameters used in this study are listed in Table 5. 1. The laser energy was 80 mJ per pulse while the laser spot diameter on the target was 750 µm, resulting in a fluence of approximately 18 J cm^{-2} or an irradiance of 2.3 GW cm^{-2}. These parameters are the same as those optimized for the measurement of palladium concentration by LIBS in a previous study [16]. For LIBS signal acquisition, a delay time of 4 µs after the laser pulse (delay before signal integration starts) and a gate width of 10 µs (signal integration time) were used. These two values were chosen to obtain a near-optimal signal-to-noise ratio for our setup. All measurements were performed in air at atmospheric pressure with a laser repetition rate of 2 Hz, which is slow enough to avoid aerosols generated by previous laser shots. All measurements reported in this paper were performed within a few hours to minimize possible variations in configuration and atmospheric conditions.

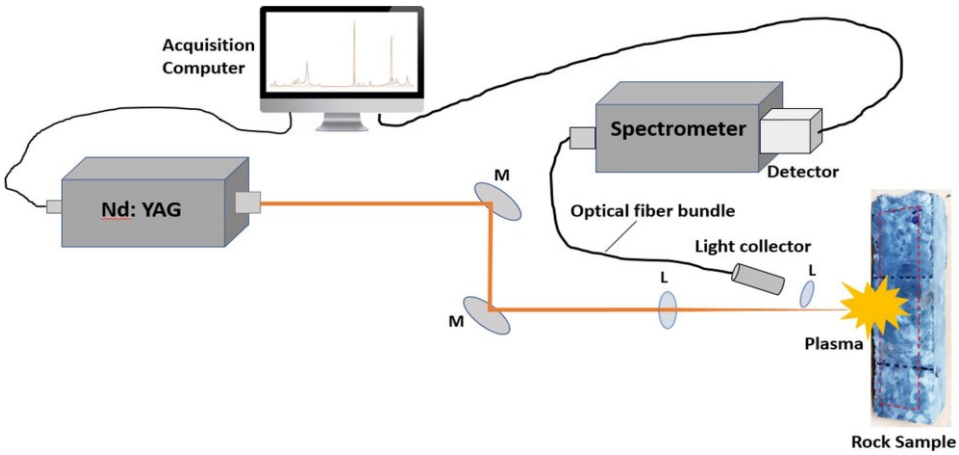

Figure 5-1 **Schematic representation of the LIBS experimental setup. Labels L and M refer to lens and mirror, respectively.**

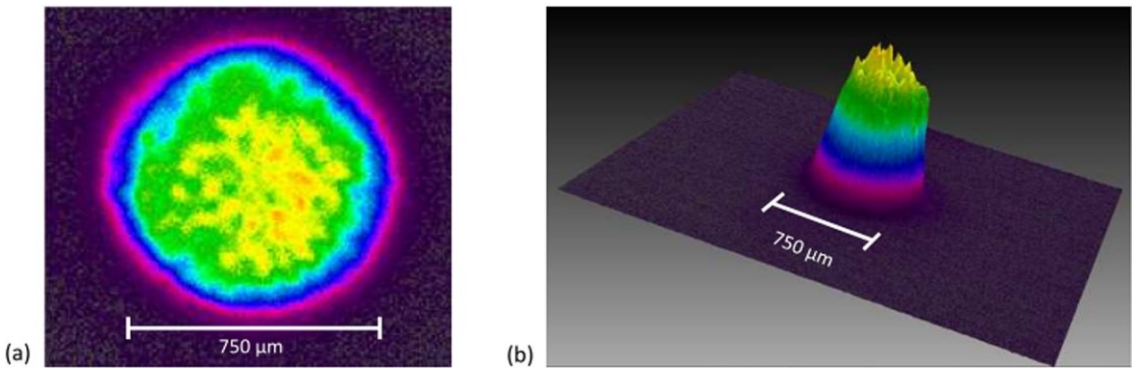

Figure 5-2 Transverse energy profile of the laser beam. 2D profile (a) and 3D profile (b)

Tableau 5-1 LIBS parameters used for crater formation.

Parameter	Value
Laser energy	80 mJ
Laser spot diameter	750 µm
Delay time	4 µs
Gate width	10 µs
Repetition rate	2 Hz
Spectrometer slit	20 µm

The geochemical study was carried out using a µ-XRF M4 Tornado analyzer (Bruker GmbH, Germany). The µ-XRF analyzer is equipped with an Rh X-ray tube with a Be window, a polycapillary focusing optics, two silicon drift X-ray detectors (type SDD VH30P), a large sample chamber, and a motorized stage for sample positioning. The spot size of the incident X-ray beam was set to 20 µm and the acquisition time per pixel was 5 ms. The acquisition and processing of the µ-XRF data was performed using the software supplied with the instrument which allowed qualitative analysis (single and multi-element mapping) as well as quantification based on fundamental parameters (standardless) of the X-ray spectra [46]. For a selected area, a complete X-ray spectrum was acquired for each pixel within a grid. The multi-element distribution map provided information on the surface area distribution occupied by the mineral phases present in the scanned area.

5.3.2 Palladium ore sample

LIBS and µ-XRF analyses and laser ablation cratering were performed on a fragment of drill core from the LDI mine (Fig 5. 3). The LDI mine is located in the Mine Block Intrusion, 106 km northwest of Thunder Bay, Ontario, Canada. The LDI complex is a mafic to ultramafic intrusive complex and

hosts significant PGE deposits [47]. The sample was collected from the B3 Zone deposit, which is hosted within the gabbronorite unit. The same surface was studied in [16] to illustrate a method for determining palladium content in ore using LIBS. This surface was also chosen for this study because of its exceptionally large, homogeneous, well- defined phase zones.

Half of the original one-meter drill core was analyzed by conventional methods. Its average elemental chemical content is summarized in Table 5. 2. It can be seen that Si is the major constituent followed by Mg, Al, Ca and Fe. This table is provided only to give a general idea of the elemental com- position of the ore. As shown in Fig 5. 3, we focus instead on the analysis of the major mineral phases present in the ore.

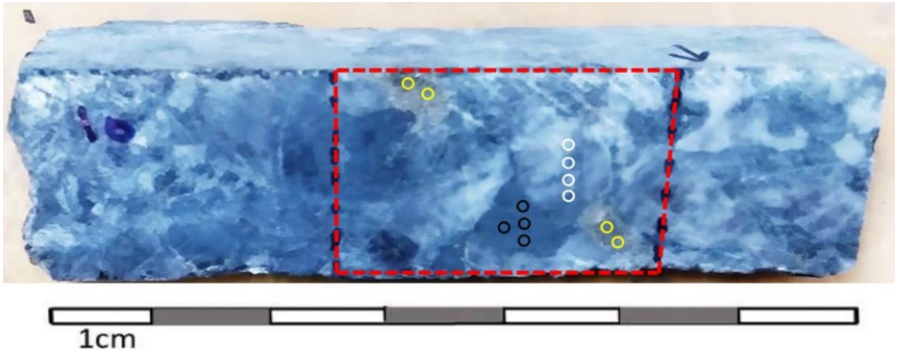

Figure 5-3 **Enhanced contrast photograph of the palladium ore sample analyzed in this study. The μ-XRF analysis was conducted in the area delineated by the red dashed lines. The approximate locations of the 12 craters examined in this study are indicated by circles in three different mineral phases: plagioclase feldspar (white circles), amphibole (black circles), and sulfides (yellow circles).**

Tableau 5-2 **Partial elemental chemical composition of the I ac des Iles drill core used in this study as determined by mine laboratory.**

Identification	Rock type	Elemental composition									
		Pt (ppm)	Pd (ppm)	Si (%)	Ca (%)	Fe (%)	S (%)	Cu (%)	Ni (%)	Al (%)	Mg (%)
18-805-X097924	Gabbronorite	0.568	4.93	24.2	6.6	4.7	0.35	0.14	0.31	7.7	7.8

5.4 Results and discussion

5.4.1 Mineralogical identification

A μ-XRF mineral identification procedure was carried out as described in our previous work [19]. Briefly, the multielement map shown in Fig 5. 4 was first obtained. Then, the relative element concentrations provided by the instrument software were obtained at selected locations on the map (small triangles near the mineral labels in Fig 5. 4). The minerals were then identified by

comparison with the generic formulas of the most likely minerals. Additional information from our previous study of samples of the same provenance was also employed. This included information from polarized light microscopy and electron probe microanalysis. The analysis confirmed the presence of minerals belonging to three different phases: amphibole, plagioclase and sulfides. Amphibole is mainly represented by hornblende (light pink zones), plagioclase by bytownite (blue zones) and sulfides by pyrrhotite, pentlandite, pyrite (deep pink and orange zones) and chalcopyrite (light green zones). The generic chemical composition of these minerals is given in Table 4.3, together with their mass density.

It should be noted that the mineral phases of rocks are rarely perfectly homogeneous, resulting in more complex compositions than those represented by their generic formulas. For example, electron probe microanalysis (EPMA) performed in our previous study on an ore of the same provenance (Supplementary Information of [19]) has shown the presence of a small amount of nickel and other metals in hornblende, which may be magnesium substitutes or micro- inclusions. Traces of iron were also found in bytownite. The presence of iron and nickel is clearly visible in the LIBS spectra of the three phases presented in Sect. 5.4.3, where their intense lines are used to determine plasma properties.

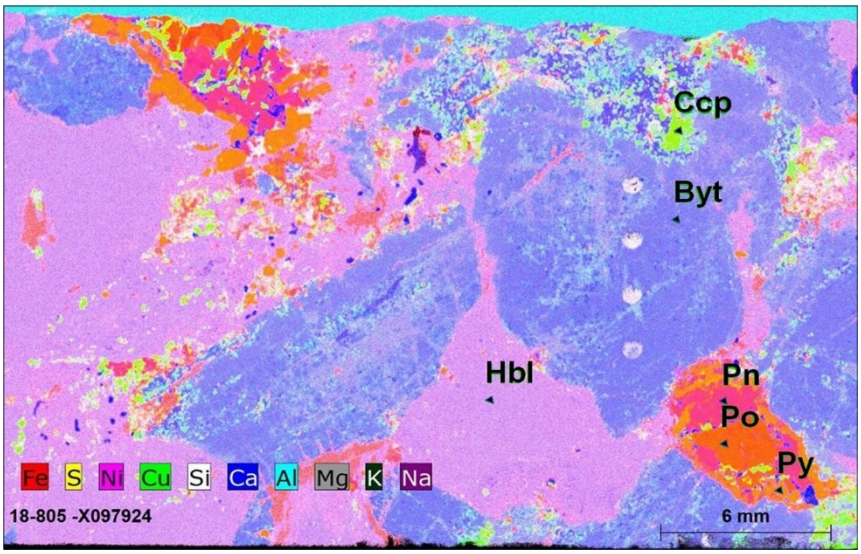

Figure 5-4 **Combined μ-XRF elemental map of the area outlined by the red dashed lines in Fig. 5.3 with identification of some minerals at locations represented by small triangles: pyrite (Py), chalcopyrite (Ccp), bytownite (Byt), hornblende (Hbl), pentlandite (Pn) and pyrrhotite (Po). The four vertically aligned circles near the bytownite label are deep ablation craters produced on this phase. The other craters are not clearly visible on this map.**

5.4.2 Cratering by laser ablation

Four craters were created at four different locations in each of the three main phases identified (plagioclase, amphibole, sulfides). Each crater was created with a different number of consecutive laser shots (50, 250, 500, 1000) at the same energy of 80 mJ per pulse and the same focal spot diameter of 750 µm. Photographs of the rock sample from Fig. 5.3, but with the actual craters, are shown in Fig 5. 5. Figure 5.5a shows the entire rock surface with the mineral phase boundaries drawn directly on the surface. The red dashed rectangle in

Tableau 5-3 Results of semi- quantitative analysis for our LDI gabbronorite sample and corresponding mass density

Phase	Main mineral	Generic mineral formula	Mass density (g cm−3)
Amphibole	Hornblende (Hbl)	$(Ca, Na)_2 (Mg, Fe, Al)_5 (Al, Si)_8 O_{22} (OH)_2$	3.14
Plagioclase	Bytownite (Byt)	$(Ca_{0.7-0.9}Na_{0.3-0.1}) [Al(Al, Si)Si_2 O_8]$	2.71
Sulfides	Pyrrhotite (Po)	$Fe_{0.8-1.0}S$	4.61
	Pentlandite (Pn)	$(Ni, Fe)_9S_8$	4.80
	Chalcopyrite (Ccp)	$CuFeS_2$	4.19
	Pyrite (Py)	FeS_2	5.01

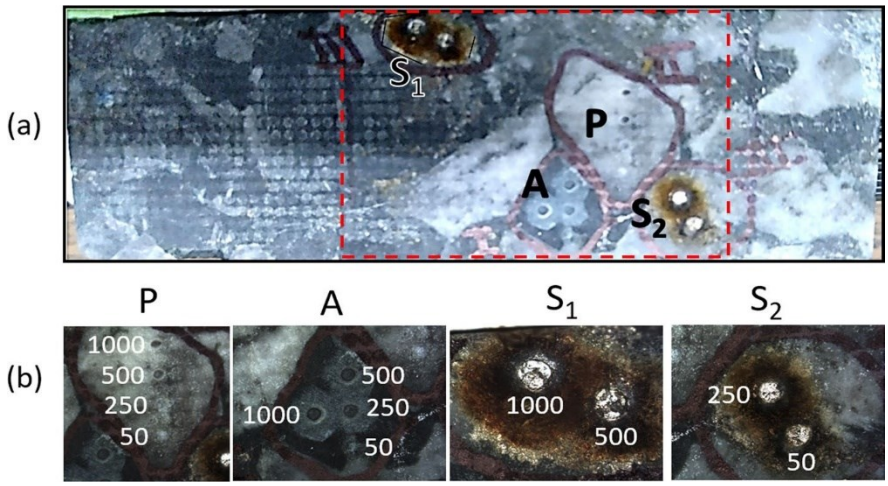

Figure 5-5 Photographs of the rock fragment after cratering by laser ablation. a Photograph of the entire surface (see Fig. 3). The red dashed rectangle represents the area scanned by µ-XRF. b Magnifcation of the areas labeled P, A, S1 and S2 in (a). The P zone is plagioclase, the A zone is amphibole, and the S1 and S2 zones are sulfides. Crater labels indicate the number of laser shots at the same location.

Fig. 5.5a corresponds to the area analyzed by µ-XRF (Fig. 4). Figure 5b magnifes the areas where the craters were formed. The number of laser shots corresponding to each crater is shown.

The craters look different in the three phases. In the sulfides (S1 and S2) a white metallic sheen appears at the bottom of the craters. This could be due to sulfur vaporization (sulfur vaporizes at 445 °C while iron vaporizes at ~ 3000 °C [48]), leaving a pure metallic phase (Fe, Ni, Cu) at the bottom of the crater. In addition, dark regions appear around the craters due to ejecta and oxidation reactions. Despite these transformations, the latter craters can not be clearly identified on the μ-XRF map in Fig 5.4. This is probably because the chemical changes due to ablation are below the absolute detection limit of μ-XRF. In amphibole (A), the craters appear as dark spots (except for the 50-shot crater) surrounded by a white rim and a larger white disk, which contrasts with the normal dark appearance of hornblende. These craters are also not visible on the μ-XRF map. In plagioclase (P), the craters appear as white or dark spots surrounded by a white rim, which are clearly visible on the μ-XRF map. The light color of the circular spots on the μ-XRF map suggests a chemical change that caused silicon to predominate at the bottom of the craters, probably a consequence of the high silicon content of bytownite and the high vaporization temperature (2355 °C) [48] of this element. As we will see from the OCT images, these craters are significantly deeper than those formed in the other phases.

SEM images at 300X magnification have been acquired with a FEI Inspect F50 instrument. Figure 5.6 shows two examples of craters for each of the three main phases: one obtained with 50 laser shots (first row) and one obtained with 1000 laser shots (second row). The craters produced in sulfides appear as solidified melt, consistent with the high metal content of this phase. Laser heating probably breaks the sulfur-metal bonds, leaving a pool of molten metal in the crater after the sulfur has evaporated. Crater diameters in this phase are close to 1 mm, significantly larger than the estimated laser spot size (750 μm). Amphibole shares with sulfide the appearance of a solidified melt, particularly evident in the 50-shot crater, while the 1000-shot crater has a more well-defined circular shape than in the sulfide phase. The crater diameter of 720 μm is similar to the laser spot size. In contrast, the bottom of the craters in plagioclase has a smoother but porous texture (note that the white spot in the 50-shot case and the black spot in the 1000-shot case are likely due to localized charge accumulation, as this material has a low electrical conductivity). The crater diameters in this case are approximately 800 μm.

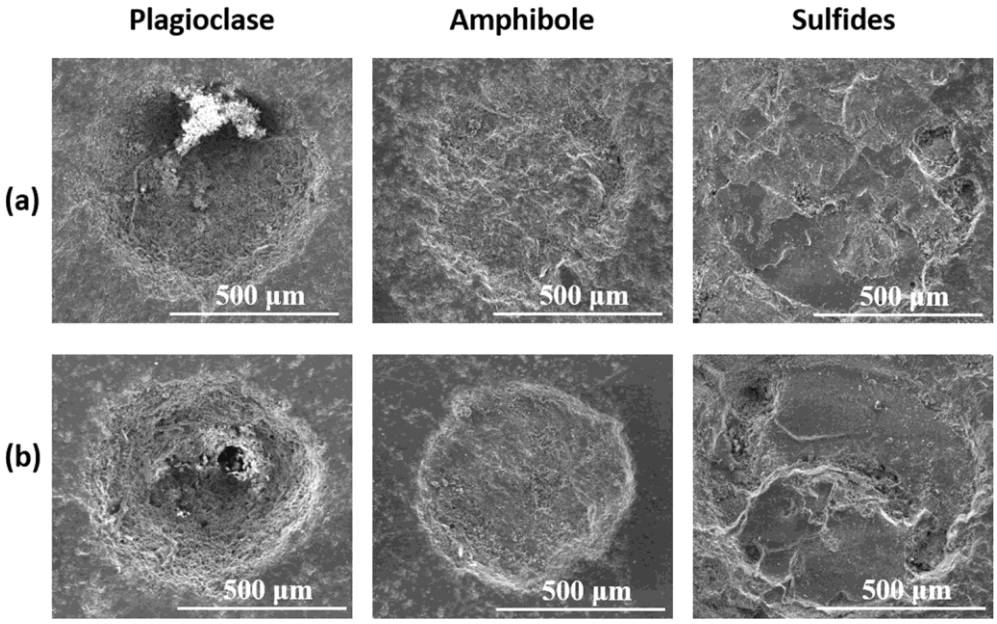

Figure 5-6 **300X SEM images obtained with secondary electrons that show laser ablation craters in the three main mineral phases for (a) 50 and (b) 1000 laser shots.**

Images with lower resolution than SEM, but with 3D details, were obtained using the OCT technique.

The OCT system used in this work was developed and operated at the National Research Council of Canada [45]. The results are shown in Fig 5.7 for the three main mineral phases (columns) and for the four numbers of laser shots (rows). In these images, the overall surface tilt of a few degrees along the X and Y axes was compensated for by rotating the data, and the surface position Z = 0 was determined by averaging the Z coordinates around the sides of each box.

Craters are much deeper in plagioclase (~ 700 µm per 1000 laser shots) compared to amphiboles and sulfides (less than 200 µm). In plagioclase, craters have a fairly regular truncated cone shape. For sulfides, the surface inside and outside the craters is highly undulating, suggesting melting of the material near the laser focus, consistent with the corresponding SEM images (Fig 5.6), and possibly also migration of the material out of the crater. Amphibole shares many characteristics with sulfides in that the craters are shallow, and their interior surfaces are rather irregular, with the possible exception of the 1000 shot case. However, the area outside the crater is flatter than in sulfides.

Figure 5.7 also indicates the volumes of the craters calculated from the OCT data. The most accurate volume calculations are probably for the plagioclase craters due to their greater depth. In this phase, the volume appears to increase steadily with the number of laser shots and tends

to be constant after about 250 laser shots. The saturation effect is most likely due to the decrease of the laser fluence (energy/surface) due to the increase of the effective interaction surface when the laser illuminates the inclined walls of the crater [49]. The defocusing of the laser as the crater deepens plays a minor role because the depth of field of the laser is greater than 2 mm. There appears to be a less consistent trend in the evolution of crater volume as a function of the number of laser shots in the amphibole. Given the shallowness of the craters, the accuracy of the volume calculation may not be sufficient to identify the true volume trend as a function of the number of laser shots. Volume calculations in sulfides are the least accurate because of the shallowness of the craters and the waviness of the surface around the laser focus, which makes it difficult to define the ground level Z = 0. This surface condition can be explained by the melting of material around the crater, the ejection of molten material, and the formation of oxides. In fact, the sulfide phase is an aggregate of at least four sulfides in different proportions, each with different physical properties. This is in sharp contrast to plagioclase, which forms a single homogeneous crystal. Considering the first 50 laser shots, we can estimate the volume ablated per laser shot to be 10^{-4}–10^{-3} mm^3 in the three phases for the laser parameters used. Using the mass densities given in Table 5.3, we can estimate that the mass ablated by laser shot is approximately 1.25 μg for hornblende, 2.71 μg for bytownite, and between 1.68 and 2.00 μg for sulfides.

To rationalize our observations, we considered some thermodynamic properties of the mineral phases. According to the Bowen reaction series [50, 51], calcium-rich plagioclase feldspars such as bytownite have a higher melting temperature (~ 1400 °C) than amphibole (~ 900 °C). With respect to sulfides, pyrite is known to transform to pyrrhotite at temperatures as low as 743 °C. However, pyrrhotite melts at 1190 °C [52]. Pentlandite melts near 900 °C [53] while chalcopyrite melts at about 950 °C [48]. These values for

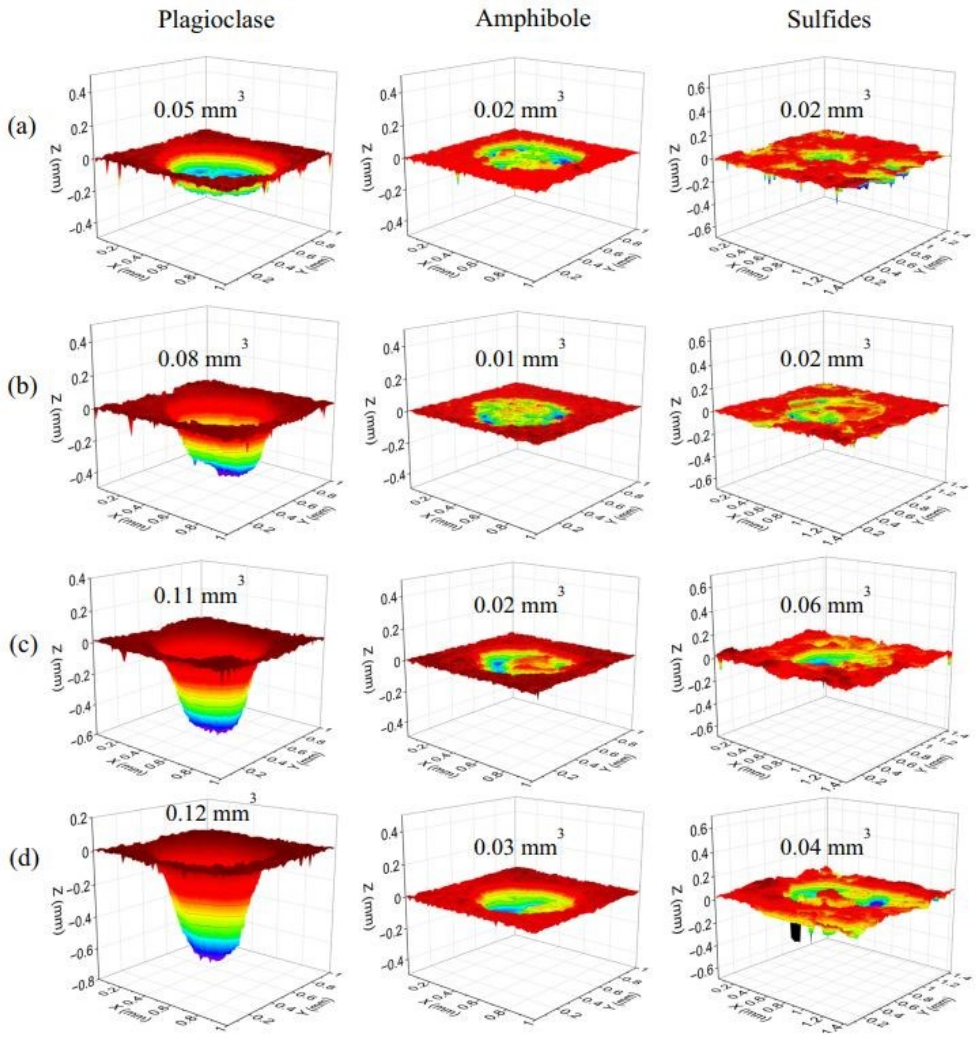

Figure 5-7 **OCT images of the ablation craters for the three main mineral phases and for diferent numbers of laser shots: 50 (a), 250 (b), 500 (c), and 1000 (d). The false colors correspond to the relative height of the craters from the bottom to the surface. Each crater profle is shown in a cube of 1 mm in length for plagioclase and amphibole, and 1.4 mm for sulfdes. The calculated volume of each crater in mm3 is indicated.**

sulfides are consistent with the amount of melt in and around laser-generated craters reported in [54]. These melting temperatures are generally consistent with the crater texture observed in SEM images (Fig 5.6), which show that the texture of sulfide and amphibole craters resembles a solidified melt, in contrast to the plagioclase which is more smooth and porous. Although it was found in [55] that the ablated volume decreases with increasing melting temperature for Sn, Pb, Ni and Si, this relationship clearly does not hold in our case.

As we know, laser ablation is a complex process that involves several physicochemical properties of the material, as well as the interaction of the laser with the solid surface and with the plasma. Interestingly, in the pre- sent cases, there is an inverse correlation between the crater volumes

and the thermal conductivity of the mineral phases. Thermal conductivity is lower in plagioclase (1.5–2.5 W m^{-1} K^{-1}) and higher in amphiboles (2.5–5.0 W m^{-1} K^{-1}), with the exact values depending on the phase composition [56], and sulfides (19.2, 4.6, and 10.7 W m^{-1} K^{-1} for pyrite, pyrrhotite, and chalcopyrite, respectively) [57]. Thermal conductivity is known to play an important role in nanosecond pulse laser ablation, as high thermal conductivity generally means that more of the laser energy deposited on the surface is rapidly dissipated within the material, leaving less available for vaporization of the material at the surface [44]. A similar correlation between crater volume and thermal conductivity can be found in [39] where experiments were performed on polymers, Si, SiO_2 and Al. Thermal conductivity is also a critical parameter to understand the higher ablation efficiency of ultrashort laser pulses at a given fluence, since in this case the thermal loss of the energy absorbed at the surface to the body of the material does not have time to operate.

5.4.3 LIBS spectra and plasma properties

Additional characteristics of the laser ablation in the mineral phases of our sample are provided by the LIBS spectra as a function of the number of laser shots. The spectra shown in Fig. 5.8 were recorded in the 1000 shot crater of each phase. The spectral range was chosen around the Pd I line at 348.115 nm, which was used to determine the palladium content in [16] (the line is too small to be visible here). The spectral lines are dominated by the high emission elements iron and nickel. These elements are normal constituents of sulfides (Table 5.3). Iron is a normal component of hornblende, but nickel is less common. As mentioned above, iron and nickel are not normally present in bytownite, but can be found as traces in the form of micro-inclusions. Here we focus mainly on the Fe and Ni lines as we use them to determine plasma properties.

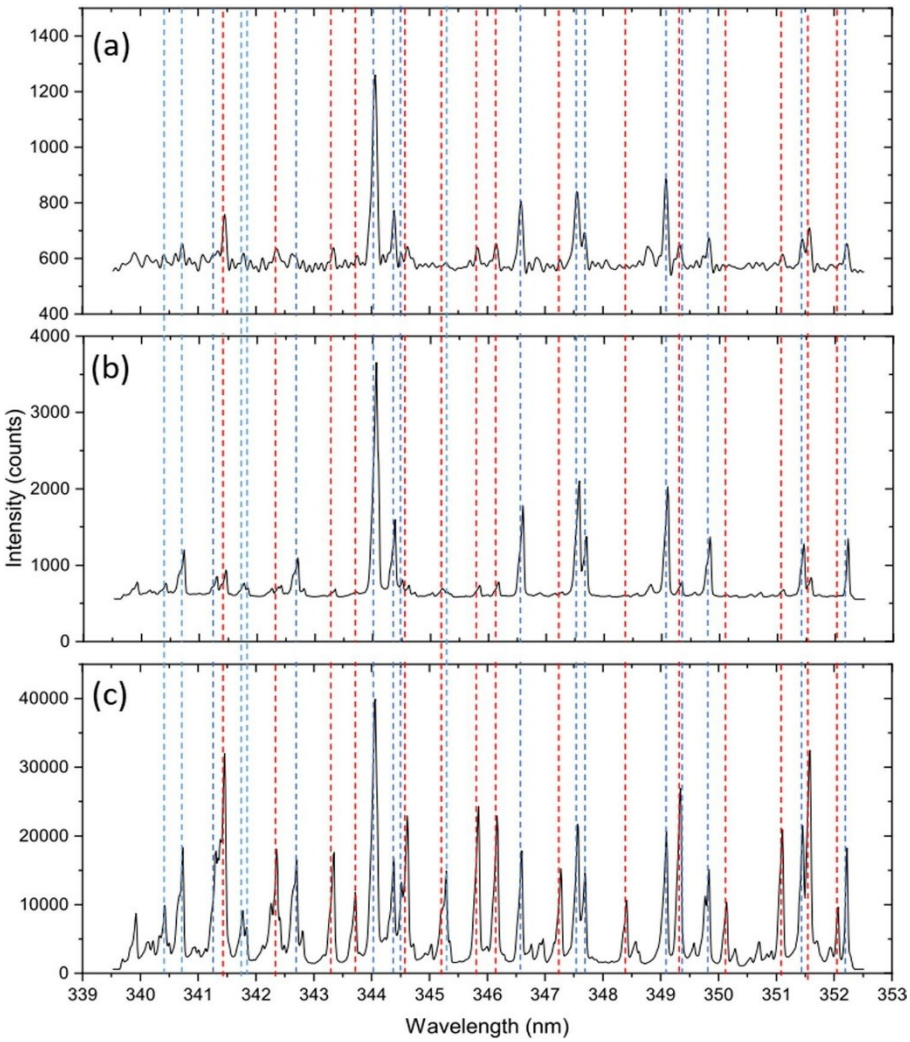

Figure 5-8 **Raw LIBS spectra between 339.5 nm and 352.5 nm for a plagioclase, b amphibole, and c sulfdes for the 1000 laser shot craters. The spectra in (b) and (c) were obtained by averaging 100 spectra around laser shot numbers 500 and 100, respectively, while the spectrum in (a) was obtained by low-pass fltering of shot number 2. Vertical blue and red dashed lines correspond to Fe I lines (except for Fe II 349.35 nm) and Ni I lines, respectively.**

A striking feature of the spectra is the order of magnitude difference between the intensities of the lines in the different phases, which is related to the amount of iron and nickel they contain. The Fe and Ni lines were identified by comparison with the NIST LIBS database [58] with high line resolution for typical plasma parameters (temperature and electron density of 1 eV and 10^{17} cm^{-3}, respectively). All visible lines are Fe I and Ni I lines. The Fe II line at 349.35 nm should be visible but is strongly interfered with by the line at Ni I 349.30 nm.

Since LIBS is based on spectral lines, in Fig 5.9 we consider the total plasma line content as a function of the number of laser shots at the same location. We define the total plasma line content as the area under the spectra after background subtraction. We observe that the line emission in

amphibole and sulfides increases rapidly during the first few laser shots to reach a fairly constant regime after a few laser shots whereas in plagioclase the line emission decreases almost steadily by a factor of almost five between the second (highest line emission) and the last laser shot. After more than 300 shots, the plagioclase spectra are noisy, and no lines can be distinguished. The value of ~ 1 in Fig 5.9 corresponds to random noise above the baseline. The reason for this phenomenon is related to the plateauing of the crater volume, which also occurs beyond the same number of laser shots (Fig 5.7) and is due to the increase of the effective laser interaction area. This effect was also observed in [48]. Considering Fig 5.9, the spectra shown in Fig 5.8 were selected based on the optimal line content in each phase. Averages of 100 spectra were taken for amphiboles (laser shots 451–550) and sulfides (laser shots 51–150) to reduce noise. Such averaging was not possible for plagioclase due to the noisy spectra obtained after the first few laser shots, so the spectrum of laser shot number 2, which has the highest line content as shown in Fig 5.9b, was selected, and the noise was reduced by low-pass filtering at 10 Hz. Figure 5. 9b shows that a first cleaning laser shot increases the line intensity for the second shot.

We used the spectra in Fig 5. 8 to estimate the plasma electron excitation temperature and electron density in the three mineral phases. To determine the plasma electron excitation temperature, we selected Fe I lines with sufficient intensity and spectral resolution. Unfortunately, the Ni I line in our spectral window have very close upper energy levels (between 3.61 and 3.83 eV), making them difficult to use for a Boltzmann plot. The Fe I lines, with their relevant parameters from NIST [59], are listed in Table 5. 4. Note that none of these lines are resonant. The resulting Boltzmann plots are shown in Fig 5.10. The highest electron temperature is obtained in sulfides, intermediate in amphibole, and lowest in plagioclase. This trend is consistent with the amount of ablated material reported in Sect. 5.4.2, since higher amounts of ablated material generally result in lower absorbed energy per electron. The temperatures obtained have values typical of those obtained in other materials for similar laser parameters, for example in an aluminum alloy for a delay of 4 µs [60]. Uncertainties in temperature were evaluated from the quality of the linear regression and from the uncertainties in A_{ki} and line intensity.

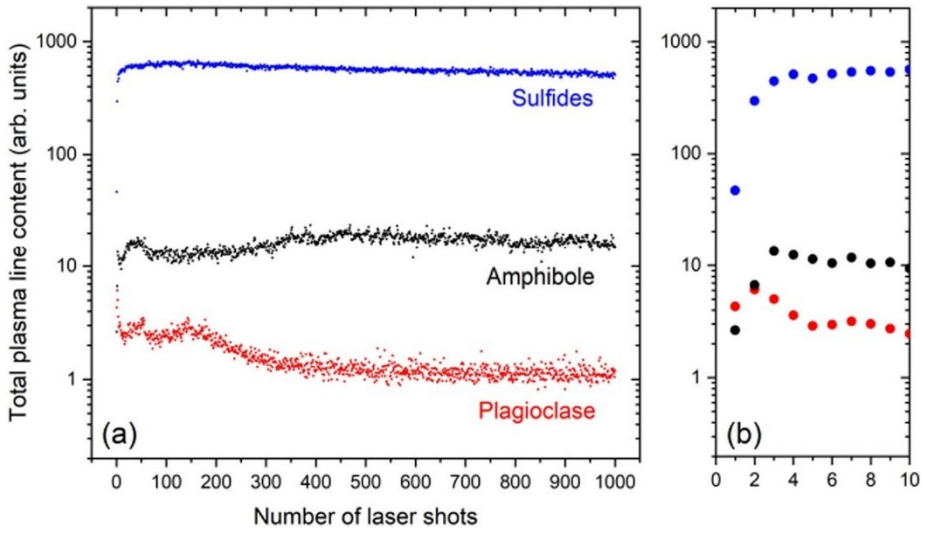

Figure 5-9 **Area under the spectra after background subtraction, highlighting the spectral line content, on a logarithmic scale, for the 1000 laser shot crater in plagioclase, amphibole, and sulfdes. a All 1000 laser shots; b zoom from (a) to show the first 10 laser shots.**

Tableau 5-4 **Fe I lines used for the Boltzmann plots.**

Wavelength λ_{ki} (nm)	Degeneracy × Einstein coefficient $g_k A_{ki}$ (s^{-1}) (accuracy)	Upper energy level E_k (eV)
340.75	5.48×10^8 (10%)	5.81
342.71	4.54×10^8 (10%)	5.79
344.39	2.38×10^7 (10%)	3.69
346.59	3.37×10^7 (10%)	3.69
347.55	4.88×10^7 (10%)	3.65
347.67	1.72×10^7 (10%)	3.69

For the electron density, we used the isolated Ni I line at 346.166 nm (transition from 3.6060 to 0.0254 eV) for which the Stark broadening parameter has been measured [61]. We calculated the electron density from the expression

$$N_e \approx \frac{\Delta\lambda_{FWHM}}{2\Delta\lambda_0}\left(\frac{T_e}{T_{e0}}\right)^{1/2} N_{e0}, \quad \textbf{(5.1)}$$

where $\Delta\lambda 0 = 5 \times 10^{-3}$ nm was measured at $N_{e0} = 6.6 \times 1016$ cm^{-3} and $T_{e0} = 18{,}000$ K for the line of interest. T_e is the temperature shown in Fig. 5. 10. The temperature factor is determined by theoretical considerations [62, 63]. By subtracting three pixels from the measured full width at half maximum of the line of interest ($\Delta\lambda_{FWHM}$) to account for the instrument function, we obtained similar electron densities of $N_e \approx 2.0 \times 10^{17}$, 1.6×10^{17}, and 2.4×10^{17} cm^{-3} for plagioclase, amphibole, and sulfides, respectively. We estimate the uncertainties on $\Delta\lambda_{FWHM}$ to be about

15%. These electron densities are close to the upper range of those obtained from minor element lines in an aluminum alloy using similar laser parameters and for a delay of 4 µs [60].

In order to consider any isolated line in our spectra, we also used Cowley's approximate broadening formula for neutral atoms [63] **to obtain Ne from the measured $\Delta\lambda_{FWHM}$,**

$$\Delta\lambda_{FWHM} \approx 1.54 \times 10^{-25} (n^*)^4 \lambda^2 N_e, \quad \textbf{(5.2)}$$

where λ is the wavelength of the line of interest (in nm) and n^* is the effective quantum number of the upper level. With $(n^*)^2 = 13.59/(I - E_k)$, where I is taken as the first ionization energy (in eV), we obtain for the Ni I 346.166 nm line similar values to those mentioned above, around Ne = 2 × 1017 cm^{-3}, for the three mineral phases. Almost the same values are obtained by considering the isolated Fe I 346.586 nm line (transition from 3.6864 to 0.1101 eV).

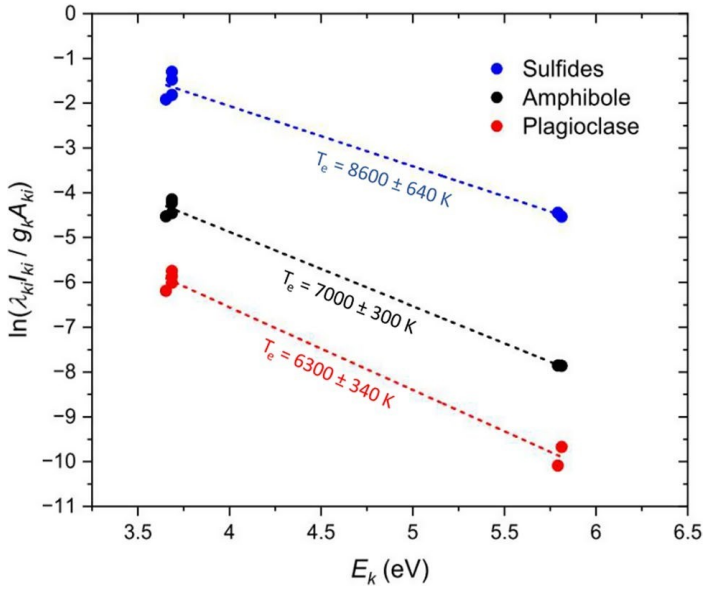

Figure 5-10 Boltzmann plots with corresponding plasma electron temperature T_e for the three mineral phases.

5.5 Conclusions

As LIBS gains popularity as a geochemical analytical technique due to the development of spectral databases and improved instrumentation, it has become pertinent to take a closer look at the effect of the laser on different mineral phases. In this work, we focused on the morphology and volume of laser-induced craters, as well as the plasma properties and emission spectra produced in the three main mineral phases of a palladium ore from the Lac des Iles mine: plagioclase, amphibole, and sulfides. We have shown, for the first time to our knowledge, that the characteristics of craters formed by laser ablation on a given ore sample can vary

considerably from one phase to another for identical laser characteristics. This was made possible in particular by the OCT technique, which allows craters to be imaged in 3D. Since LIBS is a surface analysis technique, it was important to be able to answer the question of how much material is sampled with each laser shot and how this sampling differs from one mineral to another.

Regarding the morphology of the laser-generated craters, we produced a series of four craters in each phase with 50, 250, 500, and 1000 laser shots of 80 mJ each, with a focal spot of 750 µm in diameter. We observed them using SEM and OCT techniques, which provide high-resolution 2D and 3D images of the craters, respectively. The textures revealed by SEM appear as molten and resolidified materials for amphiboles and sulfides, and more uniform and porous for plagioclase, suggesting a different ablation mechanism than for the other two phases. Plagioclase craters are by far the deepest (~ 700 µm per 1000 laser shots vs < 200 µm for the other two phases) and have a truncated cone shape whereas for the other two phases the craters are shallow and generally indeterminate in shape. For plagioclase, the crater volume calculated from the OCT data tends to be constant as the number of laser shots increases due to the decrease in fluence as the laser interacts with the sloping crater walls. For the other two phases (especially sulfides), the evolution of the crater volume as a function of the number of laser shots is not as clear due to their shallow depth. Crater volume does not appear to be directly related to the melting temperature. However, thermal conductivity may be part of the physical interpretation of these observations. Considering the first 50 laser shots, the volume ablated per laser shot can be estimated to be 10^{-4}–10^{-3} mm3 in the three phases for the laser parameters used, while the mass ablated is approximately 1.25 µg for hornblende, 2.71 µg for bytownite, and between 1.68 and 2.00 µg for sulfides.

Regarding the LIBS spectra and the associated plasma properties, we observed that the spectra are dominated by the strongly emitting species iron and nickel, although only traces of nickel are found in the studied sample and traces of iron in the plagioclase. In plagioclase, the spectral line content (integrated spectra with background subtracted) is maximal for the second laser shot. After a few hundred laser shots, the spectra are essentially random noise with no discernible spectral features. In contrast, for the other two phases, the maximum spectral line content is lower for the first laser shots and reaches a relatively stable value after a few laser shots. From these spectra, obtained at times greater than 4 µs, we extracted the plasma electron density and excitation temperature using the iron and nickel lines. The electron densities are

quite similar for all three phases (~ 2×10^{17} cm^{-3}). We obtained a lower electron temperature in plagioclase (~ 6300 K) than in amphibole (~ 7000 K) and sulfides (~ 8600 K).

This study is part of a larger project on the application of LIBS to the measurement of precious metals in rock ores. An extension of this work would be to focus on the variety of pyroxenite from the Lac des Iles ore, which contains a significant amount of phyllosilicate in addition to amphibole, plagioclase, and sulfides.

Acknowledgements We are grateful to Lionnel Djon from Impala Canada for providing us with quarter drill cores from the Lac des Iles mine and their laboratory analysis, as well as for the financial support of Impala Canada. Suzie Côté of the Université Laval is thanked for the operation and data acquisition of both the SEM and the μ-XRF instruments. We also acknowledge the professional work of Guy Lamouche of the National Research Council of Canada (NRC) who carried out the OCT measurements. This work was primarily supported by the National Science and Engineering Research Council of Canada (NSERC) [Grant Number STPGP 521608-18].

Data availability

The data are available from the corresponding author on request.

Declarations

Conflict of interest

The authors declare that they have no known competing financial interests or personal relationships that could have appeared to influence the work reported in this paper.

5.6 REFERENCES

[1] J.D. Winefordner, I.B. Gornushkin, T. Correll, E. Gibb, B.W. Smith, N. Omenetto, Comparing several atomic spectrometric methods to the super stars: special emphasis on laser induced breakdown spectrometry, LIBS, a future super star. J. Anal. At. Spectrom. 19, 1061–1083 (2004)

[2] D.A. Cremers, L.J. Radziemski, Handbook of Laser-Induced Breakdown Spectroscopy, 2nd edn. (John Wiley & Sons, Chich- ester, 2013)

[3] A.W. Miziolek, V. Palleschi, I. Schechter (eds.), Laser Induced Breakdown Spectroscopy (Cambridge University Press, Cam- bridge, 2006)

[4] R.S. Harmon, R.E. Russo, R.R. Hark, Applications of laser- induced breakdown spectroscopy for geochemical and environ- mental analysis: a comprehensive review. Spectrochim. Acta Part B. 87, 11–26 (2013)

[5] R.S. Harmon, C.J.M. Lawley, J. Watts, C.L. Harraden, A.M. Somers, R.R. Hark, Laser-induced breakdown spectroscopy an emerging analytical tool for mineral exploration. Minerals 9, 718 (2019)

[6] R.S. Harmon, G.S. Senesi, Laser-induced breakdown spectros- copy–a geochemical tool for the 21st century. Appl. Geochem. 128, 104929 (2021)

[7] F.F. Fontana, B. van der Hoek, S. Tassios, C. Tiddy, J. Stromb- erg, N. Francis, Y.A. Uvarova, D.G. Lancaster, Laser Induced Breakdown Spectroscopy (LIBS) for whole rock geochemistry. J. Geochem. Explor. 246, 107160 (2023)

[8] C. Fabre, Advances in Laser-Induced Breakdown Spectroscopy analysis for geology: a critical review. Spectrochim. Acta Part B. 166, 105799 (2020)

[9] B. Lemière, R.S. Harmon, XRF LIBS for Field Geology, vol. 20 (Wiley, 2021), pp.1046–1173

[10] G.E. De Benedetto et al., Infrared spectroscopy in the mineralogi- cal characterization of ancient pottery. J. Cult. Herit. 3, 177–186 (2002)

[11] O.V. Borisov, X. Mao, R.E. Russo, Effects of crater development on fractionation and signal intensity during laser ablation induc- tively coupled plasma mass spectrometry. Spectrochim. Acta Part B. 55, 1693–1704 (2000)

[12] B. Nguegang Kamwa, K. Rifai, M. Laflamme, M. Constantin, M. Castello, F. Vidal, P. Bouchard, K. Fytas, A. Blouin and M. Sabsabi, Sampling strategy by statistical analyses of LIBS data in the context of a portable gold analyser, Tenth International Mining Geology Conference, Hobart, Tasmania, 20–22 September 2017.

[13] A. Harhira, P. Bouchard, K. Rifai, J. El Haddad, M. Sabsabi, A. Blouin, M. Laflamme, Advanced Laser-induced breakdown spectroscopy (LIBS) sensor for gold mining. In Proceedings of the Conference of Metallurgists (COM), Vancouver, BC, Canada, 27–30 (2017).

[14] K. Rifai, M. Laflamme, M. Constantin, F. Vidal, M. Sabsabi, A. Blouin, P. Bouchard, K. Fytas, M. Castello, B. NguegangKamwa, Analysis of gold in rock samples using laser-induced breakdown spectroscopy: matrix and heterogeneity effects. Spectrochim. Acta Part B. 134, 33–41 (2017).

[15] I. Elhamdaoui, K. Rifai, J. Iqbal, N. Mohamed, S. Selmani, J. Fer- nandes, P. Bouchard, M. Constantin, M. Laflamme, M. Sabsabi, F. Vidal, Measuring the concentration of gold in ore samples by laser-induced breakdown spectroscopy (LIBS) and comparison with the gravimetry/ atomic absorption techniques. Spectrochim. Acta Part B. 183, 106256 (2021).

[16] S. Selmani, N. Mohamed, I. Elhamdaoui, J. Fernandes, P. Bouchard, M. Constantin, M. Sabsabi, F. Vidal, Laser-induced breakdown spectroscopy analysis of palladium in rock ore. Spec- trochim. Acta Part B. 196, 106523 (2022).

[17] I. Elhamdaoui, N. Mohamed, S. Selmani, P. Bouchard, M. Sab- sabi, M. Constantin, F. Vidal, Rapid quantitative analysis of pal- ladium in ores using Laser-Induced Breakdown Spectroscopy assisted with laser-induced fluorescence (LIBS-LIF). J. Anal. At. Spectrom. 37, 2537 (2022).

[18] K. Rifai, F. Doucet, L. Ozcan, F. Vidal, LIBS core imaging at kHz speed: paving the way for real-time geochemical applications. Spectrochim. Acta Part B. 150, 43–48 (2018).

[19] N. Mohamed, K. Rifai, S. Selmani, M. Constantin, F. Doucet, L. Ozcan, M. Sabsabi, F. Vidal, Chemical and mineralogical mapping of platinum-group element ore samples using laser- induced breakdown spectroscopy and micro-X-ray fluorescence. Geostand. Geoanal. Res. 45, 539–550 (2021).

[20] C. Fabre, D. Devismes, S. Moncayo, F. Pelascini, F. Trichard, Lecomte, B. Bousquet, J. Cauzid, V. Motto-Ros, Elemental imaging by laser-induced breakdown spectroscopy for the geo- logical characterization of minerals. J. Anal. At. Spectrom. 33, 1345–1353 (2018).

[21] K. Kuhn, J.A. Meima, D. Rammlmair, C. Ohlendorf, Chemical mapping of mine waste drill cores with laser-induced break- down spectroscopy (LIBS) and energy dispersive X-ray fluores- cence (EDXRF) for mineral resource exploration. J. Geochem. Explor. 161, 72–84 (2016).

[22] A. Fau, O. Beyssac, M. Gauthier, P.Y. Meslin, A. Cousin, K. Benzerara, S. Bernard, J.C. Boulliard, O. Gasnault, O. Forni, R.C. Wiens, M. Morand, P. Rosier, Y. Garino, S. Pont, S. Mau- rice, Pulsed laser-induced heating of mineral phases: Implica- tions for laser-induced breakdown spectroscopy combined with Raman spectroscopy. Spectrochim. Acta Part B. 160, 105687 (2019).

[23] A.A. Bol'shakov, J.H. Yoo, C. Liu, J.R. Plumer, R.E. Russo, Laser-induced breakdown spectroscopy in industrial and security applications. Appl. Opt. 49, C132 (2010).

[24] D. Bäuerle, Laser Processing and Chemistry, 3rd edn. (Springer, Berlin, 2011).

[25] R.E. Russo, T.W. Suen, A.A. Bol'shakov, J. Yoo, O. Sorkhabi, X. Mao, J. Gonzalez, D. Oropeza, V. Zorba, Laser plasma spectro- chemistry. J. Anal. At. Spectrom. 26, 1596 (2011).

[26] R.E. Russo, X. Mao, J.J. Gonzalez, V. Zorba, J. Yoo, Laser abla- tion in analytical chemistry. Anal. Chem. 85, 6162–6177 (2013).

[27] C. Neff, P. Keresztes Schmidt, P.S. Garofalo, G. Schwarz, D. Günther, Capabilities of automated LA-ICP-TOFMS imaging of geological samples. J. Anal. At. Spectrom. 35, 2255 (2020).

[28] G.C. Dacey, Optical masers in science and technology. Science 135, 3498 (1962).

[29] D.W. Bauerle, Laser Processing and Chemistry (Springer, Berlin, 2011).

[30] T.U. Rahman, Z.U. Rehman, S. Ullah, H. Qayyum, B. Shafique, R. Ali, U. Liaqat, A.H. Dogar, A. Qayyum, Laser-induced plasma- assisted ablation (LIPAA) of glass: effects of the laser fluence on plasma parameters and crater morphology. Opt. Laser Technol. 120, 105768 (2019).

[31] M. Akram, S. Bashir, M.S. Rafique, A. Hayat, K. Mahmood, Laser induced surface morphology of molybdenum correlated with breakdown spectroscopy. Plasma. Chem. Plasma Process. 37, 287–304 (2017).

[32] E. Terasawa, T. Shibuya, D. Satoh, Y. Moriai, H. Ogawa, M. Tanaka, R. Kuroda, Y. Kobayashi, K. Sakaue, M. Washio, Pulse duration dependence of ablation threshold for fused silica in the visible femtosecond regime. Appl. Phys. A 126, 446 (2020)

[33] M.E. Shaheen, J.E. Gagnon, B.J. Fryer, Excimer laser ablation of aluminum: influence of spot size on ablation rate. Laser Phys. 26, 116102 (2016).

[34] H. Mustafa, D.T.A. Matthews, G.R.B.E. Römer, Wavelength dependence of picosecond-pulsed laser ablation of hot-dip gal- vanized steel. Appl. Phys. A 128, 296 (2022).

[35] S.M. Eggins, L.P.J. Kinsley, J.M.G. Shelley, Deposition and ele- ment fractionation processes during atmospheric pressure laser sampling for analysis by ICP-MS. Appl. Surf. Sci. 278, 127–129 (1998)

[36] D.J. Hwang, H. Jeon, C.P. Grigoropoulos, J. Yoo, R.E. Russo, Femtosecond laser ablation induced plasma characteristics from submicron craters in thin metal film. Appl. Phys. Lett. 91, 251118 (2007).

[37] R.E. Russo, X. Mao, H. Liu, J. Gonzalez, S.S. Mao, Laser ablation in analytical chemistry—a review. Talanta 57, 425–451 (2002).

[38] J.J. Gonzalez, A. Fernandez, D. Oropez, X. Mao, R.E. Russo, Femtosecond laser ablation: experimental study of the repetition rate influence on inductively coupled plasma mass spectrometry performance. Spectrochim. Acta Part B. 63, 277–286 (2008)

[39] D. Bigoni, M. Milani, R. Jafer, C. Liberatore, S. Tarazi, L. Antonelli, D. Batani, Influence of mechanical and thermal mate- rial properties on laser-produced crater-morphology and their study by focused ion beam & scanning electron microscope imag- ing. J. Laser Micro/Nanoeng. 5, 169 (2010).

[40] A. Casal, R. Cerrato, M.P. Mateo, G. Nicolas, 3D reconstruction and characterization of laser induced craters by in situ optical microscopy. Appl. Surf. Sci. 374, 271–277 (2016).

[41] V. Grimaudo, P. Moreno-García, A. Cedeño López, A. Riedo, R. Wiesendanger, M. Tulej, C. Gruber, E. Lörtscher, P. Wurz, P. Broekmann, Combining anisotropic etching and PDMS casting for three-dimensional analysis of laser ablation processes. Anal. Chem. 90, 2692–2700 (2018).

[42] D. Monserrat Lopez, V. Grimaudo, G. Prone, A. Flisch, A. Riedo, R. Zboray, T. Lüthi, M. Mayor, M. Fussenegger, P. Broekmann, P. Wurz, E. Lörtscher, Automated, 3-D and sub-micron accurate ablation-volume determination by inverse molding and x-ray com- puted tomography. Adv. Sci. 9, 2200136 (2022).

[43] T. Lippert, Laser application of polymers. Adv Polym Sci 168, 51 (2004)

[44] S. Laville, F. Vidal, T.W. Johnston, O. Barthélemy, M. Chaker, A. Le Drogoff, J. Margot, M. Sabsabi, Fluid modeling of the laser ablation depth as a function of the pulse duration for conductors. Phys. Rev. E. 66, 066415 (2002)

[45] V. Detalle, M. Dufour, J-P Monchalin, M. Sabsabi, L. St-Onge, Method and apparatus for 3-dimensional compositional mapping of heterogeneous materials. Publication date: May 22 (2003). https://worldwide.espacenet.com/patent/search/family/02553 3595/publication/US2003095266A1?q=pn%3DUS2003095266A1. Accessed in Aug 25, 2023.

[46] S. Flude, M. Haschke, M. Storey, Application of benchtop micro- XRF to geological materials. Mineral. Mag. 81, 923–948 (2017)

[47] D. Decharte, C. Perusse, T. Hofton, C. Roney, G. Marrs, S. Taylor, S. Olson, D. Thibodeau, D. Peck and B. Young, Feasibility study for Lac des Iles Mine incorporating underground mining of the Roby Zone. Technical Report, North American Palladium Ltd. 889 (2018)

[48] https://cameo.mfa.org/wiki/Category: Materials_database, Cameo Materials Database. Accessed in Aug 25, 2023.

[49] A. Borisov, H. Palme, Solubilities of noble metals in Fe-contain- ing silicate melts as derived from experiments in Fe-free systems. Am. Miner. 85, 11–12 (2000)

[50] N.L. Bowen, The reaction principle in petrogenesis. J. Geol. 30, 177–198 (1922)

[51] D. Perkins et al., Mineralogy, LibreText geosciences. https://geo. libretexts.org/Bookshelves/Geology/Mineralogy_(Perkins_et_al.). Accessed in Aug 25, 2023.

[52] P.J. Sylvester, A practical guide to platinum-group element analy- sis of sulphides by laser-ablation ICPMS, in Chapter 13. Laser- ablation-ICPMS in the earth sciences. Principles and applica- tions. ed. by P. Sylvester (Mineralogical Association of Canada, Ottawa, 2001).

[53] G. Kullerud, Thermal stability of pentlandite. Can. Mineral. 7(3), 353–366 (1963)

[54] S.E. Gilbert, L.V. Danyushevsky, K. Goemann, D. Death, Frac- tionation of sulphur relative to iron during laser ablation-ICP-MS analyses of sulphide minerals: implications for quantification. J. Anal. At Spectrom. 29, 1024–1033 (2014).

[55] K. Amponsah-Manager, N. Omenetto, B.W. Smith, I.B. Gor- nushkin, J.D. Winefordner, Microchip laser ablation of metals: investigation of the ablation process in view of its application to laser-induced breakdown spectroscopy. J. Anal. At. Spectrom. 20, 544–551 (2005).

[56] G. Dalla Santa, A. Galgaro, R. Sassi, M. Cultrera, P. Scotton, J. Mueller, D. Bertermann, D. Mendrinos, R. Pasquali, R. Perego, S. Pera, E. Di Sipio, G. Cassiani, M. De Carli, A. Bernardi, An updated ground thermal properties database for GSHP applica- tions. Geothermics 85, 101758 (2020).

[57] E.H. Braye, A.H. Sehon, B.B. Darwent, Thermal decomposition of sulfides. J. Am. Chem. Soc. 77, 5282–5285 (1955)

[58] https://physics.nist.gov/PhysRefData/ASD/LIBS/libs-form.html for Nist LIBS Database. Accessed in August 25, 2023.

[59] https://physics.nist.gov/PhysRefData/ASD/lines_form.html for Atomic Spectra Database. Accessed in August 25, 2023.

[60] V. Detalle, R. Héon, M. Sabsabi, L. St-Onge, An evaluation of a commercial Echelle spectrometer with intensified charge-coupled device detector for materials analysis by laser-induced plasma spectroscopy. Spectrochim. Acta Part B. 56, 1011–1025 (2001).

[61] N. Konjevic, A. Lesage, J.R. Fuhr, W.L. Wiese, Experimental stark widths and shifts for spectral lines of neutral and ionized atoms (A Critical Review of Selected Data for the Period 1989 Through 2000). J. Phys. Chem. Ref. Data. 31, 819 (2002).

[62] M.C. Artu, Parametric estimates of line broadening due to quad- ratic or linear Stark effect, Spectroscopic challenges in photoion- ized plasmas. ASP Conf. Ser. 246, 155 (2001).

[63] C.R. Cowley, An approximate Stark broadening formula for use in spectrum synthesis. The Observatory. 91, 139–140 (1971).

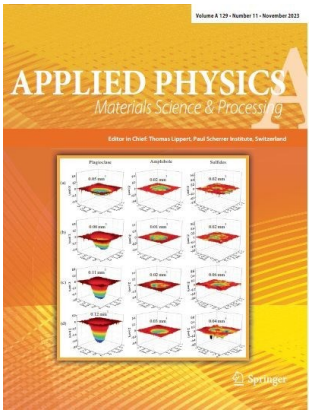

Applied Physics A - your paper for the November Editor's Choice Article Highlights

---

À partir de Cindy Zitter <cindy.zitter@springer.com>
Date Mar 28/11/2023 10:24
À Selmani, Samira <Samira.Selmani@inrs.ca>; Vidal, Francois <Francois.Vidal@inrs.ca>
Cc Fábio Santos <fabio.p.santos@springernature.com>; Lippert Thomas (PSI) <thomas.lippert@psi.ch>

Dear corresponding authors,

Every month 1 or 2 papers are chosen as an Editor's Choice. On behalf of the Editor-in-Chief of *Applied Physics A*, we would like to congratulate you as your paper was chosen for this month's Editor's Choice. You can find the announcement on the journal's update page:

https://www.springer.com/journal/339/updates/17188234

as well as tweeted and posted on our @SpringerPhysics accounts
https://twitter.com/SpringerPhysics/status/1729521389772718579
https://www.facebook.com/photo/?fbid=831357785666932&set=a.381411803994868

We would be happy if you use these to send to colleagues and distribute further to your network!

Again our congratulations and we would be happy to receive future papers!

Best regards,

Cindy Zitter

--
Mrs. Cindy Zitter

Assistant Publisher
Physics
Working everyday except Monday afternoons
--
Springer Nature Group
Van Godewijckstraat 30, 3311 GX Dordrecht, The Netherlands
Cindy.Zitter@springernature.com
www.Springer.com

CHAPITRES VI

6 ARTICLE 3 - LASER-INDUCED BREAKDOWN SPECTROSCOPY (LIBS) IN THE FIELD: HOW ROCK MOISTURE INFLUENCES SPECTRAL QUALITY AND PLASMA PROPERTIES

Spectroscopie de plasma induit par laser (LIBS) sur le terrain: Influence de l'humidité de la roche sur la qualité spectrale et les propriétés du plasma

Laser-Induced Breakdown Spectroscopy (LIBS) in the Field: How Rock Moisture Influences Spectral Quality and Plasma Properties

Auteurs :

Samira Selmani[1], Ismail Elhamdaoui[1], Paul Bouchard[3], Marc Constantin[2], Mohamad Sabsabi[3] , François Vidal[1]

[1]Institut National de la Recherche Scientifique, Centre ´énergie matériaux télécommunications, 1650 Lionel-Boulet blvd, Varennes, QC J3X 1P7, Canada

[2] Département de Géologie et de Génie Géologique, Université Laval, 1065 Avenue de la Médecine, Québec, QC G1V 0A6, Canada

[3] National Research Council of Canada, 75 de Mortagne Blvd., Boucherville, QC J4B 6Y4, Canada

Titre de la revue ou de l'ouvrage : Atomic Spectroscopy

Contribution des auteurs :

Dans cet article, chaque auteur a apporté une contribution essentielle et complémentaire pour atteindre les objectifs de l'étude.

Samira Selmani en tant que première auteure, a sélectionné l'échantillon, pris les mesures LIBS et les mesures de l'humidité. Elle a analysé, interprété les données, rédigé le manuscrit et effectué les corrections et révisions nécessaires pour finaliser l'article, avec une aide particulière de François Vidal.

François Vidal a apporté des remarques pertinentes et des interprétations précieuses qui ont considérablement amélioré l'article. Il a également joué un rôle important dans l'amélioration de

la qualité de la rédaction, offrant des explications claires. Il a supervisé la correction et la révision de l'article.

Marc Constantin a validé l'interprétation de la partie minéralogique des roches, en apportant des remarques pertinentes basées sur l'analyse au microscope électronique à balayage (SEM) et la micro-XRF.

Mohamad Sabsabi a aidé à valider les résultats et les interprétations obtenus par LIBS (Spectroscopie de plasma induit par laser).

Paul Bouchard a aidé à préparer le montage LIBS ainsi que les paramètres. Il a également apporté des conseils pertinents qui ont contribué à la précision des mesures et des analyses.

Ismail Hamdaoui a contribué à l'amélioration du contenu de l'article grâce à ses remarques constructives.

François Vidal, Marc Constantin et Mohamad Sabsabi ont supervisé l'article dans son ensemble.

Tous les coauteurs ont offert leur soutien pour la rédaction et ont contribué à la révision du manuscrit.

Chacun de ces contributeurs a joué un rôle clé dans le succès de cet article, permettant une analyse complète et rigoureuse de l’échantillon de minerai, et assurant la robustesse et la validité des conclusions tirées.

6.1 ABSTRACT

Before LIBS can be applied to analysis at mine sites under normal weather conditions, a number of practical issues need to be addressed. One of these is the moisture content of rock samples taken directly in the field. To assess the effect of rock moisture content on LIBS measurements, we studied its temporal evolution as the rock dried under ambient laboratory conditions using a series of 1080 laser shots (18 rows × 60 columns) at 2 Hz (8 ns pulse duration, 1064 nm wavelength, with a fluence of ~4 kJ cm^{-2}). At maximum moisture, the LIBS spectra are weak, with only a few strong lines emerging from the background noise, while a richer spectrum appears as the rock dries. Color maps of LIBS spectra averaged over wavelength (white light) from the rock surface and net Hα line intensity from the water layer form complex, weakly correlated mosaics whose components depend on local rock properties (e.g., composition, porosity, asperities). However, the time evolution of their average over each of the 18 rows correlates well with that of the rock weight and microwave moisture measurements. Using the Hα line broadening and the ratio between the Mg II 280.27 nm and Mg I 285.21 nm line, the space and time averaged plasma produced in both the dry and wet rock areas is characterized by an electron number density in the range of 10^{17} cm^{-3} and an ionization temperature close to 1 eV. The physical mechanisms involved are discussed. This study highlights the importance of controlling the moisture of the rock at the mining site before starting LIBS measurements, as it has a significant impact on the accuracy of the results obtained.

Keywords: LIBS measurement, rock moisture, rock drying, spectral line intensity, plasma temperature

6.2 Introduction

The mining industry is actively seeking new, cost-effective technologies. Among these is the ability to measure the concentration of chemical elements of high commercial value, such as precious metals, in real time and in the field during various phases of exploration and mine production.[1] Several techniques are commonly used for precious or base metal concentration measurements. These include inductively coupled plasma optical emission spectroscopy (ICP-OES),[2] atomic absorption spectroscopy (AAS),[3] and X-ray fluorescence (XRF).[4] All of these techniques are laboratory-based and tend to be costly, time-consuming, labor-intensive, and require extensive sample preparation. An exception is XRF in a portable configuration. However, it falls short in the quantification of precious metals due to its limited sensitivity and high limit of detection.[5,6] Infrared spectroscopy, on the other hand, can determine the mineralogy of rock samples, but generally lacks the ability to provide information on their elemental composition,[7] although recent advances are beginning to fill this gap.[8]

LIBS appears to be a promising candidate to meet the demands of real-time analysis while complementing conventional techniques already in use. LIBS is an optical analytical technique based on emission spectroscopy that uses a laser beam focused on the sample (solid, liquid or gas) to atomize a small fraction of the surface and create a plasma. The light emitted by the plasma is then collected and spectrally analyzed to determine the chemical composition of the sample. Reference materials of similar chemical composition to the samples being analyzed are used to calibrate the LIBS signal, i.e. to establish a relationship between the intensities of the spectral lines and the content of the element of interest.[9] The main advantage of LIBS for the mining industry over conventional analytical techniques is its ability to analyze any element of the periodic table in samples in the field with little or no sample preparation.[10] LIBS has already found applications in several industries and is being considered for mineral processing.[11] The use of LIBS in mineralogy has received considerable attention. Several reviews are available on the applications of LIBS in the analysis of geological and environmental materials.[12-15]

The promising results obtained with respect to the potential application of LIBS in mining for the rapid evaluation and on-site determination of precious metal concentrations in solid rock samples, such as drill cores, require careful consideration of a number of practical issues. One of these is the amount of moisture contained in the rock being analyzed, which can be highly variable in the mining environment. In practical scenarios and real-time analysis, samples in the mining environment may become wet due to rain or exposure to water. This raises the question: How are LIBS measurements affected by moisture content and how can we account for this in the

measurements? The main objective of this study is to investigate the effect of moisture present in the rock on LIBS measurements. For this study, we specifically consider a solid ore sample from the Lac des Iles (LDI) palladium mine, located 127 km north of Thunder Bay, Ontario, Canada, as these samples have been thoroughly characterized in our previous work.[9,16-19] This paper presents experimental results on the evolution of LIBS measurements and plasma properties of a drying rock sample under normal laboratory conditions. We scanned a flat surface of the rock as an 18 × 60 matrix of laser shots at 2 Hz and monitored the evolution of the spectra averaged over wavelengths (hereafter called white light) as well as the intensity of the Hα line, which used as an indicator of the presence of water. We calculated the correlation between these two pieces of information and determined the plasma properties from the spectral data in both the wet and dry areas of the rock.

6.3 Experimental

6.3.1 The rock fragment

The rock sample used in this study is a 32.1 g dry weight prismatic mineralized core fragment from the LDI palladium mine. The sample is of gabbronorite type and is from the Mine Block Intrusion area.[20] Ore from this area is characterized by locally high silicate (amphibole and plagioclase) and sulfide contents, which appear as domains of a few mm^2 randomly distributed over the surface, as determined from our micro-XRF and LIBS measurements on various samples.[16,18] A photograph of the sample after laser scanning is shown in Fig. 6a.b shows the mirror side of the rounded cut surface. The sample is a piece of a quarter core (cut longitudinally) where the rounded surface has been cut to a flat surface measuring approximately 6 cm × 2.5 cm. This surface was used for our LIBS measurements. The composition of the half of the original core, as determined by conventional analytical methods, is shown in Table 1.

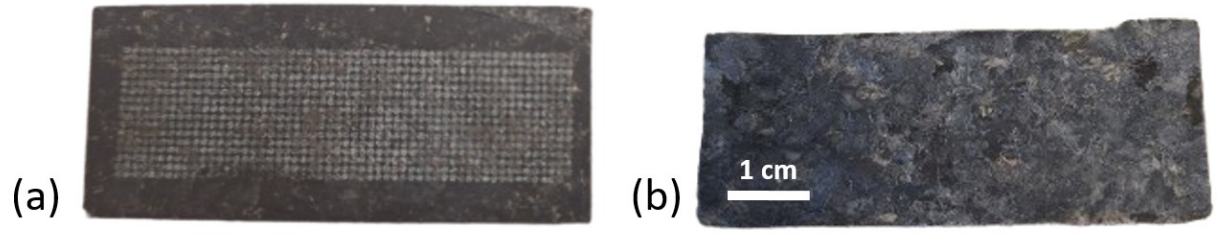

Figure 6-1 **Photographs of the Lac des Iles mine core fragment used in this study. (a) Laser-scanned surface over an 18×60 matrix with 0.95 mm between laser shots. (b) Surface of the cut rounded side of the core corresponding to the scanned surface.**

Tableau 6-1 **Partial chemical composition in % of the Lac des Iles 1 m long half core used in this study**

Si	Ca	Fe	S	Cu	Ni	Al	Mg
24.2	6.6	4.7	0.35	0.14	0.31	7.7	7.8

6.3.2 Sample wetting and moisture measurement

Fig. 6.2 illustrates the experimental protocol used to wet the sample and measure its moisture content. The sample was completely submerged in a beaker of water and left in the water for a week, during which time the rock became water saturated. We found that a few days was not long enough for the rock to become fully saturated with water. At the end of the immersion period, the rock was drained and moisture measurements were taken by gravimetry using an analytical balance (Cole-Parmer Symmetry PA-220, 220 G × 0.0001 g) or an industrial moisture meter (Mastercraft Battery Powered Digital Pinless Moisture Meter) at regular 30-second intervals until the readings remained unchanged. Measurements were made under laboratory air conditions between 23 and 25°C, with controlled humidity close to 40%. All these measurements were repeated three times under the same working conditions and parameters. The moisture meter measurements were taken on the 6 cm × 2.5 cm flat surface of the rock sample. These measurements are based on the dielectric constant of the material using an RF field under the 2 cm × 2 cm sensor pad in contact with the sample. This instrument was used to demonstrate that rapid and reliable moisture measurements could be achieved.

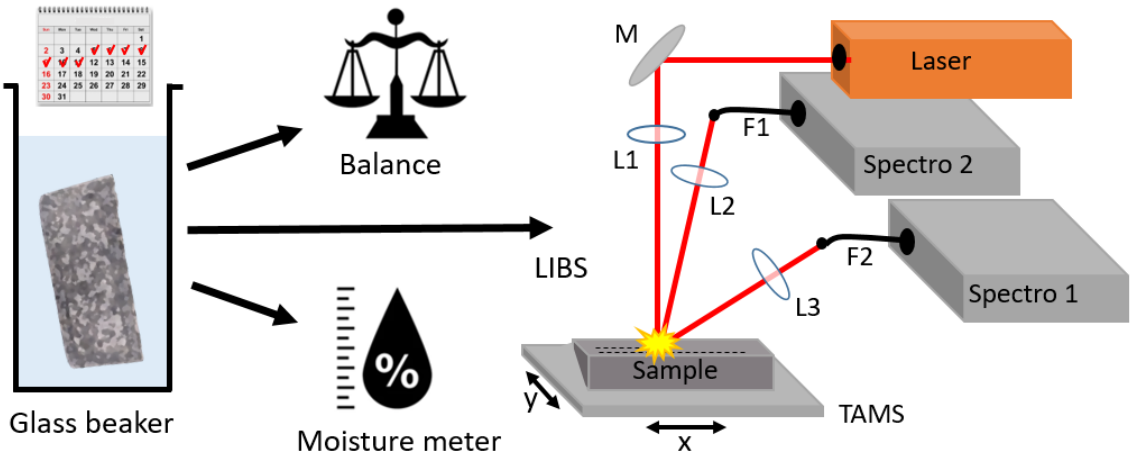

Figure 6-2 **Methods used to measure the time dependence of the moisture content of a rock sample and its influence on the LIBS spectra. The sample is removed from a beaker filled with water after 1 week and then either weighed, or probed with a moisture meter, or scanned with a LIBS system where a laser beam creates a plasma on the sample and the light emitted by the plasma is collected by two spectrometers in different spectral ranges. M: mirror, TAMS: three-axis motorised stage, F1 and F2: fibre optics bundles, L1, L2 and L3: lenses.**

6.3.3 LIBS measurements

LIBS measurements were performed on the 6 cm × 2.5 cm flat surface of the rock sample, starting 30 seconds after the sample was removed from the beaker, during which time the sample was drained and placed on the motorized sample holder. The LIBS measurements consisted of 60 laser shots on 18 horizontal lines (Fig. 6.1), one shot per position on the wet rock surface (30 seconds per line at 2 Hz) with a 0.95 mm step between two laser shots. A new series of 60 shots was automatically started in the same direction at the end of the previous scan. The LIBS measurements were then correlated in time with the moisture measurements made by gravimetry and the moisture meter.

The experimental configuration for performing the LIBS analysis is shown schematically in Fig. 6.2. A Nd:YAG laser system (Quantum Light Instruments, model Q2HE-E50-1064-AT1) was used for plasma generation. This laser is capable of delivering pulses with energies up to 70 mJ and an adjustable repetition rate up to 50 Hz. It operates at a fundamental wavelength of 1064 nm and exhibits a laser pulse time profile with a full width at half maximum (FWHM) of 5.8 ns. The spectroscopic measurements were performed with two spectrometers (Avantes, model ULS2048CL-EVO) covering the wavelength range 200 to 447 nm with a 3-pixel resolution between 270 and 380 pm and the range 425 to 920 nm with a 3-pixel resolution of 700 pm. Both are equipped with a gated CMOS detector (Hamamatsu S11639, 2048 pixels, 14×200 µm).

To generate the plasma, the laser beam was focused on the surface of the sample using a 175 mm focal length lens. The sample was mounted on a three-axis motorized stage (Zaber, model X-ASR100B120B-SD12) controlled by an on-board programmable controller. The sample surface was carefully positioned in the same plane as the stage, perpendicular to the laser beam. The plasma emission was directed onto the circular input ends of the fiber bundles using a 50 mm focal length lens. The aligned outputs of the fiber bundles were positioned in front of the 25 µm entrance slit of the spectrometers to ensure compatibility with the pixel matrix of the detector.

Each laser pulse had an energy of $E_L = 65$ mJ, and the 4σ diameter of the laser spot on the target was $D = 65\ \mu$m, corresponding to a fluence of approximately $8E_L/\pi D^2 \approx 4$ kJ cm-2.21 A delay of 1 µs after the laser pulse before starting the signal integration was implemented, together with a gate width of ms for the signal integration time. Such a high fluence was chosen in order to observe as much of the LIBS signal from the rock surface as possible, since the water layer can attenuate the signal considerably, as we will see.

6.4 Results and discussion

6.4.1 Temporal evolution of the rock moisture

The evolution of the moisture content of the wet rock, given by the balance and the moisture meter, is shown in Figs. 3a and 3b, respectively. Note that the moisture content shown in Fig. 6.3b is only a relative indication, as the moisture meter was not specifically calibrated for our type of sample. Measurements were taken by both instruments twice per minute, with each measurement lasting a few seconds. Prior to the first measurement, the sample was removed from the beaker and shaken briefly to remove excess water. After one week of incubation in water, the weight of the rock increased from 31.1 g to 32.9 g due to water absorption in its pores and capillaries. Then, when removed from the beaker, the weight of the rock decreased due to natural evaporation of the water it contained until it reached stability in about 6 minutes.

The linear decrease in water content observed in Fig. 6.3 is consistent with the general description of the drying process of capillary porous media. Drying is a combination of internal transfer within the porous medium and external transfer to the surface where evaporation takes place. As first introduced by Krischer, drying of capillary porous media is described by three main steps. During the first stage, the evaporation rate is approximately constant. This constancy is explained by the capillary effect, which efficiently drains water to the surface, keeping the surface wet enough to compensate for evaporation. After a critical stage where the capillary effect can no longer keep the surface sufficiently wet due to the depletion of moisture below the surface, the drying rate gradually decreases. The final stage is characterized by an internal evaporation front that retreats into the porous medium, leaving a dry zone on the surface.

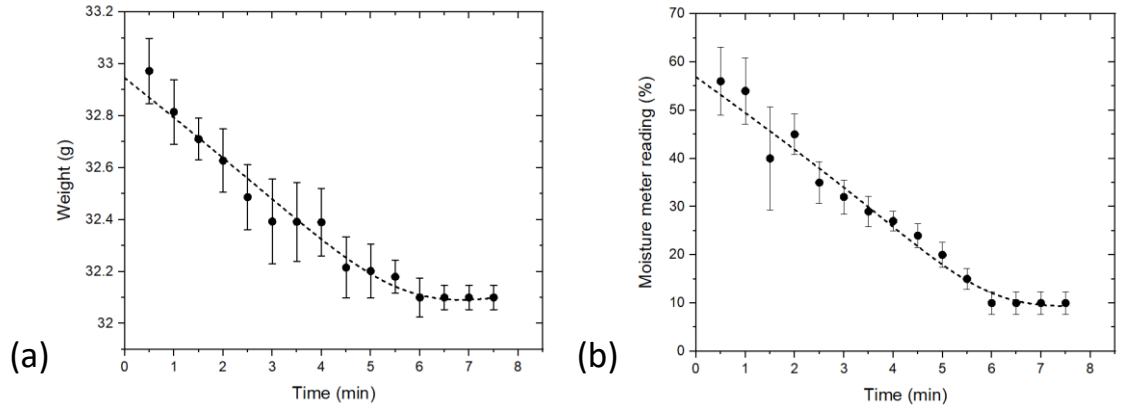

Figure 6-3 **Variation of the moisture content of the rock sample. (a) Weight and (b) uncalibrated moisture content as a function of time, as given by the balance and moisture meter (set to concrete material), respectively. The error bars are the result of 3 measurements taken 3 weeks apart. The dashed curves are fits for guidance.**

The moisture content of the rock samples at saturation was 2.5 wt%. However, this simple definition of moisture content depends only on volume, whereas it should depend more on surface area for low porosity rocks where moisture is confined near the surface, as is likely to be the case for the dense rock sample tested. We estimate the surface area of our sample to be ~40 cm^2, so the rock moisture at saturation is equivalent to covering the entire surface with a layer of ~200 μm of water. This latter value is expected to be quite similar for ore samples of the same type of different size and shape, as long as the size of the rock is greater than the moisture layer filling the pores and capillaries below the surface.

6.4.2 Temporal evolution of the LIBS spectra

To determine the behavior of the LIBS signal during the drying process, the 6 cm × 2.5 cm surface of the sample was scanned with laser shots, forming a matrix of 18 rows × 60 columns, for a total of 1080 measurements, as shown by the laser imprints in Fig.6 1. The laser started at the lower left corner of the surface (coordinates (1,1)) and scanned each row from left to right, always starting with the leftmost column after a rapid movement of the motorized stage.

Fig. 6.4a shows a map of the net Hα (H I 656.3 nm) line intensity (peak height minus background), which was expected to be indicative of the local water content. Spectra containing the Hα line are discussed in a subsequent section. In this map, the red color indicates higher emission and the blue color indicates lower emission. Unexpectedly, the intensity of the Hα line shows a large variance in all parts of the map. At the earlier times (lower part of the map), red pixels are mixed with dark blue ones, and at the latest times (upper part of the map), blue pixels are mixed with white and even reddish pixels. The large data scatter can be attributed to several factors, including local differences in porosity and composition, as well as small asperities on the rock surface. Porosity obviously affects water retention, while asperities can drive water into lower adjacent areas, leaving a drier area at the top. Since the sample under investigation was not polished (as in practical situations), the latter effect could occur even though the surface of our samples appeared quite flat to the naked eye and touch. In the present case, the local mineral composition may also affect the Hα line intensity, as hornblende and actinolite are hydrated minerals known to occur in the gabbronorite LDI ore.[16] The general wetting trend can be seen more clearly in Fig.6. 4b, which shows the average of the Hα line intensity over the 60 positions of each row. As suggested by the dashed line, the Hα line intensity appears to follow a linear trend for approximately the first 5 minutes (10th row) or so and then becomes constant on average, which

is quite consistent with the trend obtained from the weight and moisture meter measurements as a function of time shown in Fig. 6.3.

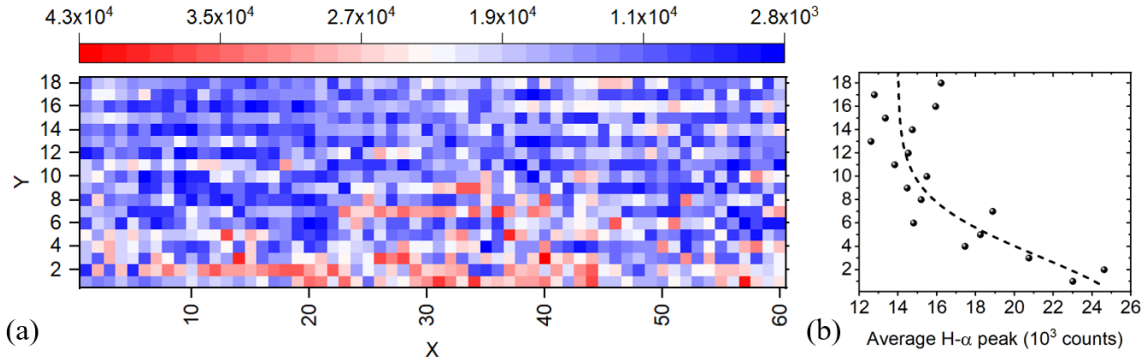

Figure 6-4 **Peak of the H-α line of the drying rock surface. (a) At each laser shot location in the 18 row × 60 column matrix. Each row is scanned from column 1, starting at (1,1). The scale is in counts. (b) Averaged over each row. The dashed curve shows the overall trend.**

The LIBS signal at each position was also characterized by averaging the spectra taken at each of the 1080 positions between 425 and 920 nm over 2048 wavelengths, the result hereafter referred to as the white light emission. A map of the white light emission at each of the 1080 scanned positions on the sample is shown in Fig. 6.5a. Note that several lines of the spectra corresponding to the reddish pixels saturate the CMOS camera (> 2^{16} counts), so the white light emission may be slightly underestimated in these cases. However, the largest average emission (~10^4 counts) observed in Fig. 6.5a is still much smaller than the saturation threshold. The map generated by the white light emission in the 200-447 nm range (not shown here) from the second spectrometer is almost identical to Fig. 6.5a, except that it is scaled down by a factor of about 2. In fact, we found a correlation of 0.96 between the 1080 pixels of the two maps. Typical spectra in this wavelength range are discussed in in a subsequent section.

It can be seen in Fig. 6.5a that the blue color dominates in the lower part of the map, corresponding to the early stage of the laser scanning (wetter surface), while the red color dominates in the upper part of the map, corresponding to the later stage of the laser scanning (drier surface). However, the details are very complex. This complexity is due to the same factors discussed above for the Hα line intensity. The explanation for the large reddish trace around column 48 in the lower blue area is unclear at this stage. It could be due to a slight unevenness, not visible or perceptible by touch, caused by imperfect sawing of the rounded part of the core along the x-axis. Even for dry rocks, significant differences in local plasma emission are expected depending on the mineral phase. In a previous paper, we showed that the three main mineralogical phases of similar LDI ore samples produce plasma emission of different amplitudes according to the relationship:

plagioclase < amphibole < sulfide.[18] In a typical LDI ore, such as the sample studied here, these mineral phases are randomly distributed and form areas of variable size, as shown by our XRF analyses.[16]

The general trend over time can be seen more clearly in Fig.6. 5b, which shows the average white light emission over the 60 positions of each row. It can be seen that the white light emission is low and fairly uniform for about the first 5 minutes (10th row) and then starts to increase. There is some periodicity in the area of low emission, which is attributed to asperities caused by the sawing process. Consistent with the weight and moisture measurements in Fig. 6.3 and the Hα line intensity in Fig. 6.4b, the white light emission shows an inflection point between a low emission area and a higher emission area around the 12th row (6 minutes).

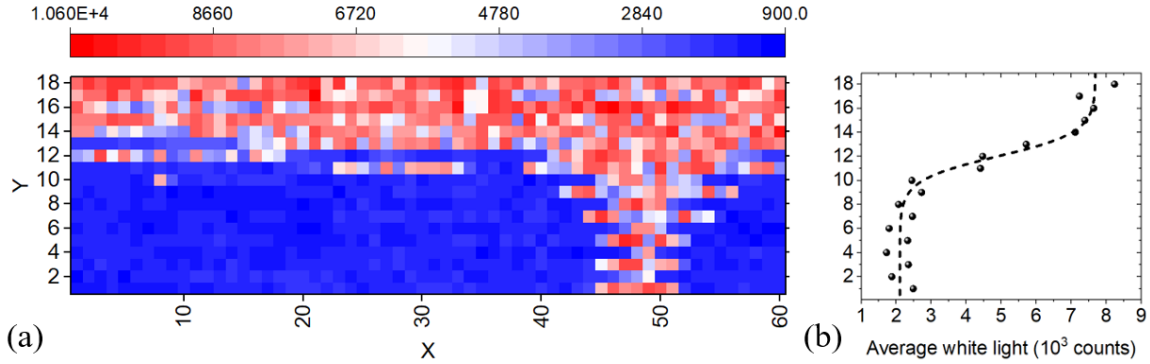

Figure 6-5 **White light emission in the spectral window 425-920 nm from the drying rock surface. (a) At each laser shot location in the 18 row × 60 column matrix. Each row is scanned from column 1, starting at (1,1). The scale is in counts. (b) Averaged over each row. The dashed curve shows the overall trend.**

We calculated the correlation coefficient between the data in Figs. 6.4a and 5a to identify relationships between white light emission and Hα line intensity. The pixel-to-pixel correlation coefficient between the two maps was found to be -0.2, indicating a low overall anticorrelation. However, more telling results are obtained from the correlation between the pixels of the same rows of the two maps. The result is shown in Fig. 6.6. It can be seen that there is no clear trend for the rows between 1 and 13, as the correlation coefficient is scattered between about -0.3 and +0.3. However, there is a significant correlation of about +0.8 for rows 14 to 17 and +0.6 for row 18, which means that there is a near proportionality between white light emission and Hα line intensity for these rows. These correspond exactly to the highest average white light emission as shown in Fig. 6.5b. This analysis suggests that for the wetter part of the rock, the emission from the rock constituents, which is mainly responsible for the white light emission (see next section), depends strongly on the local water content, which is rather random as it depends on the local

rock properties as discussed above. However, for the drier part of the rock, the Hα line intensity is mainly determined by the rock constituents.

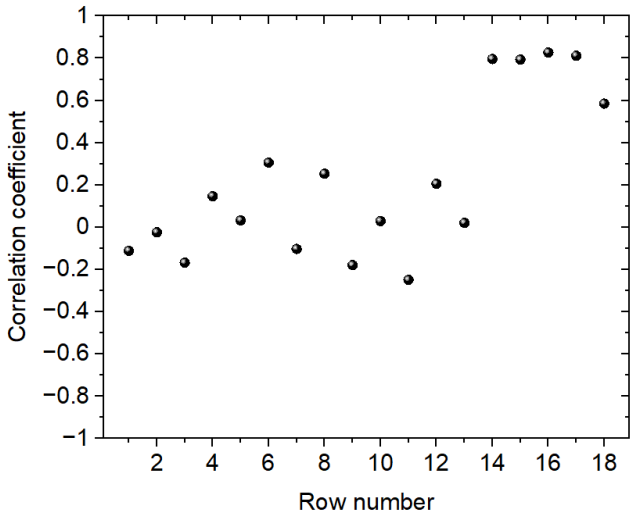

Figure 6-6 **Correlation coefficients between the 60 values of each row of the maps of Figs. 6.4 and 6.5.**

Two general conclusions can be drawn from this section. First, the white light emission, which comes mainly from the rock constituents, is significantly attenuated by the presence of water on the rock surface. Second, the white light emission does not correlate with the Hα line intensity unless the rock is almost dry, which happens after about 7 minutes in our case.

6.4.3 Plasma properties

In this and the next section, we attempt to understand the effect of water on the plasma properties by determining the electron temperature and number density in the wet and dry rock regions. Typical spectra in the wetter region collected by the pair of spectrometers are shown in Fig. 6.7 for low and high white light emission, specifically for pixels with coordinates (1,44) and (1,50), respectively, with reference to Figs. 6.4a and 6.5a. Despite the overall weakness of the spectra in the low white light emission regions, some features can be identified, as shown in Fig. 6.7a, in particular Mg lines around 280 nm, which are used to determine the plasma ionization temperature. Fig. 6.7b shows the spectrum at the same position with the Hα line, which is used to determine the electron number density. Several lines saturate the camera for the high white light emission shown in Figs. 6.7c and 7d, but not the Hα and Mg lines around 280 nm. It is clear from Fig. 6.7d that the high white-

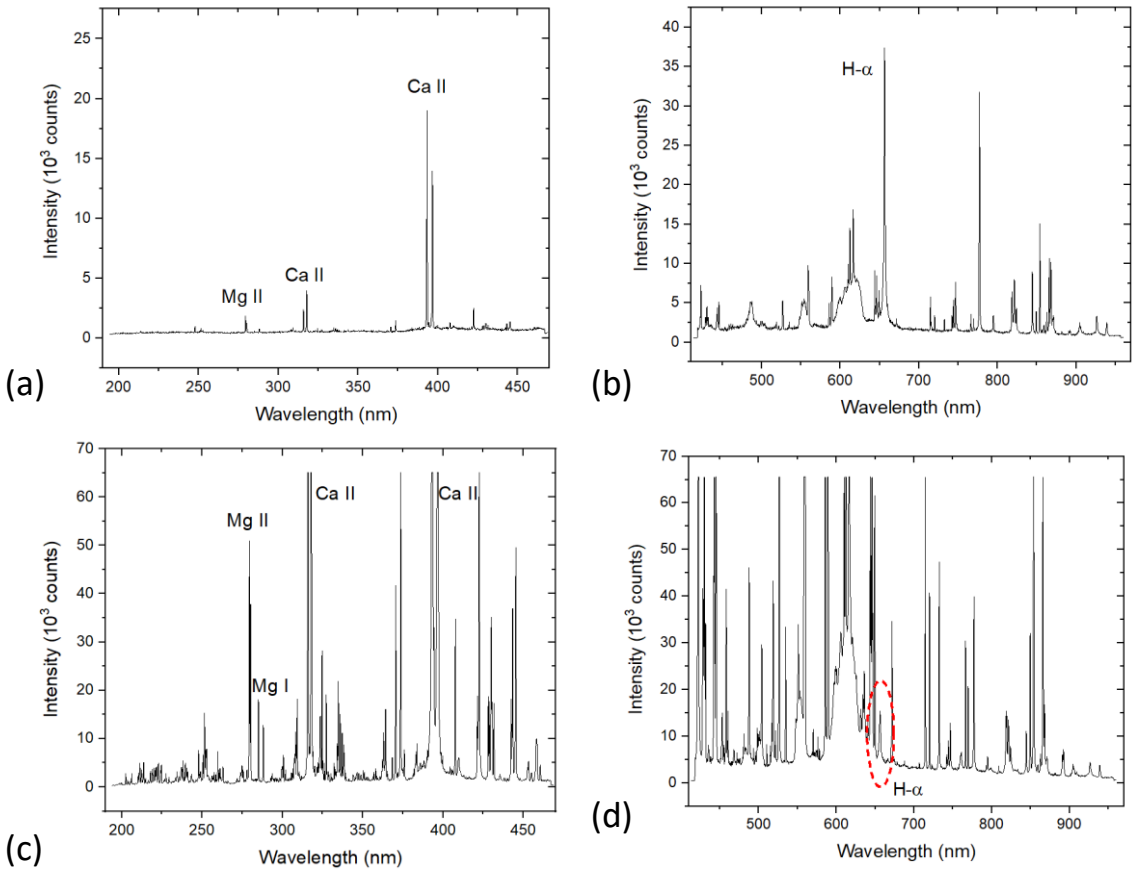

Figure 6-7 **Examples of raw spectra of the scanning matrix for pixels (1,44) and (1,50) with reference to Figures 4a and 5a. (a) and (b) in an area of low white light emission (pixel (1,44)); (c) and (d) in an area of high white light emission (pixel (1,50)). In the latter cases, several lines saturate the camera. The lines identified are Mg II 279.55 nm, Mg II 280.27 nm, Mg I 285.21 nm, Ca II 315.89 nm, Ca II 317.93 nm, Ca II 393.37 nm, Ca II 396.84 nm and H 656.28 nm (highlighted by the red dashed ellipse in (d)).**

Magnifications of the useful Mg and Hα lines in the spectra from Figs. 6.7a and 6.7b are shown in Fig. 6.8. Note the relatively noisy background in Fig. 6.7a. Pixel (1,44) was selected because the Mg I 285.21 nm line was sufficiently above the noise to be used, which was not the case for all pixels in the lower blue region of the map in Fig. 6.5a. In addition, the Hα line was particularly intense for this pixel, suggesting a significant effect of water at this location.

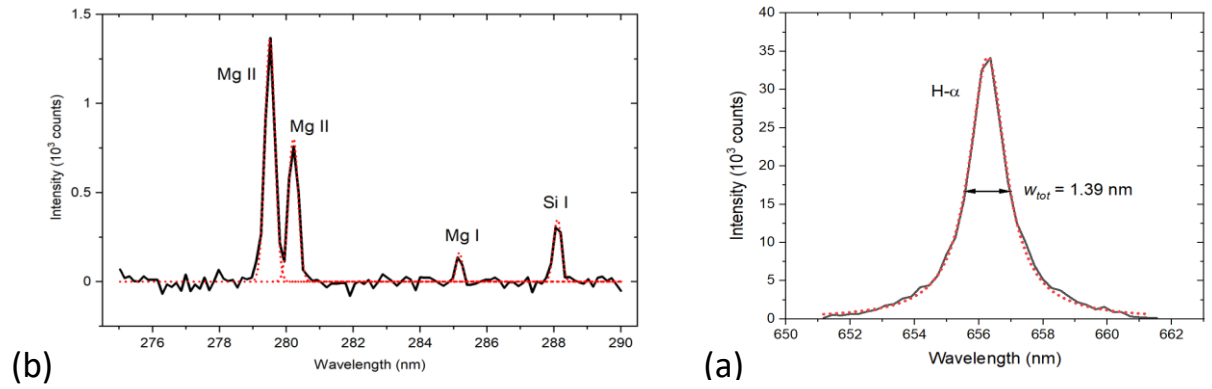

Figure 6-8 **Spectral lines used to estimate plasma properties in the low white light emission region, here for pixel (1,44). Black lines: measured spectra with baseline subtracted; red dotted lines: peak fits. (a) Mg II 279.55 nm, Mg II 280.27 nm and Mg I 285.21 nm; (b) H 656.27 nm.**

To estimate the electron density, we used the Hα line profile shown in Fig. 6.8b fitted with a Lorentzian curve (a Voigt fit could not successfully separate the Gaussian and Lorentzian contributions). Since the Doppler broadening is negligible here, the main Gaussian contribution to the line broadening is given by the instrumental profile. Using the Gaussian broadening w_G as the 3-pixel resolution of the spectrometer, i.e. 0.7 nm, as stated above, we estimate the Lorentzian full width at half maximum (FWHM) broadening w_L of the line using the Voigt width approximation,[23]

$$w_{tot} \approx 0.5346\, w_L + (0.2166\, w_L^2 + w_G^2)^{1/2}, \quad (1)$$

where $w_{tot} = 1.39$ nm is the total line broadening, as shown in Fig. 8b. One finds $w_L = 1.02$ nm. According to Gigosos et al.,[24] the electron density n_e is related to the full width at half area (FWHA) for the Hα line as,

$$\mathrm{FWHA} = 0.549\ \mathrm{nm} \times \left(\frac{n_e}{10^{17}\ \mathrm{cm^{-3}}}\right)^{0.67965}. \quad (2)$$

Since FWHA = FWHM for a Lorentzian function, we find $n_e = 2.5 \times 10^{17}$ cm^{-3}. This value is consistent with the electron density obtained from the broadening of the Ni I 346.17 nm line of a dry sample in a previous work,[18] although the fluence was much lower due to the larger laser spot size on the sample.

Knowing the electron number density n_e and the intensity ratio ρ between the Mg II 280.27 nm and Mg I 285.21 nm lines (Fig. 8a), the ionization temperature T_{ion} can be estimated from the NIST LIBS database,[25] or equivalently from the combined Saha and Boltzmann equations, which have the general form,

$$rn_e = f(T_{ion}) \quad (3)$$

where $f(T_{ion}, n_e)$ is a nonlinear function of T_{ion} and n_e (taking into account the lowering of the ionization threshold as a function of electron density). For the ratio ρ we used the peak areas fitted by Gaussian functions as shown in Fig. 8a (red dotted lines). Using $n_e = 2.5 \times 10^{17}$ cm^{-3} as found above and $\rho \approx 8.2$ from Fig. 6.8a, we obtain $T_{ion} \approx 1.1$ eV. Note that the ionization temperature is generally larger than the excitation temperature calculated using only neutral species, because laser-generated plasmas are not in perfect local thermodynamic equilibrium.[26] A possible source of error in the ionization temperature estimate is the self-absorption of the two Mg lines used, since they are resonant lines. However, given the low amplitude of these lines in the wet parts of the rock, we believe that the method used gives a reasonable estimate. This assumption is supported by the fact that the ratio between the areas of the Mg II 279.55 nm and Mg II 280.27 nm lines is 1.8, which is close to the theoretical value of 2, as in an optically thin plasma, for the two ionic magnesium lines.[25]

We also used the four Ca II lines identified in the caption of Fig. 6.7 to obtain an alternative estimate of the excitation plasma temperature using a Boltzmann plot. For line intensity, we used the area of the peaks fitted with a Gaussian function. The Ca II line parameters were obtained from the NIST Atomic Spectra Database.[27] The Boltzmann plot in Fig. 6.9 shows that the excitation electron temperature of the Ca ions is $T_{exc} = 1.27 \pm 0.08$ eV (where the uncertainty is estimated only from the linear regression). It should be noted that the pair of lines Ca II 393.37 nm and Ca II 396.85 nm is probably reduced by self-absorption, since they are resonant lines and the ratio of the lines is expected to be close to 2 in an optically thin plasma,[25] while in Fig. 6.7a the ratio of their areas is close to 1.4. In contrast, the ratio between the Ca II 317.93 nm and Ca II 315.89 nm lines, is around 1.9, close to the theoretical value of 2.[25] As a result, the slope of the Boltzmann plot is reduced and the temperature is overestimated. Because the two calcium ion doublet lines at 317.9 and 396.8 nm are far apart, we used a calibrated tungsten lamp and took into account the correction of the spectral response of the optical setup (fiber, spectrometer and detector).

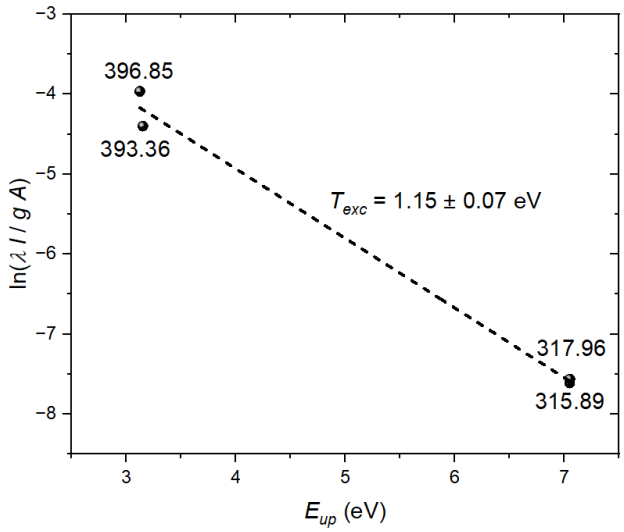

Figure 6-9 **Boltzmann plot using the four Ca II lines seen in Figure 7a. The numbers near the data points are the corresponding wavelengths of the Ca II lines. On the horizontal axis, E_{up} is the energy of the upper state. On the vertical axis, λ is the wavelength, I is the intensity, g is the degeneracy of the upper energy state and A is the spontaneous de-excitation rate.**

For comparison, we have calculated the electron number density and temperature in areas of high white light and lower Hα line intensity. We proceeded as above, except that in these areas the Ca II lines cannot be used because they saturate the camera, as can be seen in Fig.6.7c. At these locations the Hα line is broader, implying a higher electron number density, and the intensity ratio ρ between the Mg II 280.27 nm and Mg I 285.21 nm lines is similarly lower. As a result of Eq. (3), the ionization temperature T_{ion} does not change significantly. For example, in the typical case of pixel (1,50), we found from the spectra shown in Figs.6.10a and 10b, $n_e = 6.2 \times 10^{17}$ cm^{-3} and $\rho \approx 2.3$, which corresponds to almost the same ionization temperature of $T_{ion} \approx 1.05$ eV as that found for the low white light emission. Similar results are obtained for other areas of high white light emission, such as pixels belonging to the upper part of the scan matrix. However, it should be noted that self-absorption is probably more important in this case, as suggested by the ratio of the areas of the Mg II 279.55 nm and Mg II 280.27 nm lines, which is only 1.5.

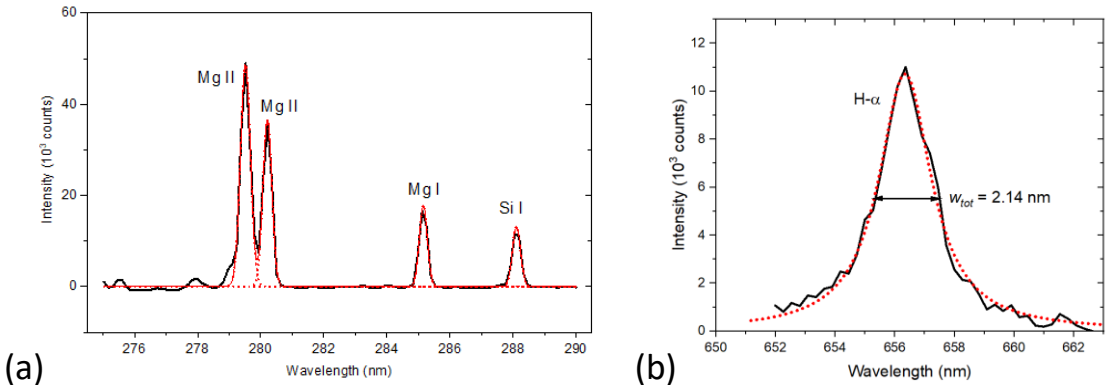

Figure 6-10 **Spectral lines used to estimate plasma properties in the high white light emission region, here for pixel (1,50). Black lines: measured spectra with baseline subtracted; red dotted lines: peak fits. (a) H 656.27 nm (H-α); (b) Mg II 279.55 nm, Mg II 280.27 nm and Mg I 285.21 nm.**

We conclude from this study of electron density and temperature that at the relatively high fluence of ~4 kJ cm^{-2} used in our experiments, the plasma properties in the high and low white light emission regions are quite similar in terms of space and time averaged temperature and electron density, although the plasma magnitude and duration may differ significantly, as discussed below.

6.4.4 Physical mechanisms

As with most ablation processes using nanosecond laser pulses, the primary energy deposition mechanism is likely to be collisional absorption, where electrons gain energy from the laser as they collide with heavy particles, then transfer their energy to atoms and produce more electrons through collisional ionization. In the case of water, this absorption mechanism is likely to be the main one, since multiphoton absorption at 1064 nm is weak at our relatively low operating laser intensity of ~1011 W cm^{-2}, considering that the photon energy is 1.17 eV, while the energy band gap of pure water is about 7 eV. However, multiphoton ionization of the water or ionization of the rock is probably required to produce the seed electrons necessary for plasma generation in pure water. Optical excitation of water molecules is probably negligible, since the absorption length of water at 1064 nm is on the order of 1 cm, which is much larger than the thin layer of water on the surface of the rock.

The fact that the plasma properties are relatively independent of the water content, while the white light emission is critically dependent on it, can be understood by invoking two complementary mechanisms. The first is the formation of a water plasma that absorbs some of the laser energy that is no longer available to form a rock plasma, resulting in less rock ablation and thus less white light emission. In fact, the energy density required to vaporize and dissociate water molecules can

be estimated at 53 kJ cm-3, which is comparable to the 95 kJ cm-3 required to vaporize and dissociate silica, the main constituent of rock. Since a layer of water covers the surface of the rock, as in the wetter part, it is possible that a significant fraction of the laser energy is first deposited in this water layer, with the remainder deposited on the rock surface. The reduced amount of ablated rock material would mix with the energetic water plasma, producing a weaker white light emission with the characteristics of the energetic plasma. Second, the presence of hydrogen in the water plasma is likely to imply a smaller and more short-lived plasma due to the high thermal conductivity of hydrogen, whose atoms and ions quickly escape the hot plasma region due to their low mass, thus cooling the plasma. In addition, because of its low mass, hydrogen gains energy faster than other heavy particles from collisions with high-energy electrons, since the collisional energy transfer is proportional to the mass ratio of the electron to the heavy particle. In steady-state arc plasmas at atmospheric pressure, the addition of hydrogen in the plasma is known to decrease its electron density, suggesting that the plasma cools faster in this case.28 Therefore, the high electron temperature and number density observed in the wet rock plasma may correspond to an early stage of the plasma not much different from that generated in the dryer part of the rock. However, the ablation rate of the rock is lower due to the shorter plasma lifetime.

6.5 Conclusion

We have investigated the effect of moisture on the LIBS spectra of a piece of solid palladium ore with the aim of clarifying the correct conditions for using LIBS at a mine site where moisture may be an issue. We took LIBS spectra at a wavelength of 1064 nm and a fluence of ~ 4 kJ cm^{-2} at 2 Hz over an 18 × 60 matrix of locations on a flat surface of the rock immediately after removing the sample from immersion in water, where it remained for one week. We measured the plasma white light emission (averaged over 2048 wavelengths between 425 and 920 nm) and used the net peak of the Hα line to characterize the amount of water on the surface of the rock. Since each matrix point was taken at a well-defined time, it was possible to correlate the drying process with the LIBS signal. We found that both white light emission and Hα line intensity form complex mosaics on the color matrix, indicating that the LIBS signals depend significantly on local rock surface properties such as composition, porosity, and asperities. The white light emission shows a general trend, increasing from the early wet part to the later dry part. In the wetter part, the spectra are weak (except for the hydrogen lines) and noisy, while in the drier part they are intense and many lines saturate the camera. The averages of the 60 positions of each line show a meaningful behavior, consistent with the total weight of the rock as a function of time, as well as

measurements made with an industrial moisture meter. We found that white light emission and Hα line intensity were not correlated early in the drying process but became significantly correlated later when the rock was nearly dry. This result is due to the highly variable water content in the wetter areas and stoichiometric emission in the drier part of the rock. We also studied the plasma properties at some positions corresponding to weak white light emission/high Hα line intensity and high white light emission/low Hα line intensity and found that the space- and time-averaged plasma electron number density and ionization temperature are similar in all cases. Since the white light emission is mainly due to the ablation of the rock surface, we attributed the weak white light emission in the wetter part of the rock to both the laser energy losses associated with the formation of the water plasma and the shorter plasma lifetime due to the increased plasma thermal conductivity caused by the high energy and high mobility of hydrogen.

This study, performed on a flat but unpolished rock sample, shows that water content is a critical parameter to consider in LIBS analysis. However, in the mining environment, control of this parameter can be problematic, for example in large samples, including walls, where dripping water is common. Whenever possible, LIBS measurements should be performed on dry samples, which can be achieved by applying a stream of hot air to the surface to be analyzed prior to LIBS analysis.

AUTHOR INFORMATION

Samira Selmani is a PhD student at the INRS, Canada. She received her education as a geologist at the National School of Engineering of Sfax, Tunisia, and at the University of Limoges, France. Her current research focuses on the analysis of mineralized rocks, in particular the quantification of their precious metal content, using the LIBS technique.

François Vidal has been a research professor at the INRS, Canada, since 2003. He holds a PhD in theoretical subatomic physics from the University of Montreal, Canada. His research focuses on the theory and numerical modeling of various physical phenomena, with particular emphasis on plasma physics, laser-matter interactions, and data processing methods in the field of LIBS.

Corresponding Authors

*Samira Selmani

Email address: samira.selmani@inrs.ca

*François Vidal

Email address: francois.vidal@inrs.ca

Notes

The authors declare no competing financial interest.

ACKNOWLEDGMENT

The authors thank Lionnel Djon of Impala Canada for providing quarter drill cores from the Lac des Iles mine and their laboratory analysis, and for financial support from Impala Canada. This work was primarily supported by the National Science and Engineering Research Council of Canada (NSERC) [grant number STPGP 521608-18].

Tables

Table 1. **Partial chemical composition in wt. % of the long half of the 1 m long core from which the fragment used in this study was taken.**

Si	Ca	Fe	S	Cu	Ni	Al	Mg
24.2	6.6	4.7	0.35	0.14	0.31	7.7	7.8

Figure Captions

Fig. 1 Photographs of the core fragment from the Lac des Iles mine used in this study after laser scanning on an 18×60 matrix with 0.95 mm between laser shots. The laser shot imprints appear as lighter marks on the rock surface.

Fig. 2 Methods used to measure the time dependence of the moisture content of a rock sample and its influence on the LIBS spectra. The sample is removed from a 1000 ml beaker filled with water after 1 week and then either weighed, or probed with a moisture meter, or scanned with a LIBS system where a laser beam creates a plasma on the sample and the light emitted by the plasma is collected by two spectrometers in different spectral ranges. M: mirror, TAMS: three-axis motorized stage, F1 and F2: fiber bundles, L1, L2 and L3: lenses.

Fig. 3 Variation of the moisture content of the rock sample. (a) Weight and (b) uncalibrated moisture content as a function of time, as given by the balance and moisture meter (set to concrete material), respectively. Error bars are the result of 3 measurements taken 3 weeks apart. The dashed curves are approximate fits.

Fig. 4 Peak of the net Hα line of the drying rock surface. (a) At each laser shot location in the 18 row × 60 column matrix. Each row is scanned from column 1, starting at (1,1). The scale is in counts. (b) Averaged over each row. The dashed curve shows the overall trend.

Fig. 5 White light emission in the 425-920 nm spectral window from the drying rock surface. (a) At each laser shot location in the 18 row × 60 column matrix. Each row is scanned from column 1, starting at pixel (1,1). The scale is in counts. (b) Averaged over each row. The dashed curve shows the overall trend.

Fig. 6 Correlation coefficients between the 60 values of each row of the maps of Figs. 4 and 5.

Fig. 7 Examples of raw spectra of the scanning matrix for pixels (1,44) and (1,50) with reference to Figs. 4a and 5a. (a) and (b) in an area of low white light emission (pixel (1,44)); (c) and (d) in an area of high white light emission (pixel (1,50)). In the latter cases, several lines saturate the camera. The lines identified are Mg II 279.55 nm, Mg II 280.27 nm, Mg I 285.21 nm, Ca II 315.89 nm, Ca II 317.93 nm, Ca II 393.37 nm, Ca II 396.84 nm, and Hα (highlighted by the red dashed ellipse in (d)).

Fig. 8 Spectral lines used to estimate plasma properties in the low white-light emission region, here for pixel (1,44). Black lines: measured spectra with baseline subtracted; red dashed lines: peak fits. Lines identified: (a) Mg II 279.55 nm, Mg II 280.27 nm, and Mg I 285.21 nm; (b) Hα.

Fig. 9 Boltzmann plot using the four Ca II lines in Fig. 7a. The numbers near the data points are the corresponding wavelengths of the Ca II lines in nm. On the horizontal axis, E_up is the energy of the upper state. On the vertical axis, λ is the wavelength, I is the line intensity, g is the degeneracy of the upper energy state, and A is the transition probability of the emission line.

Fig. 10 Spectral lines used to estimate plasma properties in the high white light emission region, here for pixel (1,50). Black lines: measured spectra with baseline subtracted; red dotted lines: peak fits. Lines identified: (a) Mg II 279.55 nm, Mg II 280.27 nm and Mg I 285.21 nm (b) Hα.

6.6 REFERENCES

[1]. F. Robert and A. Galley, Exploration Innovation Consortium: Keeping Canada's Mineral Exploration Globally Competitive, Presentation to CMIC Signature Event, Toronto, 2013. https://fr.slideshare.net/slideshow/franois-robert-and-alan-galley-cmics-exploration-innovation-consortium/16702268

[2]. E. Herincs, M. Puschenreiter, W. Wenzel, and A. Limbeck, J. Anal. At. Spectrom., 2013, **28**, 354–363. https://doi.org/10.1039/c3ja30367e

[3]. J. L. Molloy and J. A. Holcombe, Anal. Chem., 2006, **78**, 6634–6639. https://doi.org/10.1021/ac061016w

[4]. J. Tickner, J. O'Dwyer, G. Roach, M. Smith, and Y. Van Haarlem, Radiat. Phys. Chem., 2015, **116**, 43–47. https://doi.org/10.1016/j.radphyschem.2015.01.006

[5]. Canadian Mining Industry Research Organization (CAMIRO) Exploration Division, Quality Control Assessment of Portable XRF Analyzers: Development of Standard Operating Procedures, Performance on Variable Media and Recommended Uses, CAMIRO Project 10E01, Phase I, October 13, 2013. https://www.appliedgeochemists.org/sites/default/files/images/images-old/stories/XRF/pXRF%20Report%20Phase%20I%20Report%20rev%20Oct%202013.pdf

[6]. B. Lemière and R.S. Harmon, XRF LIBS for Field Geology, John Wiley & Sons Ltd, Chapter 20, 2021.

[7]. G. E. De Benedetto, R. Laviano, L. Sabbatini, and P.G. Zambonin, J. Cult. Herit., 2002, **3**, 177–186. https://doi.org/10.1016/S1296-2074(02)01178-0

[8]. P. Lypaczewski, B. Rivard, G. Lesage, K. Byrne, M. D'Angelo, and R. G. Lee, Minerals, 2020, **10**, 473. https://doi.org/10.3390/min10050473

[9]. S. Selmani, N. Mohamed, I. Elhamdaoui, J. Fernandes, P. Bouchard, M. Constantin, M. Sabsabi, and F. Vidal, Spectrochim. Acta, Part B, 2022, **196**, 106523. https://doi.org/10.1016/j.sab.2022.106523

[10]. D.A. Cremers and L.J. Radziemski, Handbook of laser-induced breakdown spectroscopy, John Wiley & Sons, 2013.

[11]. Y. Deguchi and Z. Wang, Industrial Applications of Laser-Induced Breakdown Spectroscopy, Plasma Science and Technology - Progress in Physical States and Chemical Reactions, Chapter 14, 2016, https://doi.org/10.5772/61915.

[12]. R.S. Harmon, R.E. Russo, and R.R. Hark, Spectrochim. Acta Part B, 2013, **87**, 11–26. https://doi.org/10.1016/j.sab.2013.05.017

[13]. R.S. Harmon and G.S. Senesi, Appl. Geochem., 2021, **128**, 104929. https://doi.org/10.1016/j.apgeochem.2021.104929

[14]. R.S. Harmon, J.M. Lawley C, J. Watts, C.T. Harraden, A.M. Somers, and R.R. Hark, Minerals 2019, **9**, 718. https://doi.org/10.3390/min9120718

[15]. C. Fabre, Spectrochim. Acta Part B, 2020, **166**, 105799. https://doi.org/10.1016/j.sab.2020.105799

[16]. N. Mohamed, K. Rifai, S. Selmani, M. Constantin, F. Doucet, L. Ozcan, M. Sabsabi, and F. Vidal, Geostand. Geoanal. Res., 2021, **45**, 539–550. https://doi.org/10.1111/ggr.12385

[17]. I. Elhamdaoui, N. Mohamed, S. Selmani, P. Bouchard, M. Sabsabi, M. Constantin, and F. Vidal, J. Anal. At. Spectrom., 2022, 37, 2537. https://doi.org/10.1039/d2ja00120a

[18]. S. Selmani, I. Elhamdaoui, N. Mohamed, P. Bouchard, M. Constantin, M. Sabsabi, and F. Vidal, Appl. Phys. A 2023, **129**, 737. https://doi.org/10.1007/s00339-023-06966-7

[19]. I. Elhamdaoui, N. Mohamed, S. Selmani, P. Bouchard, M. Sabsabi, M. Constantin, and F. Vidal, , Appl. Spectrosc. 2023, **77**, 1382. https://doi.org/10.1177/00037028231202804

[20]. D. Decharte, C. Perusse, T. Hofton, C. Roney, G. Marrs, S. Taylor, S. Olson, D. Thibodeau, D. Peck, and B. Young, Feasibility study for Lac des Iles Mine incorporating underground mining of the Roby Zone. Technical Report, North American Palladium Ltd., 889 pp, 2018.

[21]. L. Hoffart, P. Lassonde, F. Légaré, F. Vidal, N. Sanner, O. Utéza, M. Sentis, J.-C. Kieffer, and I. Brunette, Optics Express, 2011, **19**, 230-240. https://doi.org/10.1364/OE.19.000230

[22]. O. Krischer, Die wissenshaftlichen Grundlagen der Trocknungstechnik, Berlin, Springer, 1963.

[23]. J. F. Kielkopf, J. Soc. Am., 1973, **63**, 987.

[24]. M.A. Gigosos, M.A. Gonzalez, and V. Cardenoso, Spectrochim. Acta, Part B, 2003, 58, 1489–1504. https://doi.org/10.1016/S0584-8547Ž03.00097-1

[25]. https://physics.nist.gov/PhysRefData/ASD/LIBS/libs-form.html

[26]. O. Barthélemy, J. Margot, S. Laville, F. Vidal, M. Chaker, B. Le Drogoff, T.W. Johnston, and M. Sabsabi, Appl. Spectrosc., 2005, **59**, 529–536. https://doi.org/10.1366/0003702053641531

[27]. https://www.nist.gov/pml/atomic-spectra-database

[28]. S. Vacquie, H. Kafrouni, A. Gleizes, Influence de la presence d'hydrogene sur la densite electronique dans un plasma d'argon. Physics Letters A, 1976, **56**, 197–198. https://doi.org/10.1016/0375-9601(76)90644-7

CHAPITRE VII

7 CONCLUSION GÉNÉRALE

Au cours de cette thèse, nous avons abordé l'intégration de la technique en géochimie, qui permet une analyse rapide in situ de la composition élémentaire et de la concentration des minéraux par ablation laser de la surface du matériau. Plus spécifiquement, cette étude a porté sur l'analyse du palladium, dans les carottes de la mine de Lac des Iles (LDI), située près de Thunder Bay dans l'Ouest de l'Ontario. L'objectif était de proposer une alternative rapide et efficace aux méthodes traditionnelles d'analyse minérale en laboratoire. La problématique initiale portait sur le fait que les méthodes analytiques traditionnelles, telles que l'ICP-MS et les essais au feu, bien que précises, nécessitaient un temps considérable pour l'extraction, le transport et le traitement des échantillons. Cela représente une perte de temps et de ressources pour les industries minières, affectant directement leur rentabilité.

Le but principal de cette thèse de doctorat était d'explorer et d'adapter la technologie LIBS afin d'optimiser la mesure de la concentration du palladium avec le LIBS (le Canada étant le troisième producteur au monde d'ÉGP et le cinquième en ce qui concerne les réserves) en vue de mettre au point un instrument compact permettant de mesurer le contenu des ÉGP dans les carottes de forage in situ et en temps réel au cours de la période d'exploitation. L'objectif était non seulement de réduire considérablement le temps d'analyse, mais également de fournir une méthode suffisamment précise pour détecter et quantifier les métaux précieux dans des gisements à faible teneur.

Dans notre première étude (article 1), nous avons montré comment la technique LIBS peut être utilisée pour estimer la concentration de palladium dans une carotte de LDI. Ces premières analyses ont permis de démontrer l'efficacité de la LIBS pour estimer rapidement la concentration d'éléments précieux, comme le palladium, tout en réduisant le temps d'analyse par rapport aux méthodes traditionnelles. Une comparaison de nos résultats a été réalisée avec des analyses de laboratoire sur l'autre moitié de la carotte de LDI. Les résultats ont montré que les concentrations obtenues avec la technique LIBS étaient cohérentes avec celles des analyses effectuées en laboratoire, ce qui confirme la fiabilité et la précision de cette technique pour des applications dans des environnements réels.

Dans la deuxième partie de notre travail (article 2), nous avons exploré les interactions entre le laser et les phases minérales présentes dans le minerai de LDI dans le cadre de l'analyse géochimique LIBS. Notre objectif était de mettre en lumière la formation des plasmas et les caractéristiques des cratères d'ablation générés dans l'air ambiant, sous pression atmosphérique,

lors de l'analyse des échantillons de minerai. Nous avons étudié en détail la morphologie des cratères dans trois phases principales du minerai de palladium : le feldspath plagioclase, l'amphibole et les sulfures. Pour cette étude, nous avons réalisé quatre séries de tirs laser (50, 250, 500 et 1000 tirs) sur ces trois phases minérales afin de mieux comprendre l'influence de la composition minéralogique sur l'efficacité de l'ablation. Il est apparu que l'ablation laser était plus efficace dans le plagioclase, probablement en raison de sa conductivité thermique plus faible par rapport à celle des autres phases. Ces résultats fournissent des indications précieuses pour l'amélioration des protocoles d'analyse LIBS dans des environnements miniers complexes, tout en ouvrant la voie à l'optimisation des performances analytiques pour différents types de minéraux.

Dans le prolongement de nos objectifs initiaux, nous avons également examiné l'influence de l'humidité des roches sur les mesures effectuées avec la technologie LIBS (article 3), ce qui peut constituer un défi pour les géologues lors de l'utilisation de cette méthode sur le terrain. Cette étude a permis de mieux cerner les contraintes liées à l'utilisation de prototypes LIBS dans des environnements humides et de proposer des solutions pour atténuer ces limitations opérationnelles. Par ailleurs, nous avons développé une stratégie d'optimisation visant à réduire le nombre de tirs laser nécessaires tout en maintenant un niveau de précision satisfaisant (article 4 (Annexe)). Cette optimisation permet non seulement de réduire le temps requis pour les mesures, mais aussi d'améliorer l'efficacité de la technique dans des conditions réelles.

L'analyse comparative entre la technologie LIBS et les méthodes traditionnelles a permis de démontrer que la LIBS n'est pas seulement un outil complémentaire, mais qu'elle a le potentiel de remplacer partiellement ou totalement les méthodes plus lentes et plus coûteuses, en offrant une solution pratique sur le terrain.

En conclusion, la technique LIBS représente un véritable atout pour l'industrie minière canadienne, en particulier pour l'extraction et l'exploitation des éléments du groupe du platine. Elle permet non seulement de réduire les coûts et le temps de traitement des échantillons, mais également d'améliorer la précision des analyses sur site. Son implémentation pourrait révolutionner les pratiques actuelles et offrir un avantage compétitif aux entreprises minières, en augmentant leurs capacités de production tout en optimisant l'utilisation des ressources disponibles.

ANNEXE I

ANNEXE I- ARTICLE 4 - ÉVALUATION DE LA CONCENTRATION EN PALLADIUM DANS DES CAROTTES DE FORAGE PAR SPECTROSCOPIE DE PLASMA INDUIT PAR LASER (LIBS)

Assessment of palladium concentration in drill cores by laser-induced breakdown spectroscopy (LIBS)

Évaluation de la concentration en palladium dans des carottes de forage par spectroscopie de plasma induit par laser (LIBS)

Auteurs :

François Vidal[1], Samira Selmani[1], Ismail Elhamdaoui[1], Nessrine Mohamed[2], Paul Bouchard[3], Marc Constantin[2], Mohamad Sabsabi[3]

[1] Institut National de la Recherche Scientifique, Centre Énergie Matériaux Télécommunications, 1650 Lionel-Boulet Blvd, Varennes, QC J3X 1P7, Canada

[2] Département de Géologie et de Génie Géologique, Université Laval, 1065 Avenue de la Médecine, Québec, QC G1V 0A6, Canada

[3] National Research Council of Canada, 75 de Mortagne Blvd., Boucherville, QC J4B 6Y4, Canada.

* Corresponding author: francois.vidal@inrs.ca

Titre de la revue ou de l'ouvrage:

Article est accepté pour la publication dans PLOS ONE (Février 2025).

dans le journal PLOS ONE

Contribution des auteurs :

Dans cet article, chaque auteur a apporté une contribution essentielle et complémentaire pour atteindre les objectifs de la recherche.

François Vidal a effectué les calculs mathématiques et numérique et s'est chargé de la rédaction du manuscrit, et procédé aux corrections et révisions nécessaires pour finaliser l'article

Samira Selmani a pris les mesures expérimentales sur les carottes. Ensuite, a analysée et interprété les données.

Marc Constantin a joué un rôle important dans l'interprétation de la minéralogie des roches.

Mohamad Sabsabi a validé les résultats. Il a contribué de manière significative par ses remarques pertinentes pour améliorer l'article.

Paul Bouchard a supervisé les aspects techniques et méthodologiques liés à l'utilisation de la LIBS.

Nessrine Mohamed a contribuée à la révision de l’article.

Ismail Hamdaoui a apporté une aide précieuse en optimisant le montage expérimental. Ses remarques pertinentes ont permis d'améliorer la configuration et l'efficacité des expérimentations, contribuant ainsi à la fiabilité des données collectées.

François Vidal, Marc Constatain, et Mohamad Sabsabi ont supervisé le projet dans son ensemble.

Tous les coauteurs ont offert leur soutien pour la rédaction et ont contribué à la révision du manuscrit.

A.1 Abstract

Laser-induced breakdown spectroscopy (LIBS) appears to be a promising technique for rapid on-site assessment of precious metal concentrations in ores. However, a number of issues need to be considered for the optimal use of this technique in practical situations. This article focuses on the number of measurements (i.e. spectra or laser shots) required to assess the mean palladium concentration in drill cores from the Lac des Iles mine (Ontario, Canada). We have performed a probabilistic study of the accuracy of the mean palladium concentration obtained by LIBS as a function of the number of measurements at random locations. For this purpose, we first used the results of a detailed laser scan of the core surface and then a mathematical model of the probability density of the palladium distribution to explore the parameter space, in particular the effect of noise on the measurements. We show that for the 1 meter long, 2-centimeter radius quarter core samples analyzed, a few thousand randomly sampled locations generally provide an assessment of the palladium concentration within useful confidence limits. For a typical laser repetition rate of 50 Hz, such an analysis is a matter of minutes compared to hours or days using conventional methods.

A.2 Introduction

Precious metals, including palladium, are commercially mined in concentrations of a few parts per million (ppm) or less. Mine samples are currently analyzed using conventional wet chemistry, fire assay, ICP [1] or atomic absorption [2] techniques after a laborious, time-consuming and energy-intensive sequence of grinding, homogenization and dissolution. One of the desired state-of-the-art technologies would be the measurement of low average grades (a few ppm) of precious metals in real time and in situ during the various phases of mining exploration and production [3].

Laser-induced breakdown spectroscopy (LIBS) is a promising technology that can meet these requirements. LIBS is an optical analytical technique based on emission spectroscopy that uses a pulsed laser beam focused on the sample (solid, liquid or gas) to atomize a small area (typically less than 1 mm^2) and create a plasma. The light emitted from the plasma is then collected and spectrally analyzed. A schematic of the LIBS setup is shown in Fig.A. 1. Reference materials are used to establish the relationship between the intensities of the spectral lines and the content of the analyte element of interest for each laser shot. The main potential advantages of LIBS over traditional analytical techniques lie in the ability to rapidly analyze samples with minimal or no preparation, regardless of the type of sample [4]. Several reviews are available on the applications of LIBS in environmental and geochemistry [5-8]. LIBS has also been adopted or is being

evaluated for its potential applications in several industries, including mineral processing, food, health, and archaeology [9].

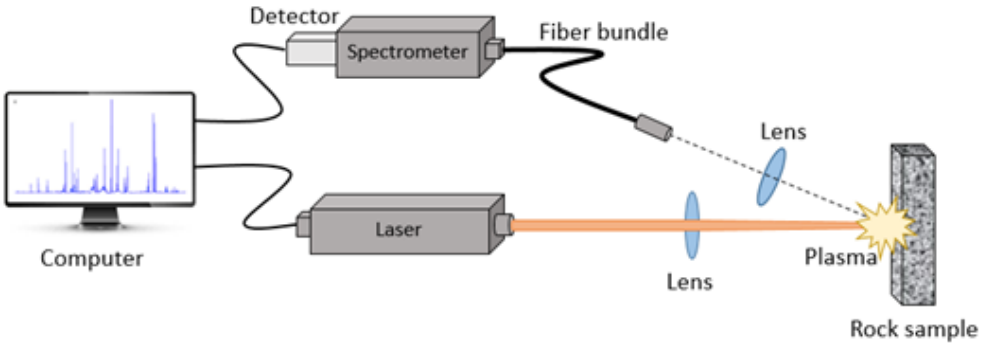

Figure A-1 Schematic of the LIBS experimental set-up

In our recent work, we measured the concentration of palladium in cores from the Lac des Iles (LDI) palladium mine in Ontario, Canada by LIBS [10] and by LIBS assisted with laser fluorescence [11]. The cores used are of gabbronorite type and come from the same zone (B3) of the LDI mine. We scanned the cores with several thousand laser shots of approximately 750 µm diameter. Ore powders spiked with various concentrations of palladium chloride were used to calibrate our measurements. Our LIBS measurements indicate that the palladium distribution on the surface of the core samples is very inhomogeneous, varying by hundreds or even thousands of ppm between adjacent locations. We then estimated the mean core concentration of palladium by averaging the concentrations for all laser shots. For the cores analyzed, the LIBS measurements were found to be in good agreement with conventional analyses performed on the transverse half of the original cylindrical cores.

Although LIBS analysis of precious metal content in cores is in principle much faster than conventional laboratory methods, it remains important to optimize the duration of the LIBS analysis by performing appropriate sampling. The duration of LIBS measurements depends on the repetition rate of the pulsed laser, the number of sites analyzed on the sample surface, and the sampling strategy used. Therefore, a trade-off must be made between the duration of the measurement (i.e. the number of laser shots) and the uncertainty in the mean concentration that is considered acceptable. An analogous issue has been discussed in [12-14] in the context of geochemical analysis of rocks containing mineral phases with concentrations in the wt% and grain sizes comparable to the laser spot size. For such samples, it was found that as few as 10-15 [12-13] or 560 [14] laser shots at different positions were sufficient to determine their mineralogical composition.

In this paper we discuss the appropriate number of LIBS measurements to assess the palladium concentration at the ppm level in drill cores with a palladium grain size much smaller than the laser spot size. The approach we use is to take as a reference the distribution of palladium concentrations from drill cores of palladium ore from the LDI mine, scanned by LIBS at M different positions, with M on the order of 104. The measured palladium distributions in the analyzed cores are presented in Sect. A.2. In Sect. A.3.1, we consider subsets of N measurements from this set of M measurements and calculate the probabilities of obtaining the mean concentration μ_N of N measurements within certain concentration limits around the reference concentration μ_M from the set of M measurements. Then, in Sect. A.3.2, we mathematically model the concentration distribution as well as the noise inherent in such measurements in a way that mimics the measured distribution for the set of M measurements. This allows us to study a wider variety of palladium and noise distributions. Sect. A. 4 concludes the paper.

A.3 Measurements

The three cores from the LDI palladium mine considered in this study, hereafter referred to as core A, B and C, are quarter cores cut longitudinally, approximately 1 m long and 2 cm in radius. Their LDI designations are listed in Table A1 in Appendix A. The three cores are of gabbronorite type, and the major phases identified by μ-XRF, polarized light microscopy, and electron probe microanalysis are (1) calcium-rich plagioclase feldspar (mainly bytownite), (2) amphibole (mainly hornblende), and (3) sulfides (mainly chalcopyrite, pentlandite, pyrrhotite, and pyrite) [15]. The diameter of the laser spot on the target was approximately 750 μm, and the analyzed areas were separated by 1 mm in both directions. The size of platinum group minerals in the LDI mine is known to be less than a few tens of μm [16], which is much smaller than the laser spot size. Figs A.2a and 2b show examples of LDI core fragments as delivered from the mine site.

Details of the laser parameters and experimental conditions used for the LIBS analysis of cores A and B are given in our previous work [10]. Briefly, the laser pulses generated by a Ng:YAG laser had a duration of 8 ns and a wavelength of 1064 nm. The laser fluence on the target was approximately 18 J cm^{-2}, the used acquisition delay and gate width were 4 and 10 μs, respectively, and the measurements were performed in ambient air. For these parameters, each laser shot was found to ablate 10^{-4} – 10^{-3} mm3 of material at the surface of the rock, depending on the mineral phase [17]. The palladium concentration for each laser shot was determined using 3 univariate calibration curves obtained from 3 sets of 6 reference materials each, as described in [10]. Fig. A.2c shows an example of a laser-scanned face of a fragment from core A, while Fig.

A.2d shows the mirror image of this face, created by cutting the rounded side of the fragment to produce an additional flat surface. Core C was analyzed with slightly different laser parameters. The fluence was 14 J cm^{-2}, and the acquisition delay was 3 µs, respectively. In addition, only one calibration curve obtained from a set of 6 reference samples was used.

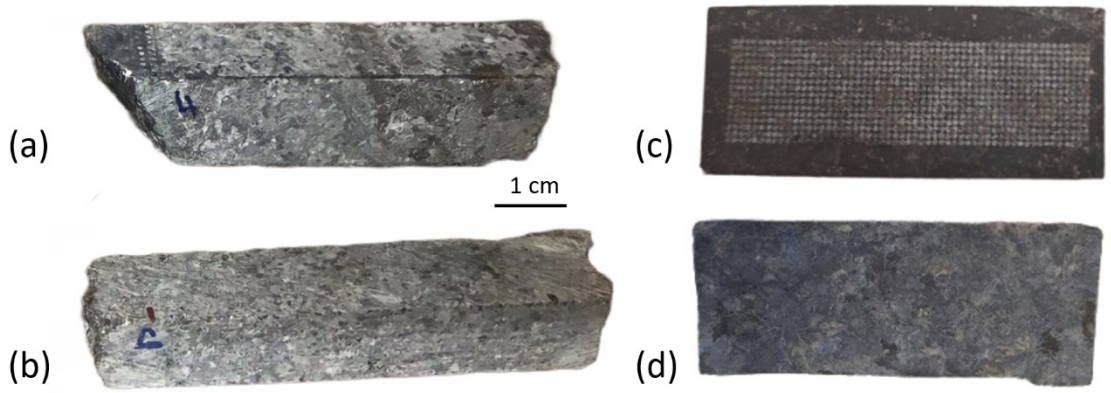

Figure A-2 **Photos of quarter core fragments from the Lac des Iles palladium mine. Examples of core fragments as delivered from the mine site. (a) and (b): Examples of core fragments as delivered from the mine site. (c): Example of a fragment face from core A after**

Fig A.3 shows a raw (un-normalized) spectrum obtained from a laser shot at core A, centered on the Pd I 348.12 nm line used for palladium concentration determination. The spectrum is characterized by strong emission lines from iron and nickel, both high-emission elements. Background noise is also present due to inherent fluctuations in plasma emission, electronic variations, and the ICCD camera. In this case, the palladium line is clearly distinguishable from the background noise. However, when the palladium concentration is lower, the net palladium intensity $I_{Pd,net}$, calculated as the peak intensity minus the average background (represented by the dashed line), can approach the noise level. In some cases, $I_{Pd,net}$ may even become negative due to random noise fluctuations around the background level. This noise limitation ultimately defines the palladium detection limit of our LIBS system, which is estimated to be about 5 ppm [10]. Since the calibration curves exhibit a linear relationship $C_{Pd} \propto I_{Pd,net}$, negative $I_{Pd,net}$ values translate into negative C_{Pd} values. Although negative concentrations are physically meaningless, they are included in the analysis for statistical accuracy. These negative values compensate for the excess positive concentrations introduced by noise, ensuring an accurate evaluation of average concentrations.

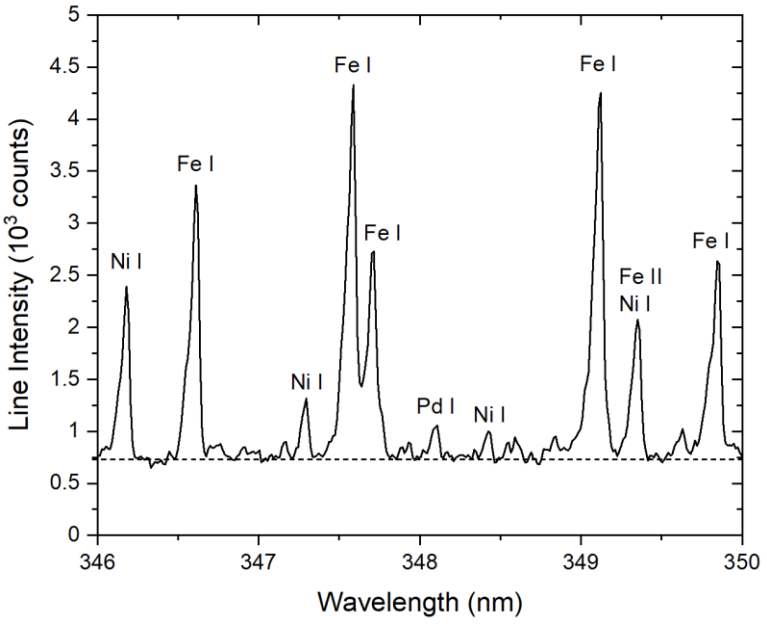

Figure A-3 **Example of a raw spectrum around the Pd I 348.12 nm line. The dashed line represents the average background emission.**

Figure A.4 shows a portion of the concentration distribution of the three cores considered in this study as determined by LIBS. The results of the LIBS analyses are summarized in Table 8.1 which shows the number of laser shots performed on the three cores as well as the mean concentration and standard deviation calculated from the distributions shown in Fig. A.4. Due to our laboratory setup, we were only able to scan the flat surfaces of the cores. Only the two flat surfaces of quarter cores B and C were scanned. For core A, we cut the round surface to form a third flat surface, which was also laser scanned.(see Fig A.2c). The number of laser shots is not the same for the three cores due to this reason and the condition of the core fragments, which allowed more or less large rectangular laser scan matrices. While the concentration range in Fig. A.4 is limited to 1000 ppm for better visibility, the highest concentrations reach a few thousand ppm for the three cores. The complete datasets of measurements for the three cores are provided in the Supporting Information files. Note the presence of negative concentrations resulting from the extension of the calibration curve to negative values of $I_{Pd,net}$, as discussed above. The mean palladium concentration has been calculated taking into account these negative concentrations, which are offset by the part of the positive concentrations also due to noise, as discussed in detail in Sect. A.3.2.

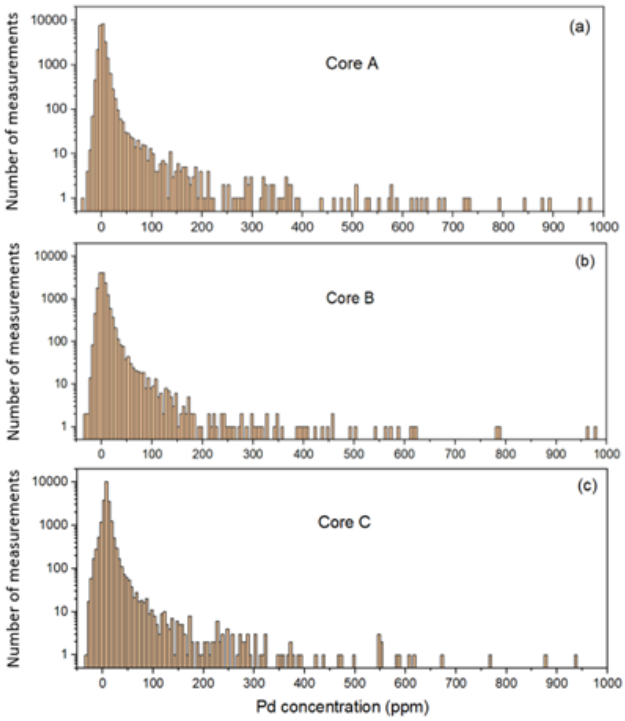

Figure A-4 **Experimental distribution of palladium concentration. Palladium distribution in ore from. the LDI palladium mine for the three cores considered in this study.The bin size of the histograms is 5 ppm.**

Tableau A-1 **Results of the LIBS analysis of the three-quarter cores from the LDI mine considered in this study.**

Core	Number of laser shots, M	Mean Pd concentration, μ_M (ppm)	Standard deviation, σ_M (ppm)
A	25 165	5.4	49
B	16 030	6.5	42
C	22 698	10.1	29

For all three cores, the LIBS measurements are in fairly good agreement with those determined by a certified laboratory using conventional methods for the longitudinal half of the original cylindrical cores, which are 4.9 ppm for core A, 7.7 ppm for core B and 12.8 ppm for core C. This agreement was achieved despite the fact that LIBS performs a surface analysis, whereas wet chemical methods are applied to samples ground to grains of about 75 µm.

A.3 Probability calculations

A.3.1 Probability calculations using experimental measurements

In this section, we generate many random sets of N values, where N ranges from 125 to 7 000, from among the M experimental measurements made on the cores, and we use them to compute the probabilities of finding the mean concentration μ_N of any single set of N measurements within

predefined limits. To generate random sets of N values among the M experimental measurements, we used the xoshiro256** pseudorandom number generator with a period of $2^{256} - 1$, as implemented in the GNU Fortran compiler.

Two types of concentration bounds are considered. First, we consider the lower (C_5) and upper (C_{95}) concentrations corresponding to a 90% probability of obtaining a mean concentration between these two values, with 5% probabilities at either end of obtaining a mean concentration μ_N outside this interval. Second, we consider the probabilities of obtaining a mean concentration μ_N within an interval of ± 30% around the mean concentration μ_M of the M measurements.

A key concept in this study is the Central Limit Theorem (CLT) of probability theory. Stated simply, suppose the concentration distribution is characterized by a mean μ and a standard deviation σ. According to the CLT, the mean concentration distribution of a large number of randomly and independently selected sets of N measurements will tend toward a normal (Gaussian) distribution with mean μ and standard deviation $\sigma N^{-1/2}$ as N increases. The consequence of the CLT is that a larger number of measurements provides a greater accuracy in the mean concentration μ_N (i.e. a smaller values of $\sigma N^{-1/2}$) and a larger standard deviation σ requires more measurements to achieve a given accuracy. High values of σ can be associated with the presence of local high concentrations (nuggets), in the case of a trace element which is predominantly present in discrete minor phase particles.

We generated the sets of N elements in a completely random manner, without the constraints that each element appears only once in a given set and that all sets are different. This is equivalent to extending the set of M elements by an infinite replication of itself. In this way, M^N sets of N elements can be formed.

Figure A.5 shows the normalized distribution obtained from the mean concentrations μ_N of 106 randomly and independently generated sets of $N = 5\,000$ measurements on core A. The mean of this distribution is $\langle \mu_N \rangle = 5.4$ ppm, exactly the mean μ_M of the set of $M = 25\,165$ measurements, and its standard deviation is 0.70 ppm, the same value as $\sigma_M N^{-1/2} = 0.70$ ppm expected from the CLT. As also expected from the CLT, the obtained distribution for μ_N is close to a normal distribution, in contrast to the distribution of the M measurements (Fig. A.4a). However, the strong skewness of the latter does not lead to a true normal distribution for $N = 5\,000$. The concentrations C_5 and C_{95} at 5% and 95% cumulative probability, respectively, are also shown. It follows that the mean concentration of any randomly selected N measurements has a 90%

probability of being between C_5 and C_{95}, with a 5% probability at either end of obtaining a mean concentration outside this range.

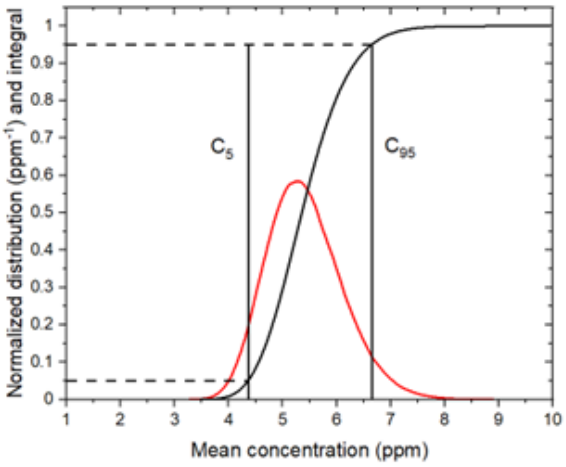

Figure A-5 **Normalized mean concentration distribution. Mean concentrations μ_N obtained from 106 random sets of $N = 5\,000$ measurements (red curve) using the experimental data for core A. The black curve is the cumulative probability (integral of the red curve as a function of the mean concentration). The concentrations $C_5 = 4.36$ ppm and $C_{95} = 6.64$ ppm correspond to 5% and 95% of the cumulative probability, respectively.**

Figure A.6 shows C_5 and C_{95} for different numbers of measurements N, between 125 and 7 000, for 106 random sets of N measurements for cores A, B and C. The value of 106 was chosen here to obtain reproducible results when repeating the calculations with a different seed in the random number generator. For all values of N we find negligible differences between $\langle \mu_N \rangle$ and μ_M for the three cores. It can be seen that the gap between C_5 and C_{95} narrows as N increases due to the decrease in standard deviation as $\sigma_M N^{-1/2}$. In addition, C_5 and C_{95} become increasingly symmetric about μ_M as N increases, that is, as the distribution becomes closer to a normal distribution. For a normal distribution, C_5 and C_{95} slowly converge to μ_M proportional to $N^{-1/2}$. Looking at core A, for $N = 7\,000$, $C_{95} - \mu_M = 1.03$ ppm and $\mu_M - C_5 = 0.90$ ppm which means that for any randomly distributed $N = 7\,000$ measurements, there is a 90% chance that the mean concentration μ_N has an error between +19% and –17% of the mean concentration $\mu_M = 5.4$ ppm.

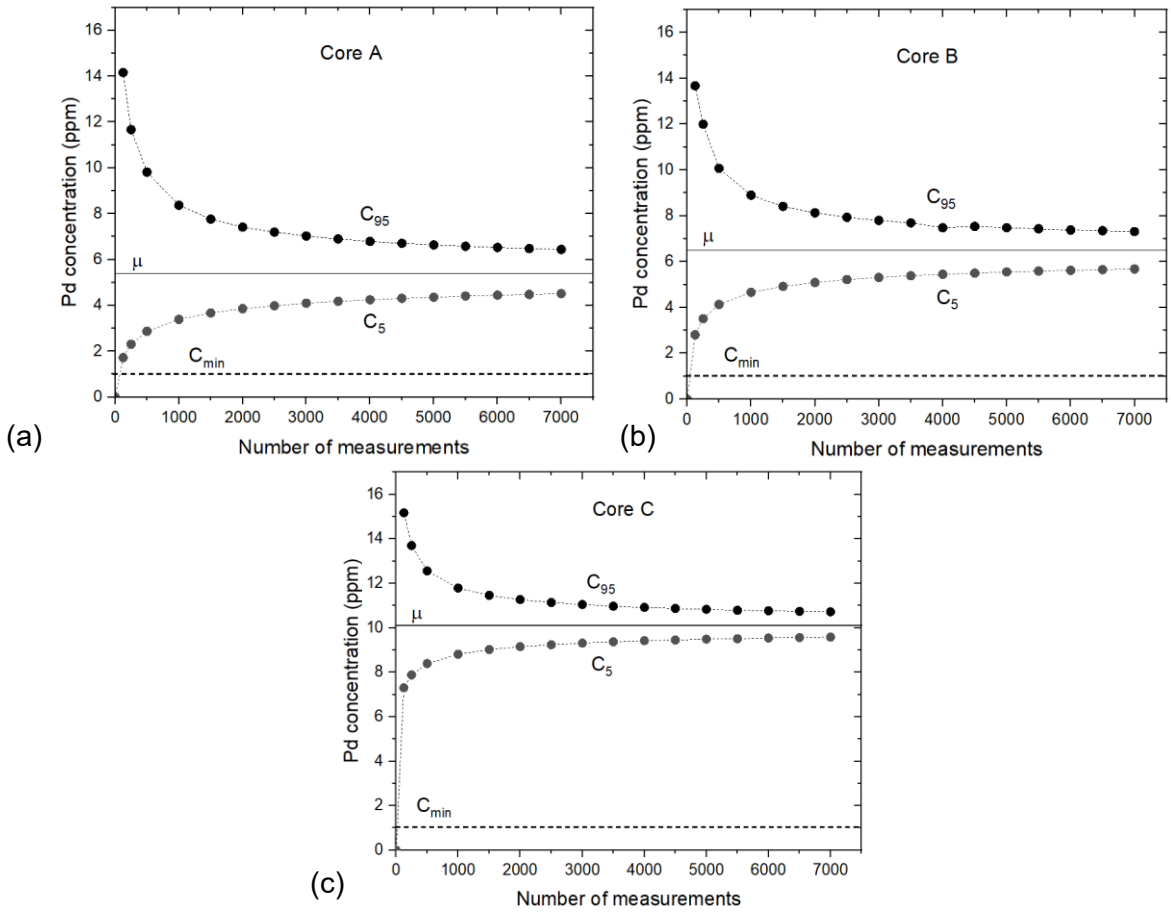

Figure A-6 **Palladium concentrations vs. number of measurements for cores A, B and C. C_5 and C_{95} at 5% and 95% of the cumulative probability, respectively, as a function of the number of randomly selected number of measurements N, for 106 sets of N measurements. For all values of N, $\langle \mu_N \rangle = \mu_M$ which takes the values given in Table 1. The dashed line C_{min} = 1 ppm represents the threshold concentration for the exploitability of the palladium ore.**

An important practical parameter to consider is the lower concentration limit for ore exploitability which depends on the economics of the extraction process. For the various mineralized zones at the LDI mine, the palladium cut-off grade varies from 0.8 to 1.8 ppm [18]. In this work we set this limit at C_{min} = 1 ppm. By definition, parameter C_5 represents the threshold concentration such that there is only a 5% chance that the mean concentration μ_N for N measurements will fall below this value. Figure A.6 shows that it would take less than $N = 125$ randomly distributed measurements (i.e. so that $C_5 > C_{min}$) to confirm with 95% certainty that the ore is suitable for processing.

In case an absolute measurement of the palladium concentration is required, we also calculated the probability P_{30} of obtaining a mean concentration μ_N within ± 30% of μ_M. This error value seemed to us to be a reasonable choice to obtain a useful estimate of the mean concentration.

Figure A.7 shows the probability P_{30} as a function of the number of measurements N for 106 sets of N measurements. We can see that P_{30} quickly approaches 100% as the number of measurements N increases. Assuming that the distribution is close to normal for large values of N and using the properties of the error function, we can show that

$$100\% - P_{\gamma\times100} \approx \frac{1}{\sqrt{\pi}\beta}\exp[-\beta^2], \quad \textbf{(A.1)}$$

when $\beta > 1$, where $\beta = \gamma\mu_M/(\sqrt{2}\sigma_M N^{-1/2})$, the approximation improving as β increases. Therefore, a smaller value of σ_M/μ_M favors a faster convergence of $P_{\gamma\times100}$ to 100% as N increases. This explains the comparative convergence rate of cores A, B, and C, since σ_M/μ_M = 9.1, 6.7, and 2.9, respectively.

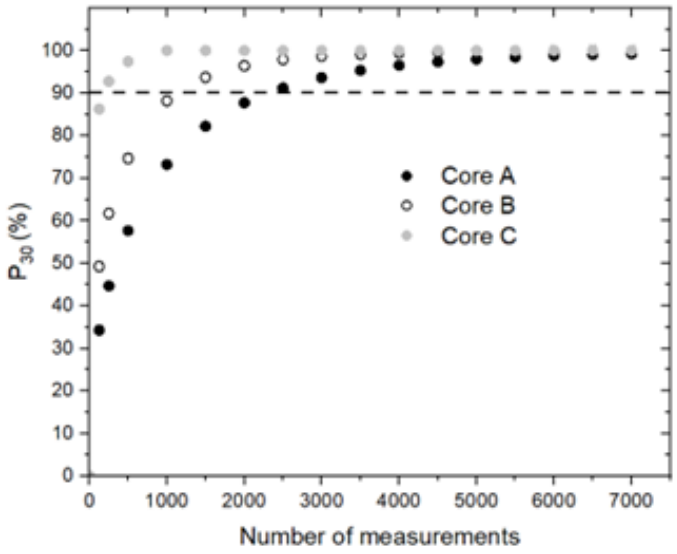

Figure A-7 **Probability of obtaining a palladium concentration within ± 30% of the mean concentration μ_M as a function of the number of randomly selected measurements N, for 106 sets of N measurements. The dashed horizontal line represents the threshold for a probability ≥ 90%.**

A.3.2 Mathematical model

In this section we discuss the approach of using an analytical concentration distribution instead of a particular set of experimental data as in the previous section. This allows one to establish a conceptual framework without being limited to a particular set of M measurements, to clarify the uncertainties associated with a finite set of M measurements, to understand the effects of noise in the measurements, and to compute probabilities for arbitrary mean concentrations μ. We will focus mainly on core A, since measurements were made on three faces of the core, and the

number of measurements is higher than for cores B and C, and thus likely more representative of the actual distribution of palladium in the core.

Measurements, such as those shown in Figure A.4, suggest that this analytical concentration distribution should have a steep slope for low concentrations and a gentle slope for high concentrations. The family of two-parameter functions of the form

$$f(x) = \exp\left[-\left(\frac{x}{\lambda}\right)^{\alpha}\right], \tag{A.2}$$

where $0 \leq x < \infty$ is the palladium concentration and λ is a scaling parameter, meets these criteria provided $\alpha <$ 1. The normalized function $\hat{f}(x) = f(x)/\int_0^\infty f(x)dx$ is the probability density (i.e. $\hat{f}(x)dx$ is the probability of measuring the concentration x within an interval dx containing x).

The mean concentration is given by

$$\mu = \int_0^\infty x\hat{f}(x)dx, \tag{A.3}$$

and the variance by

$$\sigma^2 = \int_0^\infty (x-\mu)^2\hat{f}(x)dx. \tag{A.4}$$

Here, the concentration variable x is the continuous version of the discrete variable x_i, which is the result of the ith laser shot. Each laser shot performs a local averaging over the area covered by the laser spot. In a loose analogy to the CLT, one might expect that this averaging process (which makes sense provided the laser spot size is much larger than the grains containing palladium) would lead to a decrease in the variance of the empirical probability density $\hat{f}(x)$ as the laser spot size increases but would not affect its mean value.

As discussed below, the value $\alpha = 1/10$ gives a palladium distribution of the studied core for $N = 25\,165$ virtual measurements similar to the experimental result, with the right balance between the low and high concentration populations. Smaller values of α increase the probability of obtaining higher concentrations, while larger values of α emphasize the low concentration population. However, no clear differences could be found between values of α around $1/10$. For $\alpha = 1/10$, we get the following exact results

$$\int_0^\infty f(x)dx = 3.6288 \times 10^6\,\lambda, \tag{A.5}$$

$$\mu = 3.352212864 \times 10^{11}\,\lambda, \tag{A.6}$$

$$\sigma^2 = 2.425315246554341965824 \times 10^{25}\,\lambda^2. \tag{A.7}$$

Therefore, the ratio σ/μ, which determines the rate of convergence of $P_{\gamma\times100}$ to 100%, Eq. (9.1), is 14.69 for $\alpha = 1/10$. For comparison, $\sigma/\mu = 8.67$ for $\alpha = 1/8$, $\sigma/\mu = 11.29$ for $\alpha = 1/9$, $\sigma/\mu = 19.10$ for $\alpha = 1/11$, and $\sigma/\mu = 24.82$ for $\alpha = 1/12$.

Fixing the mean palladium concentration at $\mu = 5$ ppm, approximately as in core A studied in the previous section, we find $\sigma = 73.45$ ppm. This value of σ is higher than the value obtained from the $M = 25\,165$ measured spectra ($\sigma_M = 49$ ppm). However, as we will see below, the value of σ_N can vary considerably from one set of $N = 25\,165$ virtual measurements to another. The probability density for these parameters is shown in Fig. 8.7 (solid line).

To account for the noise inherent in the experimental measurements, we assumed a Gaussian concentration noise given by the probability density

$$\hat{f}_n(x) = \frac{1}{s_n\sqrt{2\pi}}\exp\left[-\frac{1}{2}\left(\frac{x}{s_n}\right)^2\right], \quad \textbf{(A.10)}$$

where $-\infty < x < \infty$ and s_n is the standard deviation. Gaussian noise is generally considered a reasonable approximation for a wide variety of source noise in measurements. s_n is expected to be comparable to the detection limit of palladium in our experiments, which we estimated to be 5-10 ppm per laser shot for core A [Selmani et al. 2022].

The probability density for the palladium distribution including noise is given by the convolution

$$\hat{f}'(x) = \int_0^\infty \hat{f}(x')\hat{f}_n(x-x')dx', \quad \textbf{(A.11)}$$

which is shown in Fig.A.8 for $s_n = 5$ ppm (dashed curve). It can be seen that the noise significantly smears $\hat{f}(x)$ around $x = 0$ but its effect becomes negligible for $x > 25$ ppm.

Note that Gaussian noise does not affect the mean concentration μ. If we define μ' as the mean concentration taking into account the noise, we have

$$\mu' = \int_{-\infty}^{\infty} x\hat{f}'(x)dx = \int_0^\infty \hat{f}(x')\left(\int_{-\infty}^{\infty} x\hat{f}_n(x-x')\,dx\right)dx'. \quad \textbf{(A.12)}$$

The inner integral gives x', from which we conclude that $\mu' = \mu$. This result justifies considering the entire experimental concentration distribution, including the negative part, when evaluating the mean palladium concentration. Similarly, we show that the variance of $\hat{f}'(x)$ is the sum of the variances of the convolved functions (i.e. $\sigma'^2 = \sigma^2 + s_n^2$). In the presence of noise, the standard deviation of the mean concentrations of N measurements becomes $\sigma' N^{-1/2}$. Note that these results hold not only for Gaussian noise, but for any function $\hat{f}_n(x)$ that is symmetric about $x = 0$ where s_n^2 is the variance of $\hat{f}_n(x)$.

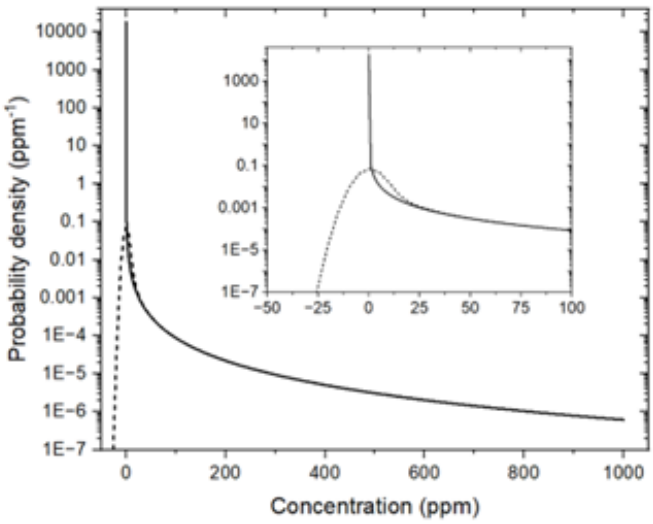

Figure A-8 **Probability densities as a function of the palladium concentration. Full curve: $\hat{f}(x)$ computed from Eq. (9.1) with $\alpha = 1/10$ and $\lambda = 1.49 \times 10^{-11}$ ppm ($\mu = 5$ ppm). Dashed curve: convoluted function $\hat{f}'(x)$ computed from Eq. (9.11) with $s_n = 5$ ppm. The inset is a magnification around $x = 0$.**

To demonstrate the suitability of the probability density $\hat{f}'(x)$ and its selected parameters for modeling distributions like those of Fig. A.2, we randomly performed N virtual measurements in a manner similar to that done in Sect. A.1 with the experimental data. To do this, we first solved the following equation for the noiseless palladium concentration x_{Pd}

$$\int_0^{x_{Pd}} \hat{f}(x')dx' = y, \tag{A.13}$$

where y is a random variable uniformly distributed in [0, 1[. For the function $\hat{f}(x)$ with $\alpha = 1/m$, this equation becomes

$$1 - e^{-z} \sum_{k=0}^{m-1} \frac{z^k}{k!} = y, \tag{A.14}$$

where $z = \left(\frac{x_{Pd}}{\lambda}\right)^{1/m}$.

The noise x_n for each measurement of the palladium concentration is given by

$$\int_{-\infty}^{x_n} \hat{f}_n(x')dx' = y', \tag{A.15}$$

where y' is a random variable uniformly distributed in]0, 1[. For Gaussian noise, Eq. (A.10), this equation becomes

$$\frac{1}{2}\left(1 + \mathrm{erf}\left[\frac{x_n}{s_n\sqrt{2}}\right]\right) = y'. \tag{A.16}$$

From a computational point of view, for a random number y, a concentration $x_{Pd} \geq 0$ is calculated from Eq. (8.13), and then for a random number y' a noise-related concentration x_n from Eq. (8.15), which can be positive or negative, is added to x_{Pd}, so that the concentration is $x = x_{Pd} + x_n$. In the following calculations, we solved Eqs. (A.13) and (A.15) by the Newton-Raphson method for each set of y and y' with an accuracy of less than 2×10^{-7} ppm. Another parameter used in the calculations is the range of x_n which we set as $-20s_n \leq x_n < 20s_n$ to ensure the convergence of the solution of Eq. (A.15).

Typical examples of the palladium concentration distribution obtained using the procedure described above are shown in Fig. A.9. The number of virtual measurements used in Figs. A.9a, 9b and 9c is equal to the number of experimental measurements performed on core A, B, and C, respectively, as described in Sect. A.1. There is an evident similarity to the experimental distributions of Fig. A.4. Of course, there is a very large number of possible realizations, since each is generated from N random numbers y and y', and the limit is mostly determined by the accuracy of the solutions of Eqs. (A.13) and (A.15). In the case shown in Fig. A.9a, $\mu_N = 5.5$ ppm and $\sigma_N = 59$ ppm, in the case shown in Fig. A.9b, $\mu_N = 7.7$ ppm and $\sigma_N = 167$ ppm, while in the case shown in Fig. A.9c, $\mu_N = 10.5$ ppm and $\sigma_N = 135$ ppm. These values differ from μ and σ' of the analytical probability densities ($\mu = 5$ ppm and $\sigma' = 74$ ppm for Fig. A.9a, $\mu = 7$ ppm and $\sigma' = 102$ ppm for Fig. A.9b, and $\mu = 10$ ppm and $\sigma' = 147$ ppm for Fig. A.9c) due to the limited sampling of N virtual measurements.

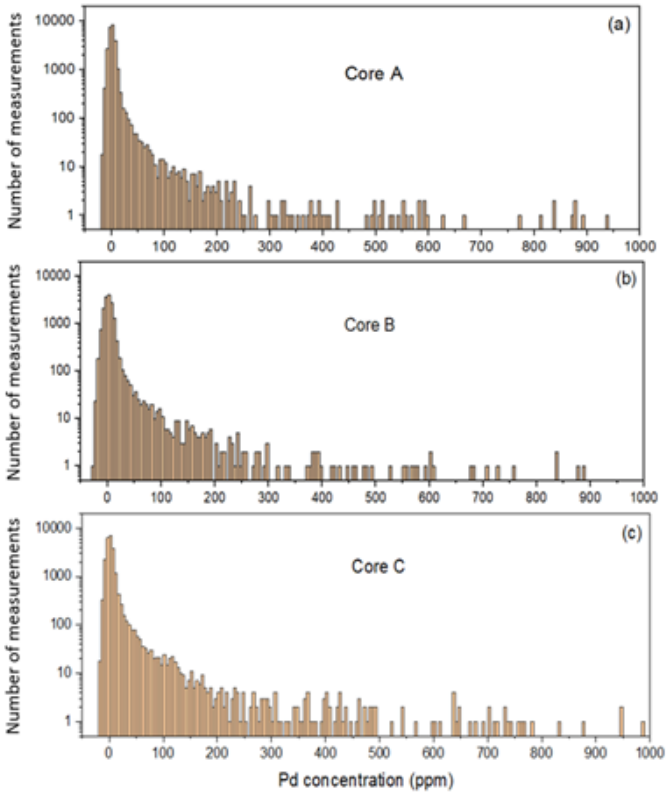

Figure A-9 **Palladium concentration distributions using analytical probability density. The model Eq. (2) with $\alpha = 1/10$ and $\lambda = \mu/3.352212864 \times 10^{11}$, including Gaussian noise. (a) $N = 25\,165$ virtual measurements using $\mu = 5$ ppm and $s_n = 5$ ppm. (b) $N = 16\,035$, $\mu = 7$ ppm and $s_n = 7$ ppm. (c) $N = 22\,698$, $\mu = 10$ ppm and $s_n = 5$ ppm. The bin size of the histograms is 5 ppm.**

We note some discrepancies between Fig. A.9 and Fig. A.4 around the zero concentration which is particularly noticeable for core C. This is the case for all realizations of N virtual measurements tried. We could not find parameters within our three-parameter analytical model (α, λ, and s_n) that provided a better fit to the experimental measurements. The model could possibly be improved by using a more general distribution for the noise, such as the generalized Student's distribution, which includes an additional parameter. A slightly higher value of s_n was used in Fig.A.9b ($s_n = 7$ ppm) than in Figs.A.9a and 9c ($s_n = 5$ ppm) to improve the fit to Fig. A.4b. Although relatively small variations in s_n have a noticeable effect on the concentration distribution near zero concentration, the effect of s_n on the parameters of interest here, namely C_5, C_{95} and P_{30}, is negligible as long as $(s_n/\sigma)^2 \ll 1$ since these parameters depend on $\sigma' = (\sigma^2 + s_n^2)^{1/2}$.

To have a closer look at the possible realizations of $N = 25\,165$ virtual measurements, we took the statistics of 106 sets of $25\,165$ measurements. The mean of the values of μ_N obtained for each set of N measurements is $\langle \mu_N \rangle = 5.00$ ppm with a standard deviation of 0.44 ppm, the latter value being close to $\sigma' N^{-1/2} = 0.46$ ppm expected from the CLT. On the other hand, the mean of

the values of σ_N obtained for each set of N measurements is $\langle\sigma_N\rangle = 62$ ppm with a standard deviation of 31 ppm, and the most likely value is about 46 ppm (close to the experimental value of 49 ppm). The distributions of μ_N and σ_N are shown in Fig. A.10. As expected from the CLT, the obtained distribution for the μ_N is close to a normal distribution in contrast to the probability density $\hat{f}(x)$. As suggested by additional calculations, the mean of the standard deviations $\langle\sigma_N\rangle$ would need a much higher value of N to approach the expected value of $\sigma' = 74$ ppm. Figure 8 10 shows that different values of μ_N and σ_N can be obtained from particular sets of $N = 25\,165$ measurements. Therefore, $N = 25\,165$ measurements may not always be representative of the intrinsic probability density $\hat{f}(x)$ of the sample. This may, of course, be the case for the experimental data shown in Fig.A.4.

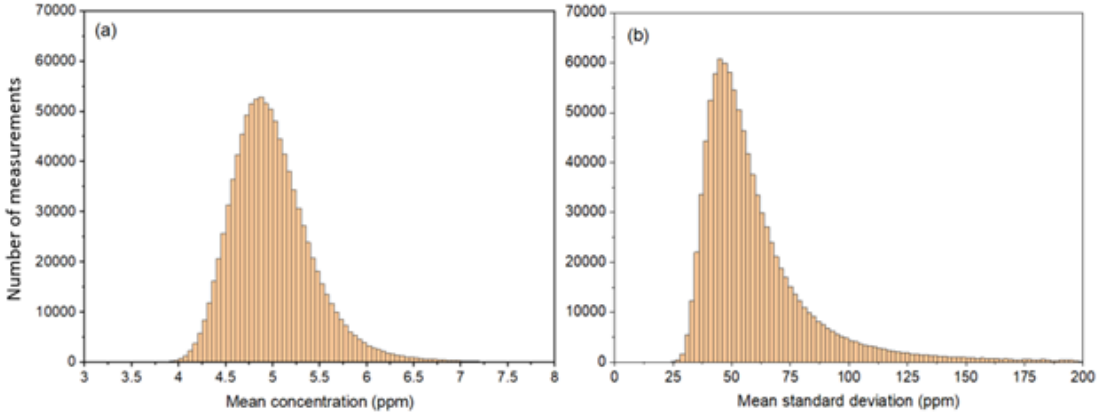

Figure A-10 **Distributions of mean concentration and mean standard deviation. Distributions of mean concentrations μ_N (a) and mean standard deviations σ_N (b) for 10^6 sets of 25 165 virtual measurements. The model uses Eq. (2) with $\alpha = 1/10$ and $\lambda = \mu/3.352212864 \times 10^{11}$ and includes Gaussian noise given by Eq. (10) with $s_n = 5$ ppm. The bin size of the histogram is 0.05 ppm in (a) and 2 ppm in (b).**

A.4.1 Probability calculations using the mathematical model

Figure A.11 shows C_5 and C_{95} for different number of virtual measurements N between 125 and 7 000 for 106 sets of N measurements. In the following calculations, the bin size of the distributions was set to 0.01 ppm. The result is similar to that of Fig. A.6 for the set of $M = 25\,165$ experimental measurements except that $C_{95} - C_5$ is somewhat larger here for the largest values of N due to the larger value of $\sigma' = 74$ ppm as compared to $\sigma_M = 49$ ppm.

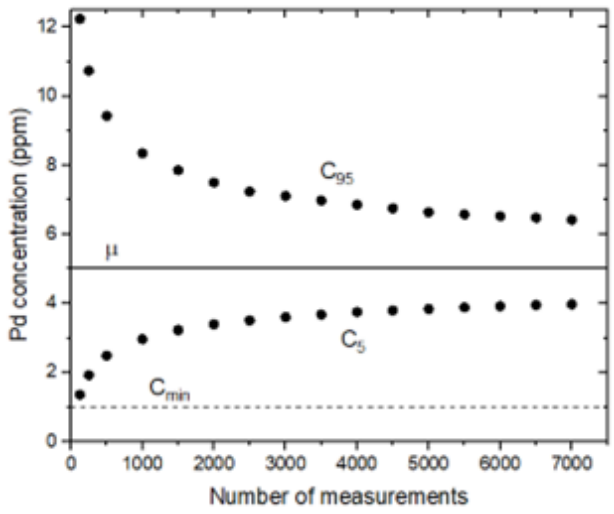

Figure A-11 **Palladium concentrations vs. number of virtual measurements. Palladium concentrations C_5 and C_{95} at 5% and 95% cumulative probability, respectively, as a function of the number of randomly selected measurements N, for 10^6 sets of N measurements. The model uses Eq. (2) with $\alpha = 1/10$ and $\lambda = \mu/3.352212864 \times 10^{11}$ and includes Gaussian noise given by Eq. (10) with $s_n = 5$ ppm. The mean concentration $\langle \mu_N \rangle$ is practically $\mu = 5$ ppm for all values of N.**

Our analytical model can be used to explore different scenarios. Still assuming $\alpha = 1/10$ (since there is no reason to make another assumption yet) and adjusting λ to obtain the desired mean concentration μ by means of Eq. (A.6), Figs. A.12a and 12b show C_5 and C_{95} for the cases $\mu = 1.5$ ppm and $\mu = 0.75$ ppm, respectively. In Fig.A. 12a, we can see that $N = 2\,500$ measurements are needed to confirm with 95% confidence that the analyzed sample is suitable for processing ($C_5 > C_{min}$). In Fig.A 12b, $\mu < C_{min}$. In this case, more than $N = 5\,500$ virtual measurements are required to confirm with 95% confidence that the ore is not suitable for processing at all ($C_{95} < C_{min}$). In the case where $\mu \approx C_{min}$, no decision can be made based on these probabilistic considerations regardless of the number of measurements. However, any analytical method will run into difficulties in assessing the economic viability of the ore when the mean concentration is close to C_{min}. In the three cores examined with $\mu = 0.75, 1.50$, and 5.00 ppm, it appears that a few thousand randomly distributed measurements are sufficient to make a decision.

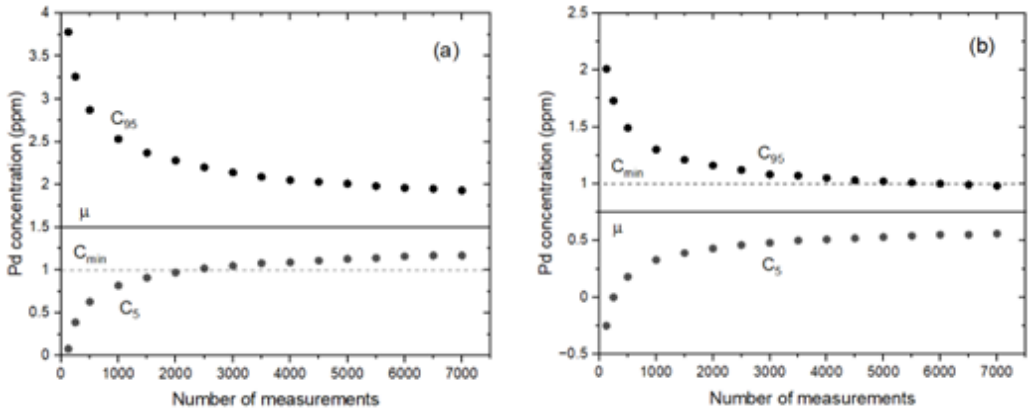

Figure A-12 **Palladium concentrations vs. number of virtual measurements for different parameters λ. Same as Fig 11 but for the parameter λ adjusted so that $\mu = 1.5$ ppm (a) and $\mu = 0.75$ ppm (b).**

Figure.8.13 shows the probability P_{30} as a function of the number of measurements N for 106 sets of N measurements for $\mu = 0.75, 1.50$, and 5.00 ppm. The results are similar to those in Fig.8. 7 except that the convergence rate of P_{30} to 100% is slower due to the higher value of $\sigma'/\mu = 14.8$.

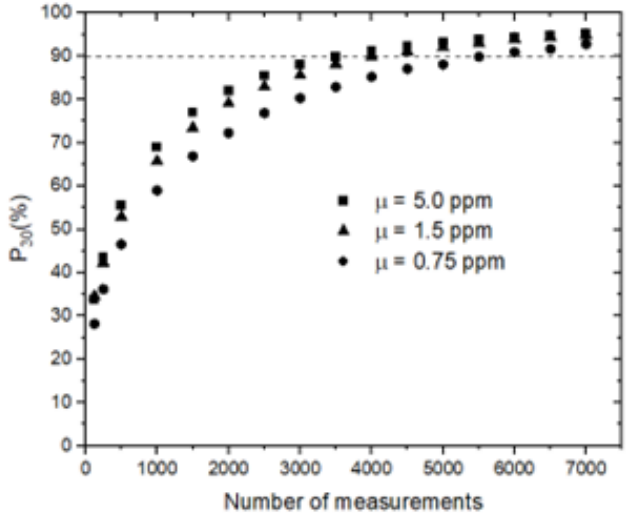

Figure A-13 **Probability of obtaining a palladium concentration within ± 30% of the mean concentration μ vs. number of virtual measurements. Probability of obtaining a palladium concentration within ± 30% of the mean concentration μ as a function of the number of randomly selected measurements N, for 10^6 sets of N measurements. Same as Fig 8.11 but for the parameter λ adjusted so that $\mu = 5.0, 1.5$ and 0.75 ppm.**

A.5 Conclusion

In this paper, a probabilistic study was performed to estimate the number of LIBS measurements N required to determine the mean palladium concentration within certain limits. Two types of limits

were considered for each value of N. Firstly, the lower (C_5) and upper (C_{95}) concentrations corresponding to a 90% probability of obtaining an mean concentration between these two values, with a 5% probability at either end of obtaining a mean concentration outside this interval. In this case, if a given economic viability threshold (C_{min}) lies outside the interval $[C_5, C_{95}]$ then the sample can be considered suitable ($C_5 > C_{min}$) or unsuitable ($C_{95} < C_{min}$) for palladium extraction processing with 95% confidence. Second, an interval of ± 30% around the mean concentration μ for the case where an absolute concentration measurement is required. To perform this probabilistic study, we first used a set of M experimental measurements, assumed to be representative of the intrinsic palladium concentration probability density of the core, and then constructed an analytical probability density that mimics the M measurements of the concentration distributions. The analytical function was used to explore the parameter space and to gain insight into the LIBS measurement process, in particular to understand the effect of noise on the measurements. The two approaches were found to give similar results despite the relatively small number of actual measurements made on the samples and the fact that only a relatively small fraction of the surface (less than 25%) was scanned.

The above analysis is a case study limited in scope to one trace element (palladium) in one type of ore (gabbronorite) from one specific area (B3) of the Lac des Iles palladium mine. The conclusion we draw from the analysis presented here is that a few thousand LIBS measurements, randomly distributed over the sample, are generally sufficient to assert that the average palladium concentration is within the confidence limits of practical interest. At a typical laser repetition rate of 50 Hz, 6 000 laser shots take 2 minutes, which is much faster than wet chemical analysis. As with any analytical method, more time would be required if greater precision were required. However, it should be remembered that LIBS performance depends on how representative the surface concentration is of the bulk core concentration.

Taking random laser shots at the core should not be a problem. In fact, the cylindrical core can be translated along its axis and rotated around its axis. By combining these two movements, the laser shots will form dotted spirals on the core. This allows the laser shots to be distributed relatively evenly across the surface of the core. In principle, with a fast processor, it would be possible to control the number of laser shots by monitoring the mean concentration trend during the analysis.

In order to go beyond the case study presented in this paper and provide useful guidelines for the use of LIBS in the mining industry, a systematic investigation of many representative samples is necessary to evaluate the appropriate LIBS methodology (laser parameters, type of reference

materials, etc.) to be used for a given class of samples. An analytical probability density can be used to better understand the importance of certain parameters such as noise level, mean concentration and standard deviation as a function of instrumentation and ore composition. However, a large-scale application of the results of this study was beyond the scope of this paper and is left for future work.

Appendix A

Tableau A-2 Lac des Iles designation of the drill cores discussed in this work

Core	Type	Zone	Sample number	Hole number	Depth range (m)
A	Gabbronorite	B3	X097924	18-805	189-190
B	Gabbronorite	B3	A0126692	19-520	142-143
C	Gabbronorite	B3	A0126695	19-520	145-146

Acknowledgements

We are grateful to Lionnel Djon formerly from Impala Canada for providing us with quarter drill cores from the Lac des Iles mine and their laboratory analysis.

Financial disclosure

This work was primarily supported by the National Science and Engineering Research Council of Canada (NSERC) [grant number STPGP 521608-18]. Financial support was also provided by Impala Canada. The funders had no role in study design, data collection and analysis, decision to publish, or preparation of the manuscript.

Author contributions

Conceptualization: François Vidal

Data curation: Samira Selmani, Ismail Elhamdaoui, Nessrine Mohamed, François Vidal

Formal analysis: François Vidal

Funding acquisition: Marc Constantin, François Vidal

Investigation: Samira Selmani, Ismail Elhamdaoui, François Vidal

Methodology: François Vidal

Project administration: Mohamad Sabsabi, Marc Constantin, François Vidal

Resources: Paul Bouchard, Mohamad Sabsabi, Marc Constantin, François Vidal

Software: François Vidal

Supervision: Mohamad Sabsabi, Marc Constantin, François Vidal

Validation: François Vidal

Visualization: François Vidal

Writing – original draft: François Vidal

Writing – review & editing: Samira Selmani, Ismail Elhamdaoui, Mohamad Sabsabi, Marc Constantin, François Vidal

A.REFERENCES

[1] R.B. Anderson, R.V. Morris, S.M. Clegg, J.F. Bell III, R.C. Wiens, SD. Humphries, SA. Mertzman, TG. Graff, R. McInroy The influence of multivariate analysis methods and target grain size on the accuracy of remote quantitative chemical analysis of rocks using laser induced breakdown spectroscopy. Icarus, vol. 215, pp. pp. 608-627, 2011

[2] D. Decharte, C. Perusse, T. Hofton, C. Roney, G. Marrs, S. Taylor, S. Olson, D. Thibodeau, D. Peck, B. Young, Feasibility study for Lac des Iles Mine incorporating underground mining of the Roby Zone. Technical Report, North American Palladium Ltd, 2018.

[3] Y. Deguchi, Z. Wang, Industrial Applications of Laser-Induced Breakdown Spectroscopy, Plasma Science and Technology - Progress in Physical States and Chemical Reactions. Chapter 14 Industrial applications of laser-induced breakdown spectroscopy. https://doi.org/10.5772/61915 (last accessed December 18, 2023, 2016.

[4] I. Elhamdaoui, N. Mohamed, S. Selmani, P. Bouchard, M. Sabsabi, M. Constantin, F. Vidal, Rapid quantitative analysis of palladium in ores using Laser-Induced Breakdown Spectroscopy assisted with laser-induced fluorescence (LIBS-LIF). J. Anal. At. Spectrom. Vol.37, pp2537, 2022.

[5] C. Fabre Advances in Laser-Induced Breakdown Spectroscopy analysis for geology: a critical review. Spectrochim. Acta Part B, vol.166, pp105799, 2020.

[6] F.F. Fontana, B. V. der Hoek, S. Tassios, C. Tiddy, J. Stromberg, N. Francis, Y.A .Uvarova, D.G. Lancaster Laser Induced Breakdown Spectroscopy (LIBS) for whole rock geochemistry. J. Geochem. Explor, vol 246, pp107160, 2023.

[7] R.S Harmon, R.E. Russo, R.R. Hark, Applications of laser-induced breakdown spectroscopy for geochemical and environmental analysis: a comprehensive review. Spectrochim. Acta Part B. vol. 87, pp. 11, 2013.

[8] R.S. Harmon, C.J.M Lawley, J. Watts, C.L. Harraden, A.M. Somers, Hark RR, Laser-induced breakdown spectroscopy—an emerging analytical tool for mineral exploration. Minerals, vol. 9, pp. 718, 2019.

[9] R.S Harmon, G.S Senesi, Laser-induced breakdown spectroscopy–a geochemical tool for the 21st century. Appl. Geochem, vol. 128, pp. 104929, 2021.

[10] E. Herincs, M. Puschenreiter, W. Wenzel, A. Limbeck, A novel flow-injection method for simultaneous measurement of platinum (Pt), palladium (Pd) and rhodium (Rh) in aqueous soil extracts of contaminated soil by ICP-OES. J. Anal. At. Spectrom. Vol. 28, pp. 354, 2013.

[11] M.C. McCanta, P.A .Dobosh, M.D. Dyar, H.E. Newsom, Testing the veracity of LIBS analyses on Mars using the LIBSSIM program. P&SS, vol. 81, pp. 48, 2013.

[12] N. Mohamed, K. Rifai, S. Selmani, M. Constantin, F. Doucet, L. Ozcan, M. Sabsabi, F. Vidal, Chemical and mineralogical mapping of platinum-group element ore samples using laser-induced

breakdown spectroscopy and micro-X-ray fluorescence. Geostand. Geoanal. Res. Vol. 45, pp. 539, 2021.

[13] J.J. Molloy, J.A Holcombe, Detection of palladium by cold atom solution atomic absorption, Anal. Chem, vol. 78, pp. 6634, 2006.

[14] F. Robert, A. Galley, Exploration Innovation Consortium: Keeping Canada's Mineral Exploration Globally Competitive, Presentation to CMIC Signature Event, Toronto, 2013.

[15] S. Selmani, N. Mohamed, I. Elhamdaoui, J. Fernandes, P. Bouchard, M. Constantin, M. Sabsabi, F. Vidal, Laser-induced breakdown spectroscopy analysis of palladium in rock ore. Spectrochim. Acta Part B. vol. 196, pp. 106523, 2022.

[16] S. Selmani, I. Elhamdaoui, N. Mohamed, P. Bouchard, M. Constantin, M. Sabsabi, F. Vidal, Laser-produced craters in minerals of a palladium ore sample, Appl. Phys. A, vol. 129, pp. 737, 2023.

[17] V.K Singh, D.K Tripathi, Y. Deguchi, Z .Wang (Editors), Laser Induced Breakdown Spectroscopy (LIBS): Concepts, Instrumentation, Data Analysis and Applications. 2 Volume set, Wiley 2023.

[18] Xiao Z, Laplante AR, Characterizing and recovering the platinum group minerals—a review. Miner. Eng. Vol. 17, pp. 96,2004.